Computationally-Efficient Thermal Modeling Techniques for Electric Machines

by

Yuanying Wang

A dissertation submitted in partial fulfillment
of the requirements for the degree of
Doctor of Philosophy
(Electrical and Computer Engineering)
in The University of Michigan
2021

Doctoral Committee:

Professor Heath Hofmann, Co-Chair
Professor Jing Sun, Co-Chair
Assistant Professor Al-Thaddeus Avestruz
Associate Professor Krzysztof Fidkowski
Professor Ian Hiskens
Associate Research Scientist Jason Siegel

Yuanying Wang

yuanying@umich.edu

ORCID iD: 0000-0001-7421-7032

ACKNOWLEDGEMENTS

Graduate study has been much more difficult than what I pictured. However, looking back on these years in Michigan, this journey remains a priceless experience, thanks to all the support I received.

First of all, I would like to express my gratitude to my advisors, Professor Heath Hofmann and Professor Jing Sun. I still remember the first time I knocked on Prof.Hofmann's office, and he showed me around Michigan Power and Energy Lab, where I started my research journey. He has provided me with countless valuable guidance and experience in academics and life and is always patient, supportive, responsible, and rigorous. I also appreciate his tolerance and comfort with my mistakes and broken lab devices. I later joined Prof.Sun's research group, and her high standards towards research but warmth and kindness outside her office set me a good model. Their encouragement and sufficient supports are a great motivation and relief, especially under this pandemic. I also want to show my appreciation to my committee members, Professors Krzysztof Fidkowski, Ian Hiskens, Al-Thaddeus Avestruz, and Dr.Jason Siegel, for their valuable help, suggestions, and feedback.

I want to acknowledge the Automotive Research Center and U.S Office of Naval Research for their support and our collaborators Dr.Denise Rizzo, Mr.Scott Shurin, Dr.Andrej Ivanco, Dr.Xiao Hu, Dr.Lei Hao for their help and support.

I would also want to extend my thanks to my labmates and friends. It is my honor to work with Fanny Pinto Delgado, Jake Chung, Dr.Ziyou Song, Dr.Jun Hou, Dr.Abdi Zeynu, for all the time we spent together with those high voltage devices,

for their academic help and support, for the research insights coming up during our discussions, and for cheering each other up with desserts and bubble tea. I also want to thank Dr.Kan Zhou and Dr.Jason Pries for sharing their research results and providing supports for continuous research work. As to my friends in Michigan, I want to show my gratitude to Shuqi Cheng, Bin Shao, Yu Huang, Miriam Figueroa-Santos, Shichang Xu, Fengmin Hu, Yuanzhen Wang, Dan Zhao, Zumrad Kabilova, Mengqi Yao, Sijia Geng, Akshay Sarin, Xin Zan, Xiaofan Cui, and Xinran Tao and my lifelong friends Weijia Wang, Xinyi Shen and Yin Xie. I also want to show special thanks to my boyfriend Zhenguo Chen, for his understanding, company, humor, and significantly improved cooking skills.

Finally, I want to show my gratitude to my parents and grandparents for their unconditional love and care. It is not easy for a family to keep a 12 hour time difference for such a long time. They also teach me what to insist on and what to give up. I hope I can stick to their lifelong motto "Live and Learn" and keep moving forward.

TABLE OF CONTENTS

LIST OF FIGURES

Figure

LIST OF TABLES

Table

LIST OF ABBREVIATIONS

AC Alternative Current

ARD Average Relative Difference

CFD Computational Fluid Dynamics

CAFE Corporate Average Fuel Economy

DC Direct Current

DNS Direct Numerical Simulation

EMF Electromotive Force

EOE Extent of Excitation

EV Electric Vehicles

FEA Finite Element Analysis

GSE Generalized Steinmetz Equation

HEV Hybrid Electric Vehicles

ICE Internal Combustion Engines

iGSE Improved Generalized Steinmetz Equation

IPMs Interior Permanent Magnet Machines

RLS Recursive Least Squares

LDV Light Duty Vehicles

LPTM Lumped Parameter Thermal Model

MOR Model Order Reduction

MPC Model Predictive Control

MQS Magnetoquasistatic

MRE Maximum Relative Error

MSE Modified Steinmetz Equation

MVP Magnetic Vector Potential

NSE Natural Steinmetz Equation

ODE Ordinary Differential Equation

PCA Principal Component Analysis

PD Positive Definite

PDE Partial Differential Equation

PM Permanent Magnet

PMSMs Permanent Magnet Synchronous Machines

POD Proper Orthogonal Decomposition

PSD Positive Simi-Definite

PWM Pulse Width Modulation

RANS Reynolds-Averaged Navier-Stokes Equations

RSM Reynolds Stress Equation Model

RTDs Resistance Temperature Detectors

SA Spalart–Allmaras Model

SE Steinmetz Equation

SMPMs Surface-Mount Permanent Magnet Machines

SST Menter's Shear Stress Transport Model

SVM Singular Value Decomposition

TEFC Totally Enclosed Fan-Cooled

ABSTRACT

Electric machines are widely used in industry, ranging from as large as 700Mw generators used in Three Gorges in Yichang, China, to as small as brushless Direct Current (DC) motors used in your computer hard drives. For some areas, such as automotive powertrain design, accurate and computationally-efficient models for electric machines are in great demand since they can play important roles as either real-time observers or in vehicle simulations. In this dissertation, computationally-efficient thermal and electromagnetic models for electric machines are developed. In particular, a thermal convection model to capture air region heat convection considering air density variation and slotting effects on stator surface is developed and analyzed; and an electromagnetic model to calculate Alternative Current (AC) winding resistance of different winding configurations is proposed and integrated. With the developed techniques, thermal and electromagnetic performance can be accurately and efficiently estimated. Furthermore, this dissertation has conducted a comparative study, which shows the advantages of using thermal models for online loss estimation for electrical machines over the conventionally-used electric model. The conclusions and results of this study provide useful tools for online loss estimators with model uncertainty.

CHAPTER I

Introduction

1.1 Background and Motivation

During the last few decades, transportation electrification has been a major trend. Most of the world's petroleum is consumed by transportation [1], which leads to severe air pollution and contributes to global warming through carbon dioxide emission. On the other hand, the rise in global fossil fuel consumption and the difficulty of finding new reserves has deepened the concerns of fossil energy depletion. Many countries have announced the goal to end the production of vehicles based on Internal Combustion Engines (ICE), aiming to transition to a cleaner and electrified transportation sector [2]. For example, in the U.S, several states have set goals to reduce national vehicle emissions to zero by 2050 [3]. Japan has set the target of selling Electric Vehicles (EV) only by 2050 [3]. India is one of the few countries with a concrete strategy for transport electrification and has committed to ending the sale of fossil-fuel-powered vehicles by 2030 [3]. China is working on a plan to end the production and sale of vehicles powered solely by fossil fuels and achieve a zero-emissions fleet by 2050 [3]. The trend of Light Duty Vehicles (LDV) market share by energy type is shown in Fig. 1.1. It can be seen that conventional transportation with internal combustion engines is gradually reducing its market share of LDV. At the same time, advanced powertrain vehicles have occupied more market share.

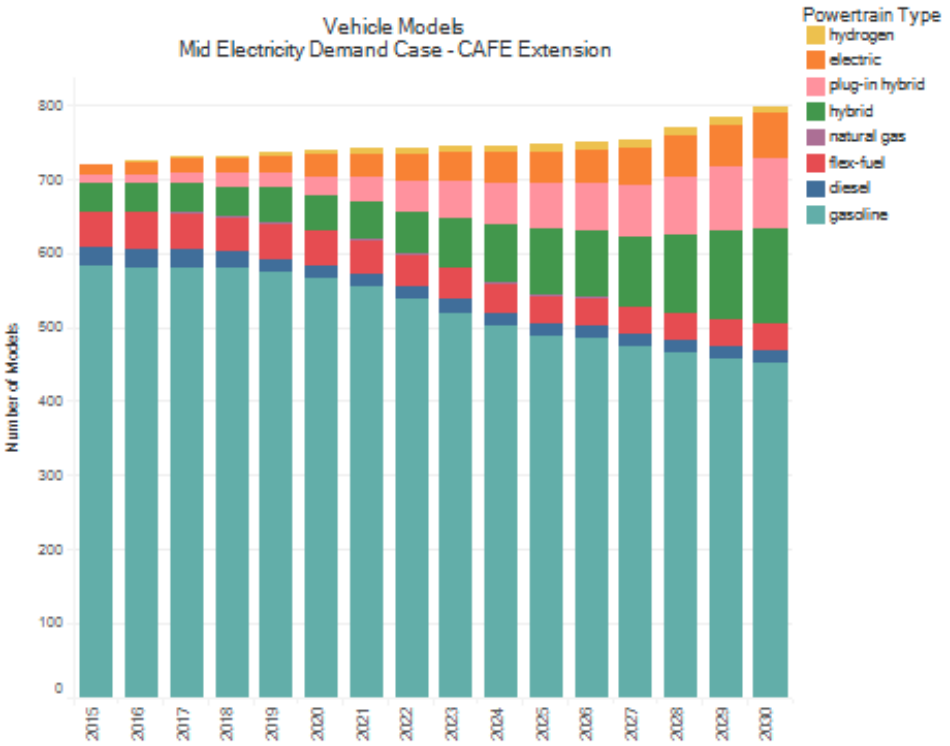

Figure 1.1: Numbers of LDV Models in the Mid Electricity Demand Case With CAFE [4]

Electric machines are a key component in the powertrain of electrified transportation. Its design and operation involve physical phenomena such as electromagnetic, thermal (conduction, convection, radiation), structural, etc, thus is fundamentally cross-disciplinary. The models for electric machines that can capture many details usually have significant computation cost, thus can not meet the computation requirement of applications such as real-time monitoring and machine design optimization. This dissertation focuses on thermal and electromagnetic modeling of electric machines, specifically, heat convection modeling and AC resistance modeling. The goal is to develop both accurate and computationally-efficient models to enable high performance control design and condition monitoring. One real-time application is presented: online loss estimation of electric machines, with a comparative study showing the advantages of using the thermal model over the conventionally-used electrical model.

1.2 Literature Review and Objectives

In this section, the literature on thermal and electromagnetic modeling of electric machines is reviewed. The literature on the applications of the thermal models is also included. Based on the context and background established through the literature review, the dissertation's objectives are presented at the end of each subsection.

1.2.1 Thermal Modeling

Electric machines' power and torque capabilities are often limited by temperature distribution [5], thus, knowledge of internal machine temperature is essential for control, online monitoring [6], protection [7], machine design optimization [8], and full-scale vehicle-level powertrain simulation, and thermal management [9]. Accurate and fast thermal models for electric machines are needed.

The influence of temperature on torque capabilities is shown in Fig. 1.2.

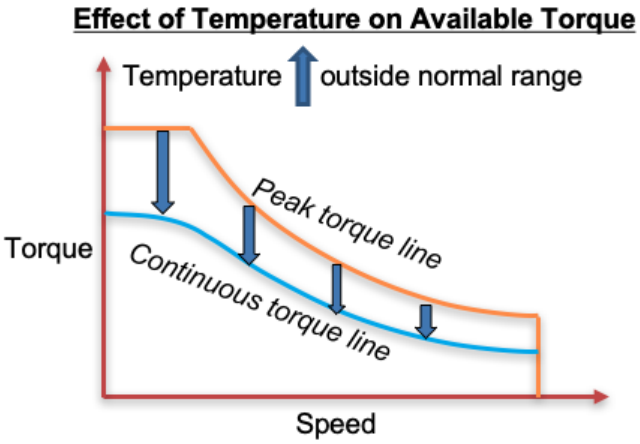

Figure 1.2: Temperature Influence on Torque Curve [10]

Many machine parameters are temperature dependent, such as the winding resistance. The normal operation of electric machines without failure also requires that component temperature remain within their operating temperature range.

Taking Permanent Magnet Synchronous Machines (PMSMs) as an example, the

main temperature of interest includes the Permanent Magnet (PM) and the stator winding temperatures. High temperatures can cause demagnetization for the PM, which poses a severe problem because demagnetization can lead to degradation of the torque production and efficiency. It is time-consuming and costly to repair the problems due to demagnetization [11]. For the stator winding, high temperatures are one of the main reasons for insulation aging [12]. Referring to the Arrhenius model usually applied to thermal aging [13]:

$$L_t = Be^{E_a/k_bT}, \tag{1.1}$$

where L_t is the lifetime, B is the constant determined from experiments, E_a is the activation energy, k_b is the Boltzmann's constant, and T is the absolute temperature. The higher the temperature, the faster the thermal aging and shorter the lifetime.

The geometry of one pole in one kind of PMSMs, the Interior Permanent Magnet Machines (IPMs), with spots of interests (winding, PM, etc.) are shown in Fig. 1.3.

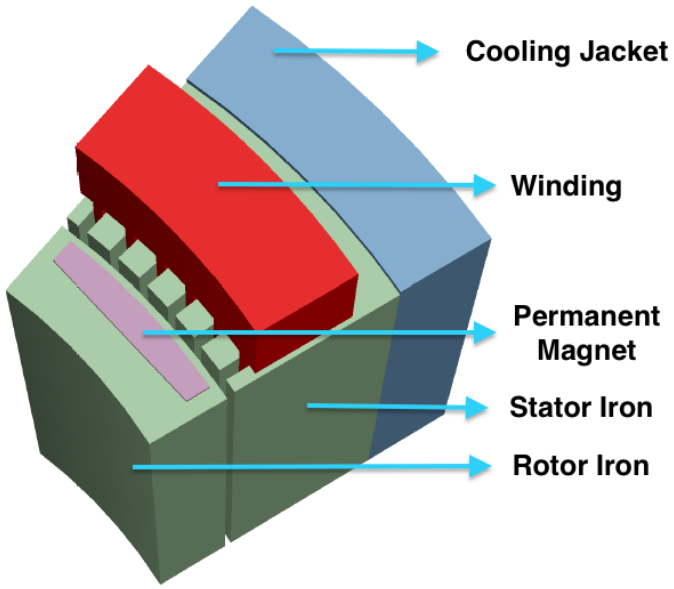

Figure 1.3: Temperature of Interest in IPMs [14]

In order to better analyze an electric machine's performance under different operating conditions, accurate knowledge of internal temperatures is required. Moreover, such knowledge needs to be obtained by a computationally-efficient method suitable for real-time applications, as direct measurement of these temperatures are infeasible due to cost and other constraints.

In previous work, [15], a 3D Finite Element Analysis (FEA) based thermal conduction model was constructed and then reduced into a model with an acceptable error. Through an eigenmode-based Model Order Reduction (MOR) technique, this thermal conduction model is many orders of magnitude faster than the original model, and was validated on a UQM PowerPhase 145 PM machine. Its rotor is fixed to limit the thermal convection to natural convection and it avoids complex thermal convection effects due to machine rotation. Experiment results show close agreement, with the maximum temperature error of end-turn and permanent magnet of $1.69°C$ and $1.13°C$, respectively, in the driving cycle test of maximum torque 280N-m, using 7 states for the stator and 4 states for the rotor. However, this thermal model is not complete because the heat convection behavior due to air movement caused by rotation is not captured.

This dissertation will focus on the thermal modeling of the convection in the air region inside electric machines. To better understand the air region, a cross-section of 1/8 geometry of an IPMs is shown in Fig 1.4. The internal air domain is divided into two parts: the air gap region (the red dotted line) and the end region (the shaded area). The air gap region is formed in the thin gap between two annular cylinders: the rotor and stator. The end region is formed in the relatively larger space between the end cap housing and the rotor/stator surface facing the end cap housing.

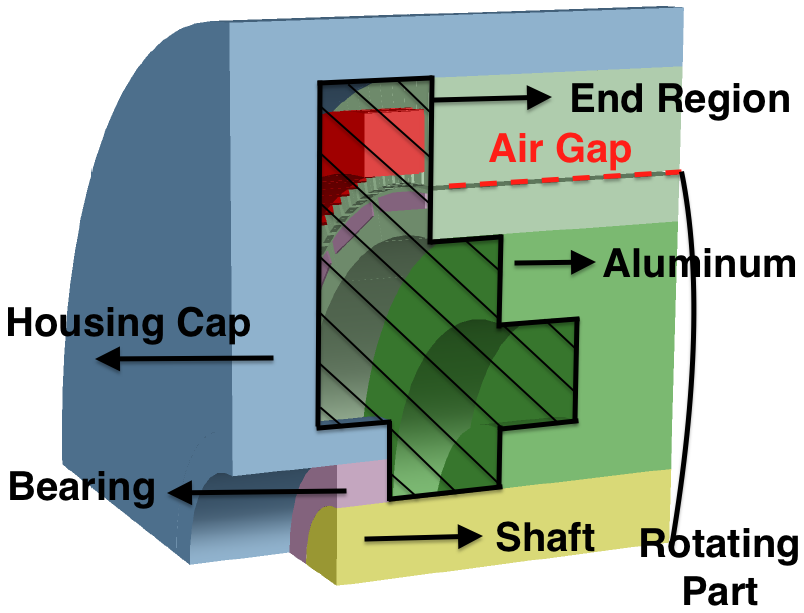

Figure 1.4: Air Domain inside IPM

This dissertation will investigate electric machines under the following assumptions: 1. without any cooling fans implemented to create axial flow through the machine; 2. without any multi-phase changes of materials to increase heat transfer, such as cooling oil spraying. These constraints allow me to focus on modeling the air circulating inside non-sealed electric machines due to the moving rotor, excluding other forms of mechanism that may enhance heat convection.

Researchers apply two major methods to model heat convection for electric machines: equivalent thermal resistor in Lumped Parameter Thermal Model (LPTM) and numerical calculations such as Computational Fluid Dynamics (CFD).

The LPTM approach reduces the system to many discrete "lumps," assuming that the temperature difference within each entity is negligible. This approximation is to simplify otherwise complicated differential heat equations and has the advantage of short computation time. However, the accurate thermal network formation may need careful investigation, especially for main thermal paths. The LPTM is sometimes referred to as a heat thermal network, which shares commonalities with electric

circuits: the temperature to the voltage, the power to the current, and the thermal resistance to electrical resistance. Thus, a thermal resistance network describes the main paths for power flow in conduction and convection, where the resistance values are determined from conduction and convection parameters. This network enables the calculations of main components' temperatures for a given loss distribution [16]. The lumped parameters for different thermal paths in electric machines can be calculated according to [17].

The thermal resistance for convection is equal to one over the product of effective area and heat convection coefficient:

$$R_{conv} = \frac{1}{h_{conv} A_{eff}}, \tag{1.2}$$

where R_{conv} is the thermal convection resistance, h_{conv} is the convective heat transfer coefficient, A_{eff} is the effective area. The heat convection coefficient, however, is not easy to calculate. It is mostly obtained by fitting experimental data to empirical formulation, which strongly depends on machine geometry and operating conditions, and the level of accuracy may be limited by sensor resolutions.

The traditional way to calculate the heat convection coefficient for the air region in electric machines is to use the dimensionless convection correlations, as shown in Eq.(1.3) by empirical models:

$$Nu = f(Re, Pr), \tag{1.3}$$

In Eq.(1.3), three dimensionless number are introduced: the Nusselt Number (Nu), the Reynolds Number (Re) and the Prandtl Number (Pr). Those dimensionless numbers, together with the Taylor Number (Ta, specifically for the air gap),

which will also appear later in this work, are defined as follows:

$$Nu = \frac{h_{conv}L}{k}, \tag{1.4a}$$

$$Re = \frac{\rho V L}{\mu}, \tag{1.4b}$$

$$Pr = \frac{C_p \mu}{K}, \tag{1.4c}$$

$$Ta = \frac{w_r^2 R_r (R_s - R_r)^3}{\nu^2}, \tag{1.4d}$$

where L is the characteristic length (the radius or diameter for the air gap, and distance from the end housing to the rotor/stator surface for the end region), k is the fluid thermal conductivity, ρ is the fluid density, V is the fluid velocity, μ is the fluid dynamic viscosity, C_p is the fluid specific heat, w_r is the fluid angular velocity, R_s and R_r are the inner and outer radius of stator and rotor, ν is the fluid kinetic viscosity.

The flow has been classified into laminar, turbulent, or vortex categories according to Reynolds number, which depends on fluid velocity for a particular fluid. Taylor Number is similar to Reynolds number but is used specifically for coaxial cylinders, similar to the air gap geometry. Prandtl number describes the ratio between momentum to thermal diffusivity. Once the correlation between the Nusselt number and the Reynolds number/Prandtl number is determined by Eq.(1.3), the heat convection coefficient can be determined from Eq.(1.4a), and the thermal resistance for convection can be calculated using Eq.(1.2).

For the air gap, the reference [18] did an analytical analysis for air gap flow and [19] measured velocity and temperature profile between annular cylinders. A special type of flow was discovered by [18]: Taylor vortices. This flow is named Taylor-Couette Flow or Taylor-Couette-Poiseuille Flow depending on whether enforced axial flow is present. Taylor vortices come into existence when fluid speed exceeds a threshold after laminar flow before becoming turbulence and it possess an interesting periodic

structure in the axial direction. Due to the strong air mixture, Taylor vortices in the air gap enhances heat transfer [20]. However, all these mentioned literature assumed smooth cylinder surface and did not include slots on stator surfaces, which increase the effective volume of the air gap. The slots are the deep grooves on the stator surface for coil winding placement, as shown in Fig. 1.5. Some space remains after the winding has been placed, leaving an extra air domain connecting to the air gap region, the blue area in Fig. 1.5. The remaining slots will enhance heat transfer between the stator and rotor due to a larger surface area and a greater air mix with different velocities. Fenot *et al.* [21] did experimental tests to measure local heat transfer of annular cylinders: inner rotating slotted cylinders and outer stationary cylinders, but the geometry can not be applied for the slotted stator.

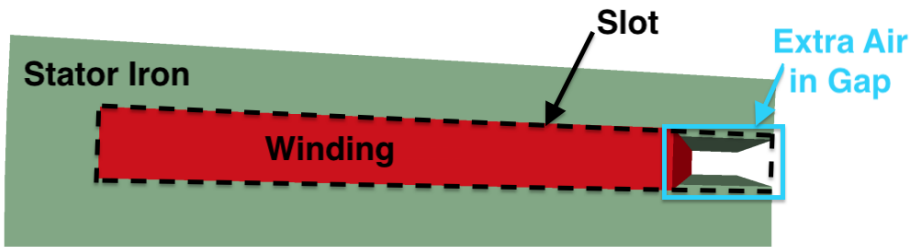

Figure 1.5: Slots on Stator Surface

For the end region, empirical models are mostly applied to model heat convection. For example, a hybrid thermal model consisting of an LPTM and limited CFD simulations is provided in [22]. Ahmad *et al.* [23] and Veg *et al.* [24] used different thermal resistances for the stator and rotor end region. Boglietti *et al.* [25] investigated the heat convection coefficient at the end region for different machines based the measurements on a nylon rotor. Zhang *et al.* [26] separated the convection resistance near the rotor and near the stator in the end region since the Reynolds numbers close to housing and rotor are different.

With the development of modern computers with more computation power, the numerical approaches, such as CFD, have been more widely used to analyze heat

convection for electric machines. It has the advantage of applicable to any machine geometry. On the other hand, correctly setting up the simulation parameters and the appropriate fluid model is not easy. Each model has its own advantages and also restrictions in different scenarios. Meanwhile, the accuracy of CFD simulations can't be guaranteed in many cases. Many papers published dealt with comparing predicted heat convection coefficients with those measured experimentally or established by correlations [27].

For the air gap, flow behavior can be more conveniently analyzed with the help of CFD, especially for Taylor vortices for its complex flow structure in different directions. Viazzo *et al.* [28] conducted numerical simulations for the Taylor-Couette system with a radial temperature gradient. Several flow regimes have been discovered, and a correlation between Nusselt number and Taylor number along rotor and stator has been demonstrated. Hosain *et al.* [29] used CFD to model annulus air gap heat transfer for both steady and transient analysis. But [28] and [29] did not consider slot effects and used incompressible air model. The simulations by [28] did not match well with experiments provided in [30]. Hayase *et al.* [31] used CFD to numerically calculate the heat convection between rotating cylinders with periodic cavities and discovered that the slots influence the turbulent flow dramatically. Lancial *et al.* [32] analyzed slot effects by CFD simulations, but the flow simulated was Taylor-Couette-Poiseuille flow, and the slots were on rotor surfaces. Kedia *et al.* [33] conducted numerical simulations to study heat transfer of Taylor-Couette flows influenced by natural convection.

For the end region, Micallef *et al.* [34] conducted CFD simulations and validated the CFD results with experimental data. Lampard *et al.* [35] used CFD to model the ventilation of end winding with the complex winding structures for Totally Enclosed Fan-Cooled (TEFC) electric machines.

However, the numerical calculations and experimental correlations for the above

literature do not consider the air density variation due to temperature change. The temperature for electric machines can range from room temperature up to $150°C$, so air density can vary over a relatively large range, as shown in Fig. 1.6:

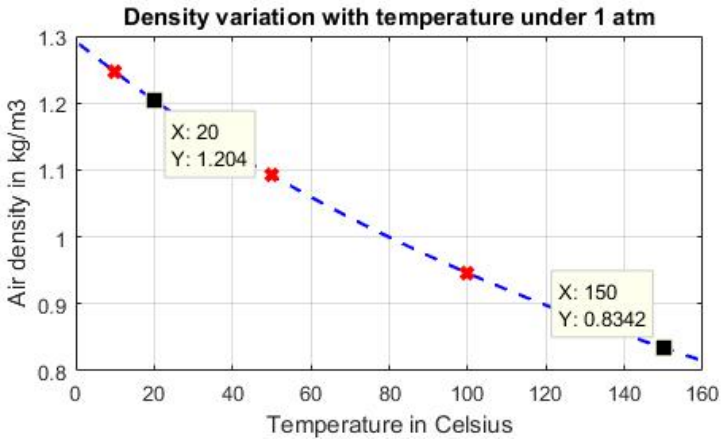

Figure 1.6: Air Density Variation with Temperature under 1 Atm [36]

Several efforts have been made to reduce CFD computation time. References [37] and [38] used the linear model, assuming incompressible flow, and decoupled velocity and temperature field. Then linear MOR technique can be applied using Singular Value Decomposition (SVM), etc. Other non-linear order reduction techniques are applied for general CFD simulations, such as steady-state modeling by Principal Component Analysis (PCA) [39] and transient modeling by Proper Orthogonal Decomposition (POD) [40].

To consider the effect of air density variation and the slotting effects, a heat convection model of an electric machine's air region is presented in Chapter 2. This convection model is constructed according to the homogeneity property of the mapping between different components' temperatures, the rotor speed, and the heat fluxes of different parts. This property is discovered through the simulations of heat convection of Surface-Mount Permanent Magnet Machines (SMPMs) under certain assumptions by a commercial CFD simulation software (Ansys Fluent) and then proved by the fundamental governing equations for fluid dynamics and heat transfer. The

parameters of this mapping are then determined using a global optimization and the least squares method. This homogeneity property dramatically reduces the number of simulations needed to build the convection model. Consequently, the model can be computed in real-time. Finally, this model is validated by the close agreement with CFD simulation.

1.2.2 Winding Loss Modeling

The losses act as the thermal model excitation. Once they are determined in an electric machine, temperatures inside the machine can be estimated. Thus, accurate determination of the power losses is one important procedure of thermal modeling of electric machines.

Losses in AC machines include conduction loss in the machine winding, core loss in magnetic materials, and mechanical loss (bearing and windage loss). These losses can be calculated using analytical or numerical models based on first principles or empirical formulas. However, the models are generally complex or computationally intensive. For example, the winding resistance model is complicated by its temperature dependency, skin, and proximity effects. The core loss is hard to be estimated, due to the high frequency, Pulse Width Modulation (PWM) harmonics and the influence of machine geometry on flux density distribution [41]. It is often described by empirical models, such as the Steinmetz Equation (SE), Modified Steinmetz Equation (MSE), Generalized Steinmetz Equation (GSE), Improved Generalized Steinmetz Equation (iGSE) and Natural Steinmetz Equation (NSE), shown and compared in [42] and applied in [43]. If the core material hysteresis curve is available, the mathematical models can be used for hysteresis loss calculation, such as the play and stop models for hysteresis loops as provided in [44]. As for numerical models, while FEA based electromagnetic simulations can provide better accuracy, they remain computationally intensive. References [45] and [46] provide 2D and 3D FEA simulations

for loss calculation. The windage loss can be calculated by theoretical equations in [47] for smooth cylinders but with limited accuracy, or numerical simulations such as CFD for better accuracy.

Stator winding loss is the dominant component of power loss in electric machine [48]. Due to skin effect and proximity effect, the current is re-distributed inside the conductor, creating difficulties in AC resistance modeling.

To better satisfy higher power density and higher efficiency requirements for automotive applications, rectangular conductor windings have been used due to their advantages in filling factor, thermal performance, and automated production compared to stranded/round conductors shown in [49] and [50]. Two main approaches are used to model the AC resistance of conductors in magnetic devices: analytical and numerical approaches.

The analytical AC resistance model built by Dowell in [51] is widely used. This method determined the current density distribution for transformer windings using a 1D analysis by solving the ordinary differential equation with the appropriate boundary conditions. References [52] and [53] used similar methods for transformer and AC stator windings, respectively. They made use of Dowell's model and developed designs that minimize losses.

Built-in orthogonality between skin and proximity effect in a 1D analysis was discovered by Ferreira *et al.* [54], assuming uniform proximity field over the conductor cross-section. This method separated the calculation of skin and proximity effect and simplified the calculation of AC resistance. Bartoli *et al.* [55] made use of this orthogonality to calculate the overall AC resistance of a Litz wire. Holguin *et al.* [56] combined Dowell's 1D approach with Ferreira's orthogonality approach and proposed an improved method to calculate AC resistance for inductors. Wu *et al.* [57] analyzed open-circuit, armature reaction, and on-load resistance limited eddy current loss in the winding, using spatial harmonics and a Fourier Series decomposition to analyze

the influences on harmonics on loss distribution. Bellara *et al.* [58] derived a 2D analytical solution for flux density in slotted SMPMs with variable separation.

Concerning slot and conductor geometry, Swann *et al.* calculated the AC resistance of different slot geometries for electric machines: cylindrical [59], rectangular [60], and trapezoidal [61] without considering the influence of the number of turns. Xu *et al.* [62] discretized a pear-shaped slot of electric machines along the radial direction and solved the analytic equations based on boundary conditions approximately, assuming a tangential magnetic field. Ferreira *et al.* [63] gave the analytical solution of AC resistance of round cables by calculating the total power loss. Thomas *et al.* [64] compared a 1D analytical model for AC loss for a switched-flux machine with numerical results and optimized the conductor size. Hamalainen *et al.* [65] used the formula from [66] for AC resistance for Litz wire and applied it to low-voltage high-power generators.

FEA has been used to determine AC resistance. Mostly, 2D FEA simulations of machine windings have been conducted. Nan *et al.* [67] compared the analytical expressions provided by [51] and [54] to FEA simulation results and determined the conditions to achieve better accuracy for each analytical model while normalizing the parameters to reduce error. Hamalainen *et al.* [68] performed FEA simulations of the winding inside a slot and took circulating current and end turn into consideration to calculate AC resistance. Gonzalez *et al.* [69] used FEA to analyze form-wound windings and validated the results with experiments. Ayat *et al.* [70] compared the performance of interior permanent magnet machines with copper and aluminum conductors, claiming that the increased material resistance helps abate the effects of proximity effect. Paradkar *et al.* [71] analyzed various stranded-conductor configurations in two slots for one winding coil. Venegas *et al.* [72] applied FEA to analyze the magnetic and electric fields in a single-coil and performed FEA for faster computation by equivalent materials. FEA can simulate all possible configurations; however, it has

a high computation cost.

Most of the analytical models [51-54,64] assumed the same current flowing in all conductors in a stator slot. Reference [62] focused on stranded conductors assuming tangential flux density and can model complicated winding configurations such as double-layer windings. However, it does not provide a procedure to develop explicit expressions for AC resistance. As a result, more computation time is required (e.g., 0.34 sec), which may not be suitable for real-time applications. The method presented in [57] was based on modeling current density with spatial and temporal harmonics. This approach also lacks an explicit resistance expression derivation and hence is not expected to be computationally-efficient. References [59-61] assume only one conductor in the slot. Therefore, there is a need to find a method to quickly calculate the AC resistance of complex winding configurations to be used in real-time control applications.

An analytical technique to estimate the AC resistance of a stator winding with rectangular conductors, based on magnetoquasistatic analysis, is presented in Chapter 3. Like Dowell's method, the proposed method uses a 1D model of the stator slot region to develop boundary transfer relations for the winding turns. A set of equations associated with the winding turns relating current and the electric scalar potential/magnetic vector potential are set up, from which the impedance matrix is generated. From this impedance matrix, the AC resistance can be calculated. The proposed technique is more flexible than previous analytical solutions. It is not limited to analyzing full-pitch windings, where all the conductors in the slot are in series, but can also model arbitrary configurations such as fractional-pitch windings.

1.2.3 Loss Estimation

Losses can also be estimated through parameter identification, either offline or online. With offline identification, measurements, or estimations are obtained over

the operating range, and then look-up tables are generated. However, this requires expensive measurements and time due to the need for numerous experiments required over a wide operating range, especially for estimating multiple parameters. Furthermore, the results may be inaccurate as losses can vary over time, for example, temperature-dependent parameters can affect the estimation [73].

Online estimators are widely used to adapt to changes in parameters over time in different operating conditions. For linear systems, the convergence of estimated parameters can be guaranteed as long as the condition of excitation persistency is maintained, as shown in [74]. Other approaches have been proposed to assure parameter convergence.

Balamurali *et al.* [75] estimated core loss resistance offline and winding resistance online using Recursive Least Squares (RLS). Cao *et al.* [76] estimated inductance and winding resistance one step before by RLS for maximum torque per ampere control. Dang *et al.* [77] made use of two-time-scale online estimation; with a fast convergence rate for inductance and a slow convergence rate for winding resistance, flux linkage, and torque. Li *et al.* [78] used a thermal model offline to estimate resistance and an electrical model to estimate inductance using an ADALINE neural network. Khreis *et al.* [79] proposed a novel online estimation method for PMSM parameters based on the cluster technique, and used four clusters to solve the problem of under-determinant of the regressor matrix. Xu *et al.* [80] estimated inductance and winding resistance using RLS by adding another operating condition in the regressor matrix, assuming that the estimated parameters don't change with operating conditions. Liang *et al.* [81] proposed an online stator resistance estimation algorithm based on a first-order sliding mode observer.

Hey *et al.* [82] used a LPTM for online loss estimation, whose parameters were determined from experiments, but its accuracy level can lead to deviation of estimated loss parameters. Ghosh *et al.* [83] input the temperatures from a LPTM and cur-

rent/voltage information into an artificial neural network to estimate the loss. These methods assume a good knowledge of some parameters to reduce the total number of estimated parameters, which is essential when excitation is limited.

More often than not, only a subset of parameters is estimated for online parameter identification due to other constraints. Thus, robust estimators, which can maintain estimation performance despite uncertainties in the parameters which are not the targets of estimation, are critically important. The selection of the model can determine the performance and robustness of the estimator. For AC PM machine loss estimator, two models are possible: the electrical model [74-81] and the thermal model [82] and [83]. Most online loss estimators are constructed upon the electrical model and very few upon the thermal model. However, no report can be found that compares the corresponding estimators' performance.

To fill this knowledge gap, Chapter 4 conducts a robustness analysis for loss estimators for PMSMs based on both electrical and thermal models. An estimator's robustness is defined as the relative sensitivity of the estimated parameters with respect to uncertainties in parameters that are not the estimation targets, determined via steady-state sensitivity analysis. It is found that loss estimators based on thermal models are more robust than those based on electrical models over a wide range of operating conditions. The conditions, under which the thermal model can achieve better robustness, are obtained in analytical expressions and validated by simulation.

1.3 Contributions and Dissertation Outline

The technical contributions of this dissertation are:

1. Development of a new computationally-efficient heat convection model for electric machines: A homogeneity property is proved in the fundamental governing equations of fluid dynamics and energy conservation, and is used to create a ther-

mal convection behavior in the air region of electric machines. Numerous CFD simulations have been conducted concerning air density variation and stator iron/winding slotting effects. This property reduces the number of CFD simulations needed to determine model parameters and good agreement with CFD simulations. Taylor vortices flow has been investigated to build the thermal convection in the air gap. 2D CFD simulations for simplified smooth cylinder models and 3D simulations for slotted stator surfaces. The geometric conditions of obvious Taylor vortices have been investigated.

2. Development of a new computationally-efficient AC resistance model for AC machine winding: An AC resistance model for solid-conductor winding is developed, with the help of a proposed impedance matrix. This method is fast and applicable to different winding structures. Good agreement in predicted current density when compared to FEA simulations is shown. The proposed AC resistance model is validated by experiment.

3. Online loss estimation and analysis: Online loss estimation for electric machines based on electrical and thermal models are developed and compared. A comparative study to evaluate the estimator robustness is conducted. It is found that estimators based on thermal models are more robust than those based on electrical models over a wide range of operating conditions. The operating conditions to achieve better robustness using the thermal model are provided in analytical expressions and validated through simulation.

This dissertation is organized as follows:

- Chapter 1 has presented the background and motivation behind the proposed objectives of the dissertation, along with a detailed literature review. The objectives are presented with the specific contributions highlighted.

- Chapter 2 presents the development of a computationally-efficient thermal convection model for electric machines for low and medium rotor speeds and validated by CFD simulation and empirical models. This convection model can then be coupled with the thermal conduction model that has been previously constructed [15].

- Chapter 3 presents a computationally-efficient model for the AC resistance of solid conductors for AC PM machines considering skin and proximity effects. The generation of an impedance matrix allows the derivation of an analytical expression. Simulations and experimental measurements are provided to validate the proposed model.

- Chapter 4 presents an application of the thermal model: online loss estimation for electric machines. The advantages of the thermal model to construct the online loss estimator as opposed to an electrical model are analyzed via the steady-state sensitivity analysis. Simulation results show that the uncertainty in the thermal model parameters that are not estimated will lead to smaller estimation errors than the electrical model.

- Chapter 5 presents the conclusion of the dissertation, along with some related future work.

The works presented in this dissertation have been published in [84] and [85], or are under preparation for submission.

CHAPTER II

Computationally Efficient Heat Convection Model

2.1 Introduction

Accurate and computationally-efficient models for electric machines can play important roles in either real-time observers or vehicle simulations. Since the power and torque capabilities of an electric machine are significantly influenced by its inner temperature distribution, and over-temperature can damage electric machines, there is a need to have accurate and fast thermal models for electric machines.

In this chapter, a thermal model of electric machines will be presented, as shown in Fig. 2.1. This model includes two parts: thermal conduction and convection. Previous work established a computationally-efficient thermal conduction model [15]. A new computationally-efficient thermal convection model for the air domain inside electric machines, as shown in Fig. 1.4 is established. A case study consisting of an SMPM with a cooling jacket (UQM PowerPhase 145) is applied [14]. The nomenclature used in this chapter is provided in Table 2.1.

Table 2.1: Nomenclature for Convection Model

Thermal Model			
$\boldsymbol{D}$	FEA Mass Matrix	R_{gas}	Gas Constant
C_p	Constant Pressure Specific Heat	T	Temperature
C_v	Constant Volume Specific Heat	$\vec{v}$	Velocity
e	Inner Energy	$\vec{v}_b$	Boundary Velocity
$\vec{g}$	Gravity	$\vec{v}_m$	Solid Material Velocity
H	Heat Flux	α	Scaling Factor
k	Thermal Conductivity	ω_r	Rotor Angular Velocity
$\boldsymbol{K}$	FEA Stiffness Matrix	ρ	Density
$\vec{n}$	Normal Vector	μ	Dynamic Viscosity
p	Pressure	ν	Stack Length
p_{atm}	Atmospheric Pressure	$\vec{\vec{\tau}}$	Stress Tensor
P_{gauge}	Gauge Pressure	ϕ_μ	Viscous Heat Dissipation
q_{loss}	Power Loss Density		

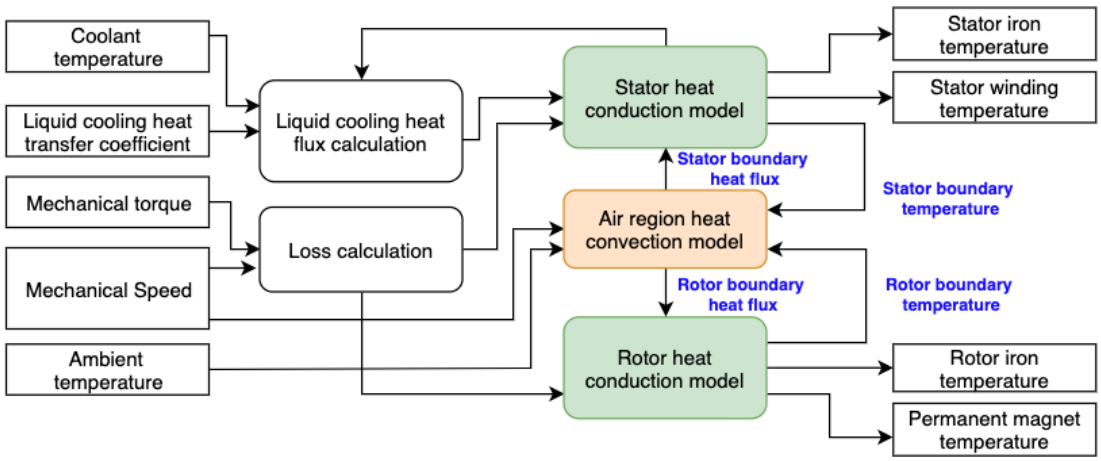

Figure 2.1: A Complete Thermal Model for Electric Machines

In Fig. 2.1, mechanical torque and mechanical speed are the inputs that determine the losses (heat generation) of SMPMs; while the coolant temperature, liquid cooling heat transfer coefficient, as well as ambient temperature are inputs which determine the boundary conditions of the thermal conduction model. SMPM losses are mainly

comprised of conduction loss and core loss. The conduction loss model will be further discussed in Chapter III.

2.2 Computationally-Efficient Thermal Conduction Model

The green blocks in Fig. 2.1 represent the SMPM stator and rotor thermal conduction models. Both conduction models have losses and boundary heat fluxes as inputs. The stator model also takes the cooling jacket's heat transfer coefficient as an input, which is implemented around the stator's outer surface. The outputs of the conduction models are the temperatures at locations of interest, including the windings, PM, and stator and rotor irons.

Heat conduction is captured by the following Partial Differential Equation (PDE):

$$C\frac{\partial T}{\partial t} - k\nabla^2 T = q_{loss}, \tag{2.1}$$

where T is the temperature, t is time, C is the specific heat. and q_{loss} is the power loss inside the machine.

This computationally-efficient heat conduction model [15] is based on eigenmode decomposition, and a case of the 3D FEA of a sector of SMPMs is studied. Using FEA techniques and considering convective boundary, the PDE shown in Eq.(2.1) can be discretized into an Ordinary Differential Equation (ODE) as:

$$\mathbf{D}\dot{\vec{T}} + \mathbf{K}\vec{T} = \vec{q} \tag{2.2}$$

where $\vec{T}$ is the nodal temperature of the FEA mesh, $\boldsymbol{D}$ is the mass matrix, $\boldsymbol{K}$ is the stiffness matrix, and $\vec{q}$ represents the excitation of the thermal model which can be expressed as:

$$\vec{q} = \sum_i \vec{f}_{loss,i} P_{loss,i} - \sum_j \vec{f}_{b,j} H_{b,j}, \tag{2.3}$$

where $P_{loss,i}$ stands for the total power loss for the i^{th} loss mechanism, for example, the conduction losses, and $H_{b,j}$ stands for the heat flux density for the j^{th} convective boundary. The vector $\vec{f}_{loss,i}$ is the normalized loss distribution vector for the i^{th} loss mechanism and $\vec{f}_{b,j}$ is the normalized flux distribution for the j^{th} convective boundary.

Previous work has applied an MOR to the linear model shown in Eq.(2.2) using eigenmodes [15]. The eigenmodes have been decomposed into dynamic and static modes according to corresponding time constants. The "slow" eigenmodes are then further divided into two categories referring to their Extent of Excitation (EOE), as shown in Fig. 2.2:

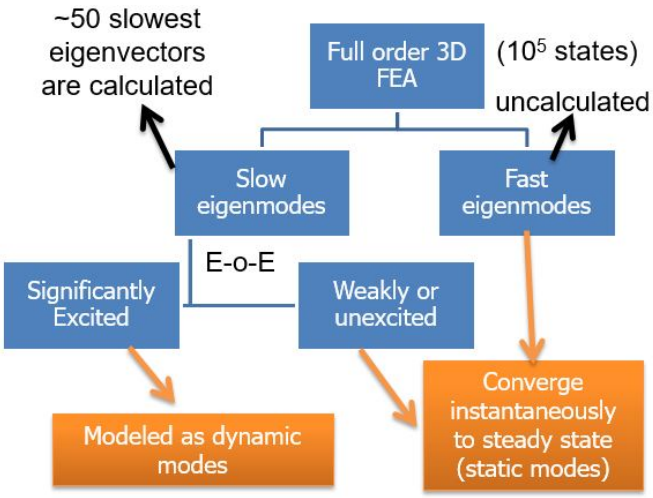

Figure 2.2: Order Reduction Process of FEA-Based Heat Conduction Model by Eigenmode Decomposition [15]

As the results of two steps of reduction, only a small portion of eigenmodes are kept, referred to as dynamic modes. This order reduction technique dramatically reduces the number of states compared to full order FEA. Thus the computation time is decreased by orders of magnitude. Experimental validation of this computationally-

efficient heat conduction model was achieved through a locked rotor test during driving cycles with satisfactory agreement [15]:

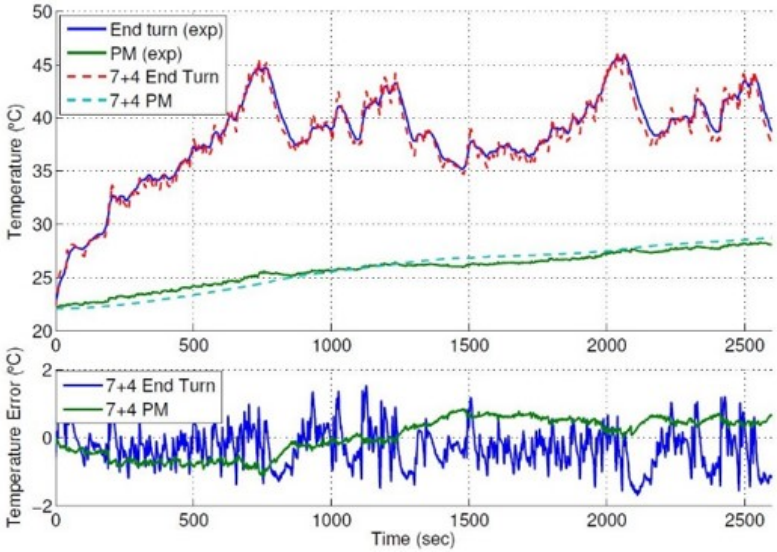

Figure 2.3: Experiment Validation of Locked Rotor Test of the Proposed Model [15]

2.3 Computationally-Efficient Thermal Convection Model

To completely model the machine's thermal behavior, a computationally-efficient heat convection model to capture the heat convection behavior with different rotor speeds is needed.

The orange block in Fig. 2.1 represents the thermal convection model. This model captures heat transfer due to convection of air inside the machine, as shown in Fig. 1.4. It takes the components' surface temperatures as inputs and calculates the total heat flux flowing into corresponding components as the outputs. For simplicity, it is assumed that temperature is uniformly distributed along the components' surfaces.

The governing equations for heat convection are shown in Eq.(2.4a), Eq.(2.4b)

and Eq.(2.4c):

$$\frac{\partial \rho}{\partial t} + \nabla \cdot (\rho \vec{v}) = 0, \quad \text{(Conservation of Mass)} \tag{2.4a}$$

$$\frac{\partial (\rho \vec{v})}{\partial t} + \nabla \cdot (\rho \vec{v} \vec{v}^T) + \nabla p - \nabla \cdot \vec{\vec{\tau}} - \rho \vec{g} = 0, \quad \text{(Conservation of Momentum)} \tag{2.4b}$$

$$\frac{\partial (\rho e)}{\partial t} + \nabla \cdot (\rho e \vec{v}) + p \nabla \cdot \vec{v} + \nabla \cdot \vec{q} - \phi_\mu = 0, \quad \text{(Conservation of Energy)}, \tag{2.4c}$$

where $\vec{v}$ is fluid velocity, $\vec{\vec{\tau}}$ is the stress tensor, p is the absolute pressure, $\vec{g}$ is gravity, e is the internal energy, and ϕ_μ is viscous heat dissipation.

The constitutive properties of air assumed in this work are shown in Eq.(2.5a), Eq.(2.5b), Eq.(2.5c), and Eq.(2.5d).

$$p - \rho R_{gas} T = 0, \quad \text{(Ideal Gas Law)} \tag{2.5a}$$

$$e = C_v T, \quad \text{(Calorically Perfect)}, \tag{2.5b}$$

$$\vec{\vec{\tau}} = \mu \big[(\nabla \vec{v} + \nabla \vec{v}^T - \frac{2}{3} (\nabla \cdot \vec{v} \mathbf{I})) \big], \quad \text{(Constant Viscosity)} \tag{2.5c}$$

$$\vec{q} = -k \nabla T, \quad \text{(Constant Thermal Conductivity)} \tag{2.5d}$$

where R_{gas} is the ideal gas constant, C_v is the constant volume-specific heat, and $\vec{q}$ is the local heat flux density. In terms of excitation assumptions, heat transfer induced by gravity will be ignored ($\vec{g} = 0$), and heat generation in the air due to viscosity is also ignored ($\phi_\mu = 0$) [16].

The absolute pressure (p) consists of two parts, the atmospheric pressure (p_{atm}) and the gauge pressure (p_{gauge}), as shown in Eq.(2.6a). Since electric machines are usually not perfectly sealed, we assumed that the atmospheric pressure is constant. We also assume that the air region's gauge pressure inside electric machines is small compared with the atmospheric pressure. These assumptions lead to the approximations provided in Eqs.(2.6b) and (2.6c).

$$p = p_{atm} + p_{gauge}, \tag{2.6a}$$

$$\nabla p \approx \nabla p_{gauge}, \tag{2.6b}$$

$$p \approx p_{atm}. \tag{2.6c}$$

Based on these assumptions, the conservation of momentum and energy equations, as well as the ideal gas law have been simplified to the following:

$$\frac{\partial \rho}{\partial t} + \nabla \cdot (\rho \vec{v}) = 0 \tag{2.7a}$$

$$\frac{\partial (\rho \vec{v})}{\partial t} + \nabla \cdot (\rho \vec{v} \vec{v}^T) + \nabla p_{gauge} - \mu \nabla \cdot \left[(\nabla \vec{v} + \nabla \vec{v}^T - \frac{2}{3} (\nabla \cdot \vec{v} \mathbf{I})) \right] = 0 \tag{2.7b}$$

$$C_v \frac{\partial (\rho T)}{\partial t} + C_v \nabla \cdot (\rho T \vec{v}) + p_{atm} \nabla \cdot \vec{v} - k \nabla \cdot (\nabla T) = 0 \tag{2.7c}$$

$$p_{atm} - \rho R_{gas} T = 0 \tag{2.7d}$$

Claim: the governing equations Eq.(2.7a), Eq.(2.7b), Eq.(2.7c) and Eq.(2.7d) are still satisfied when the following scalings are applied:

$$T_\alpha = \alpha T, \tag{2.8a}$$

$$\rho_\alpha = \frac{1}{\alpha} \rho, \tag{2.8b}$$

$$p_{gauge-\alpha} = \alpha p_{gauge}, \tag{2.8c}$$

$$\vec{v}_\alpha = \alpha \vec{v}, \tag{2.8d}$$

$$t_\alpha = \frac{1}{\alpha} t, \tag{2.8e}$$

where α is the scaling factor, and the α subscript designates the variable after scaling.

The governing equations when the scaling applied can be reverted to their original

form. The proof is shown below:

$$\begin{aligned}\frac{\partial \rho_\alpha}{\partial t_\alpha} + \nabla \cdot (\rho_\alpha \vec{v}_\alpha) &= \frac{\partial (\frac{1}{\alpha}\rho)}{\partial (\frac{1}{\alpha} t)} + \nabla \cdot \big((\frac{1}{\cancel{\alpha}}\rho)(\cancel{\alpha}\vec{v}) \big) \\ &= \frac{\partial \rho}{\partial t} + \nabla \cdot (\rho \vec{v}) = 0\end{aligned} \tag{2.9}$$

$$\begin{aligned}&\frac{\partial (\rho_\alpha \vec{v}_\alpha)}{\partial t_\alpha} + \nabla \cdot (\rho_\alpha \vec{v}_\alpha \vec{v}_\alpha^T) + \nabla p_{gauge-\alpha} - \nu \nabla \cdot \big[(\nabla \vec{v}_\alpha + \nabla \vec{v}_\alpha^T - \frac{2}{3}\big(\nabla \cdot \vec{v}_\alpha \mathbf{I}\big)) \big] \\ =&\frac{\partial (\frac{1}{\alpha}\rho)(\alpha \vec{v})}{\partial (\frac{1}{\alpha} t)} + \nabla \cdot ((\frac{1}{\cancel{\alpha}}\rho)(\cancel{\alpha}\vec{v})(\alpha \vec{v}^T)) + \\ &\qquad \alpha \nabla p_{gauge} - \nu \nabla \cdot \big[(\nabla(\alpha \vec{v}) + \nabla(\alpha \vec{v}^T) - \frac{2}{3}(\nabla \cdot (\alpha \vec{v}) \mathbf{I})) \big] \\ =&\alpha \left(\frac{\partial (\rho \vec{v})}{\partial t} + \nabla \cdot (\rho \vec{v} \vec{v}^T) + \nabla p_{gauge} - \nu \nabla \cdot \big[(\nabla \vec{v} + \nabla \vec{v}^T - \frac{2}{3}\big(\nabla \cdot \vec{v} \mathbf{I}\big)) \big] \right) = 0\end{aligned} \tag{2.10}$$

$$\begin{aligned}&c_v \frac{\partial (\rho_\alpha)(T_\alpha)}{\partial t_\alpha} + c_v \nabla \cdot (\rho_\alpha T_\alpha \vec{v}_\alpha) + p_{atm} \nabla \cdot \vec{v}_\alpha - k \nabla \cdot (\nabla T_\alpha) \\ =&c_v \frac{\partial (\frac{1}{\alpha}\rho)(\alpha T)}{\partial \frac{1}{\alpha} t} + c_v \nabla \cdot ((\frac{1}{\cancel{\alpha}}\rho)(\cancel{\alpha} T)(\alpha \vec{v})) + p_{atm} \nabla \cdot (\alpha \vec{v}) - k \nabla \cdot (\nabla(\alpha T)) \\ =&\alpha \left(c_v \frac{\partial (\rho T)}{\partial t} + c_v \nabla \cdot (\rho T_\alpha \vec{v}) + p_{atm} \nabla \cdot \vec{v} - k \nabla \cdot (\nabla T) \right) = 0\end{aligned} \tag{2.11}$$

$$p_{atm} - (\rho_\alpha) R_{gas}(T_\alpha) = p_{atm} - (\frac{1}{\cancel{\alpha}}\rho) R(\cancel{\alpha} T) = p_{atm} - \rho R_{gas} T = 0 \tag{2.12}$$

The scaling relation is similar but different from Reynolds scaling. Reynolds scaling assumes incompressible flow, but this homogeneity property uses the ideal gas law as the fluid density model, which is more accurate since air density varies significantly with temperature, as shown in Fig. 1.6.

Due to no-slip conditions at the boundary between air and machine solid components, the velocity is continuous between boundary and material, as shown in Eq.(2.13):

$$\vec{v}_b = \vec{v}_m, \tag{2.13}$$

where $\vec{v}_b$ is the fluid velocity at solid/fluid boundary, $\vec{v}_m$ is the velocity of solid material.

Thus, to be consistent with the velocity scaling relation, the angular velocity of the rotor must also be scaled with α, shown in Eq.(2.14):

$$w_{r,\alpha} = \alpha w_r \tag{2.14}$$

Transient flow solutions are, in most cases, unnecessary, as time-averaging models give reasonably close results in a fraction of the time [16]. The proposed heat convection mapping therefore outputs time-averaged, steady-state net heat fluxes at the component surfaces, as a function of time-averaged component boundary temperatures and rotor angular speed, as shown in Eq.(2.15):

$$\vec{H} = f\left(\vec{T}, w_r\right), \tag{2.15}$$

where $\vec{T}$ is a vector of components' temperatures, and $\vec{H}$ is the steady-state net heat flux vector for all component surfaces. Here in Eq.(2.15), the heat flux and temperature vectors are of the length of n, which is the number of machine components. We assume each component has a uniform temperature profile, and we calculate the total

heat flux into or out of each component.

The heat flux at each component surface is due solely to conduction ($\vec{v} \cdot \vec{n} = 0$) can therefore be expressed as in Eq.(2.16):

$$H_{comp} = \int_s -k\Delta T \cdot \vec{n} dS \tag{2.16}$$

where H_{comp} is the steady-state net heat flux for one component and $\vec{n}$ is the surface normal vector. The total heat flux for each component after the scaling can be shown in Eq.(2.17):

$$H_{comp,\alpha} = \int_s -k\Delta(\alpha T) \cdot \vec{n} dS = \alpha H_{comp} \tag{2.17}$$

Thus the mapping from the component temperatures and rotor speed to total component surface heat flux satisfies the homogeneity property, as shown in Eq.(2.18):

$$\alpha\vec{H} = f\left(\alpha\vec{T}, \alpha w_r\right) \tag{2.18}$$

Note that the mapping from temperatures and rotor speed to corresponding total heat flux is not linear. It does not satisfy the superposition property, which is another criterion for linearity.

It is worth noting that, if a constant density model for air is assumed (instead of the ideal gas law model), the velocity field and temperature field solved from the governing equations shown in Eq.(2.9), Eq.(2.10) and Eq.(2.11) are decoupled. As a result, the velocity field can be calculated merely by solving the conservation of mass and momentum equations with velocity boundary conditions. In this case, the Reynolds

number is only a function of speed [86]. Most literature assumes incompressible flow and models the surface heat convection coefficient as a function of rotor speed, so the total heat flux is a linear function of temperature differences for a given rotor speed, shown as [23-28], [30-31]. However, this does not hold for our application since air density variation can be substantial due to the significant temperature range during normal operation of electric machines, as shown in Fig. 1.6, especially for electric machines with large torque capability. In this case, the Reynolds number will also be influenced by temperature, and the ideal gas law is more accurate.

2.3.1 Heat Convection Model for Low Rotor Speed

For low rotor speeds, the air flow is laminar, so 2D CFD simulations are sufficient to capture the flow behavior. For the air gap between the stator and rotor, planar 2D simulations are conducted, while for the end region between the end-cap housing and inner stator/rotor surfaces, axisymmetric 2D simulations are conducted.

Some of the simulation profiles are shown in Figs. 2.4 and 2.5, with air properties shown in Table 2.3, boundary conditions shown in Table 2.3, and simulation under-relaxation factors which are used to partially update the state after each iteration to reduce solution oscillation [87] is shown in Table 2.4

Density	C_p	k	μ	Molecular Weight
Ideal Gas Law	1006.43 $J/kg \cdot K$	0.0242 $w/m \cdot K$	1.7894×10^{-5} $kg/m \cdot s$	28.966 g/mol

Table 2.2: CFD Simulation Air Properties

Model	T_r	T_s	$T_{winding}$	w_r	T_{pm}	$T_{aluminum}$	$T_{housing}$
Air Gap	338K	383K	388K	50rpm	N/A	N/A	N/A
End Region	353K	408K	413K	150rpm	358K	333K	293K

Table 2.3: Low-Speed 2D Boundary Conditions

p	ρ	Body Force	Momentum	Turb Kinetic Energy	Turb Dissi Rate	Turb Viscosity	Energy
0.3	45	1	0.4	0.8	0.8	1	1

Table 2.4: 2D Simulation Under-Relaxation Factor Setup [87]

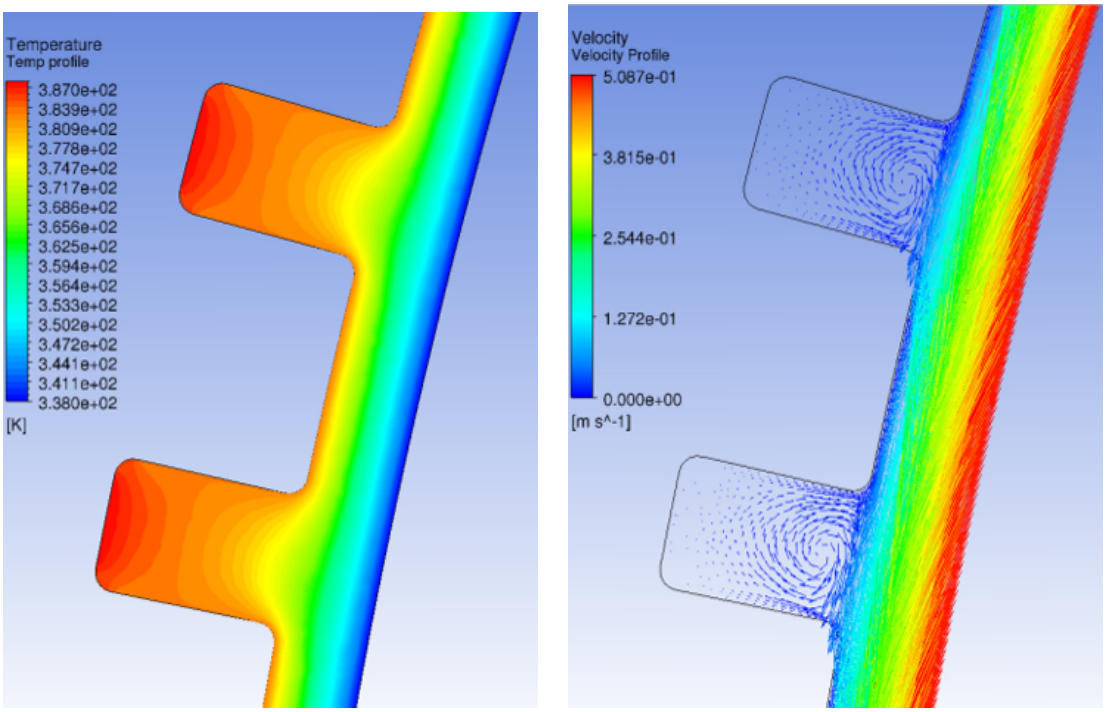

(a) Air Gap Temperature Profile (b) Air Gap Velocity Profile

Figure 2.4: 2D Air Gap Planar Simulations Profiles

A homogeneity test has been carried out for 2D planar simulations for the air gap and 2D axisymmetric simulations for the end region, as shown in Table 2.5. First, the base simulation is conducted ($\vec{H} = f(\vec{T}, \omega_r)$). Then, another simulation with the scaled boundary conditions is conducted ($\vec{H}_\alpha = f(\alpha\vec{T}, \alpha\omega_r)$). The scaled result of the base simulation ($\alpha\vec{H}$) is then compared with the simulation results with scaled boundary conditions ($\vec{H}_\alpha$). The Maximum Relative Error (MRE) is defined as Eq.(2.19).

$$MRE = max\left|\frac{H_{prop} - H_{sim}}{H_{sim}}\right| \times 100\% = max\left|\frac{\alpha H - H_\alpha}{H_\alpha}\right| \times 100\%, \tag{2.19}$$

where H_{prop} is the heat flux calculated by scaling the base simulation, and H_{sim} is the heat flux calculated from simulation.

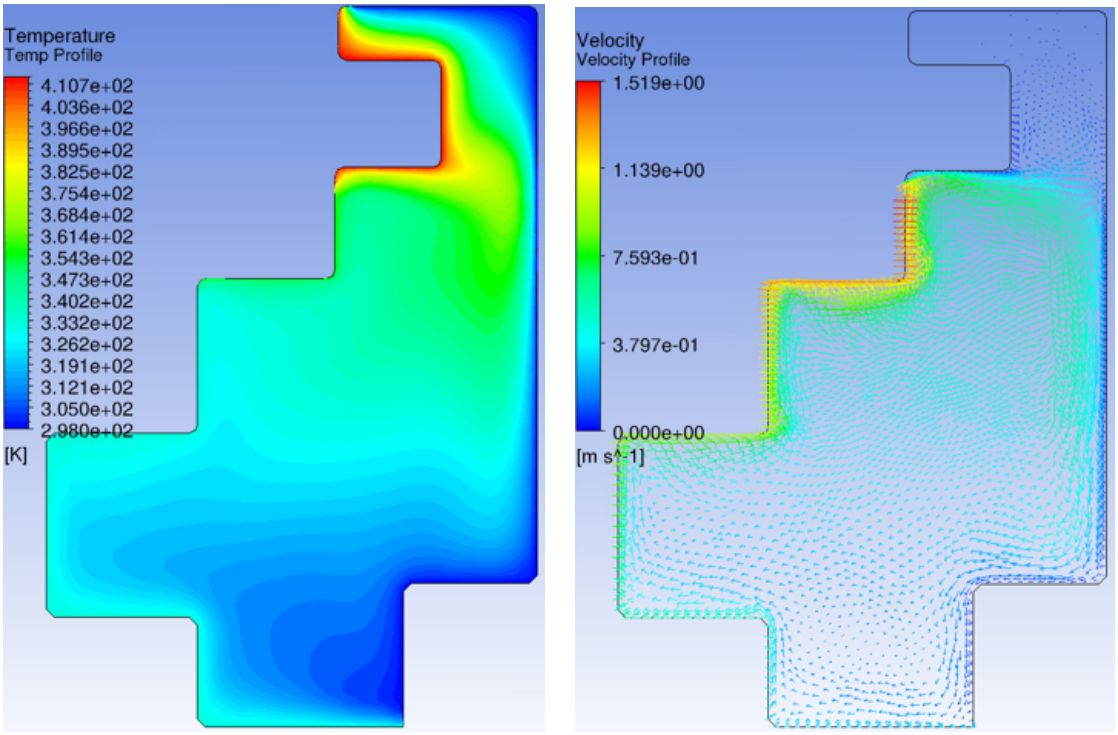

(a) End Region Temperature Profile (b) End Region Velocity Profile

Figure 2.5: 2D End Region Axisymmetric Simulations Profiles

Model	Air Gap	End Region
# simulations	40	34
Temperature range	$100 \sim 850K$	$100 \sim 3880K$
Rotor speed range	$25 \sim 400rpm$	$25 \sim 500rpm$
MRE	$2 \times 10^{-3}\%$	$9 \times 10^{-3}\%$

Table 2.5: Homogeneity Test for 2D planar Air gap model and 2D axisymmetric End region model

It can be seen that the maximum relative errors are less than $10^{-4}\%$. Hence, this property holds.

The homogeneity property dramatically reduces the space of possible functions that map temperatures and speed to heat flux. In general, the heat flux mapping will take the general form Eq.(2.20):

$$\prod_i (T\omega_r)_i^{e_i}, \tag{2.20}$$

where $T\omega_r$ is either a temperature T or the rotor speed ω_r (as inputs of the mapping), and the exponents e_i satisfy:

$$\sum_i e_i = 1 \tag{2.21}$$

Aside from this property, the mapping from temperatures and rotor speed to corresponding heat flux also has to possess some other properties.

The first one should be linearity when $w_r = 0$. When the rotor is fixed, only heat conduction occurs in the air domain. This linearity test has also been carried out for both 2D planar simulations for the air gap and 2D axisymmetric simulations for the end region, as shown in Table 2.6.

Model	Air Gap/End Region
# simulations	28
Temperature range	$258 \sim 413K$
Rotor speed range	0 rpm
MRE	$2 \times 10^{-5}\%$

Table 2.6: Linearity Test for 2D Planar Air Gap Model and 2D Axisymmetric End Region Model

The second property of the mapping is that no heat flux should be observed when all components are of the same temperatures, since heat transfer is due to the temperature differences. This is what the zero temperature gradient test does: all components are set to have the same temperatures, heat flux for corresponding components are recorded for different rotor speeds, as shown in Table 2.7.

Model	Air Gap/End Region
# simulations	6
Temperature range	$280 \sim 400K$
Rotor speed range	$150 \sim 300rpm$
Max relative error	$10^{-4}/10^{0\sim2}$

Table 2.7: Zero Temperature Gradient Test for 2D Planar Air Gap Model and 2D Axisymmetric End Region Model

According to the discovered homogeneity property as well as the features tested above, the mapping from component temperatures and rotor speed to a component heat flux can be expressed in Eq.(2.22):

$$H_{comp} = \sum_{i=1}^{n-1} \sum_{j=i+1}^{n} \alpha_{ij}(T_i - T_j) + \sum_{i=1}^{n-1} \sum_{j=i+1}^{n} \beta_{ij}(T_i^{e_{ij}} - T_j^{e_{ij}})\omega_r^{1-e_{ij}}, \tag{2.22}$$

where α, β are coefficients and e are exponents for one component that needs to be determined.

All exponents and coefficients for the both air gap and end region models have been determined using the fmincon routine in MATLAB and the least squares method. Specifically, CFD simulation data covering the temperature and rotor speed range are fed into MATLAB global search algorithms *GlobalSearch* for a range of exponents trial. The group of exponents with the minimum least square errors of heat fluxes of all components compared with simulated heat fluxes will be chosen. The corresponding coefficients achieve the minimum least square errors of fed simulation data sets.

The pseudo codes to determine the model parameters are shown as follows:

- *Load zero speed data* $\vec{H}_0, \vec{T}_0$

  Calculate α_{ij} *by least squares method*

- *Load low speed data* $\vec{H}, \vec{T}, \omega_r$

  Separate heat fluxes due to rotation $H_{sim} = H - \sum_i^{n-1} \sum_j^n \alpha_{ij}(T_i - T_j)$

- *GlabalSearch to minimize* $MRE(\beta, e)$

  opts = optimoptions(@fmincon,'Algorithm','interior-point');

  problem = createOptimProblem('fmincon','objective',@(e),MRE,'e0','lb',...

  'ub','options',opts);

  gs = GlobalSearch;

  [e,∼] = run(gs,problem);

  Calculate β_{ij} *by least squares method*

The MRE of the proposed model have been compared with a quadratic model shown in Eq.(2.23), which follows all the assumptions listed above except for the homogeneity property.

$$H_{comp} = \sum_{i=1}^{n-1} \sum_{j=i+1}^{n} \alpha_{ij}(T_i - T_j) + \sum_{i=1}^{n-1} \sum_{j=i+1}^{n} \beta_{ij}(T_i - T_j)\omega_r \tag{2.23}$$

Parameters α_{ij} and β_{ij} are determined by least squares method for the quadratic model.

The comparison of MRE using different models when compared with CFD simulation results is shown in Table 2.8 and Fig. 2.6.

MRE	Air Gap Model			End Region Model			
	Rotor	Stator	Winding	Housing	Rotor	Stator	Winding
Proposed Model	0.21%	0.23%	0.35%	0.68%	1.85%	0.38%	0.65%
Quadratic Model	4.78%	5.11%	1.08%	13.11%	34.34%	9.34%	8.07%

Table 2.8: Comparison of Proposed Model and Quadratic Model

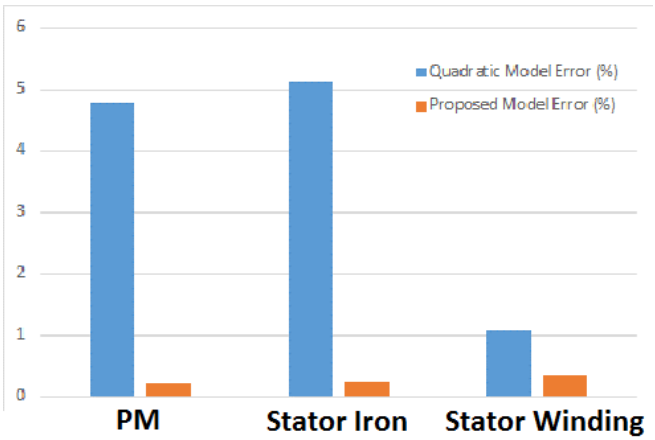

(a) Comparison of 2D Planer Air Gap Model

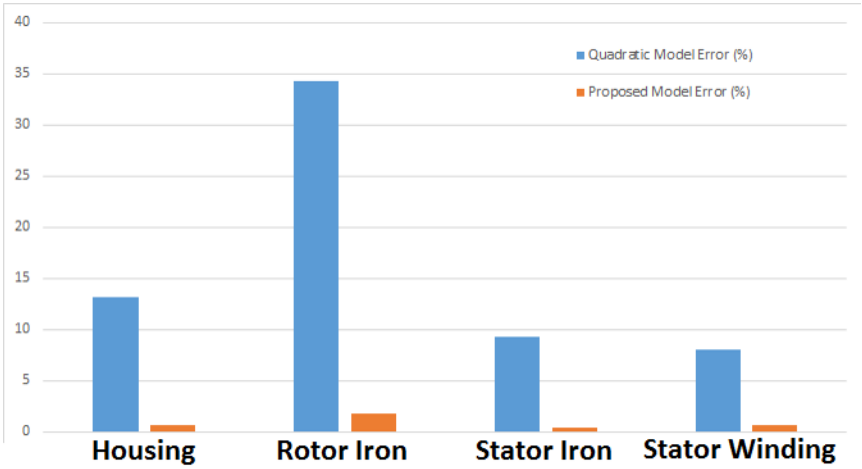

(b) Comparison of 2D Axisymmetric End Region Model

Figure 2.6: 2D Simulation Comparison of MRE of Proposed Model and Quadratic Model for Low Rotor Speed

From the comparison between the proposed model and the second-order model, it can be concluded that, with the proposed model, the maximum relative error is typically reduced by over an order of magnitude. The maximum relative error of winding heat flux of both the proposed model and the quadratic model is small. This is because the heat flux flowing out of stator winding is much smaller than total flux from the stator to rotor ($\sim$ 10% for the air gap model and $\sim$ 6% for the end region model).

2.3.2 Heat Convection Model for Medium Rotor Speed

In a typical electric machine geometry, the rotor and stator are two co-axial annular cylinders. In the air gap formed by those cylinders, a special flow phenomenon called Taylor Vortices comes into existence at particular rotating speeds of either the inner or outer cylinder, or both cylinders.

An inner rotating cylinder with a stationary outer annular cylinder is studied for Taylor Vortices based on the typical electric machine structure. It has been shown in [18] that, when the inner cylinder achieves an angular speed above a certain threshold, a flow emerges characterized by axisymmetric axially periodic vortices. As the inner cylinder's rotating speed increases, the phenomena propagates into the next stage of Taylor Vortices, called wavy vortex flow, as shown in Fig. 2.7. As the angular velocity continues to increase, the flow will eventually develop into turbulence. It can be seen that a periodic flow behavior along the axial direction exists which enhances the heat transfer between the cylinders. Fenot *et al.* [88] did a detailed review for both Taylor-Couette and Taylor-Couette-Poiseulle flows. The flow regimes over a wide speed range are presented, with the existing correlations for Nusselt number and the influences of Taylor vortices on heat transfer. The results provided in [20] shows that the presence of Taylor vortices in the air gap flow enhance the overall heat transfer, and that the heat transfer coefficient increases with rotation speed and air gap length.

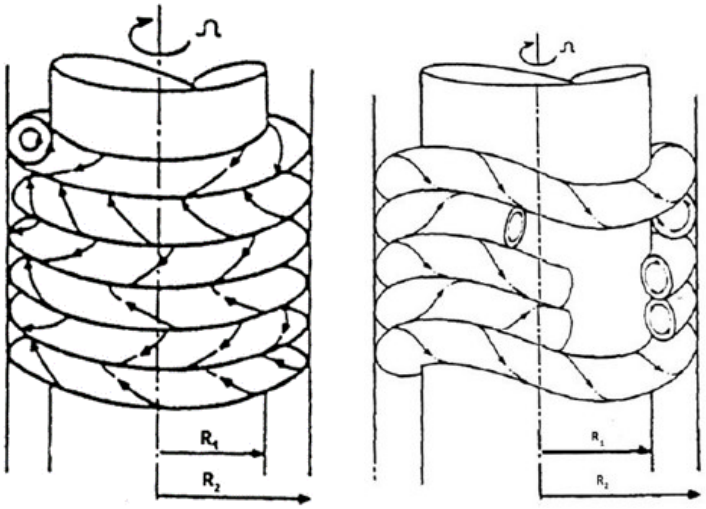

(a) Taylor Vortices Stage 1 (b) Taylor Vortices Stage 2

Figure 2.7: Taylor Vortices within the Speed Range from [88]

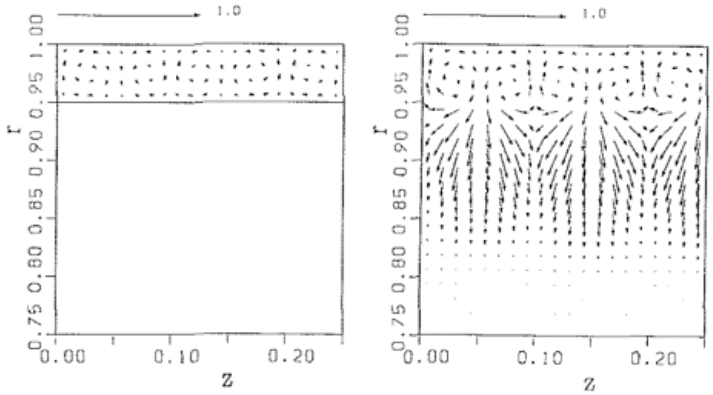

Figure 2.8: Taylor Vortices in Axisymmetric Plane with Slots on Rotor Surface from [31]

In real electric machines, the stator surface is not smooth due to the slots where the winding coils are placed, which will influence heat transfer as shown in Fig. 2.8. Periodic behavior can still be observed in the gap between stator and rotor. However, the flow also behaves with repeated forms within slots, which requires 3D simulations to capture accurately.

2.3.2.1 2D Simulations for medium rotor speed

For simplicity, 2D axisymmetric time-averaged simulations of two smooth cylinders are considered initially, with the boundary conditions provided in Table 2.9. Time-averaged simulations may not be able to capture detailed flow behavior, but they are sufficient to model the macroscopic heat transfer phenomenon [16] with close results at a fraction of time compared with Direct Numerical Simulation (DNS). Note that these simulations are not conducted for the UQM machine air gap geometry ($97.5mm \sim 98.6mm$), but larger air gap ($97.5mm \sim 101.8mm$), where the radius of outer cylinder ($101.8mm$) actually represents the position of the closest winding coil, as shown in Fig.1.5.

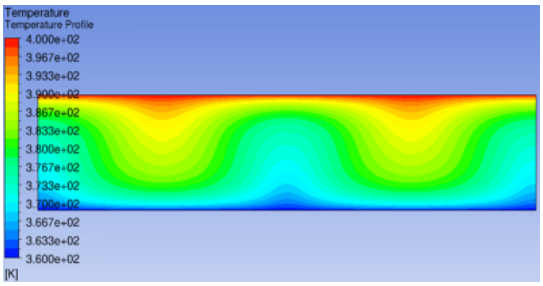

Figure 2.9: Temperature Profile of 2D Simulations for Taylor Vortex Effects

$T_r(K)$	$T_s(K)$	$w_r(rpm)$
360	400	600

Table 2.9: 2D Simulations Boundary Conditions for Taylor Vortices

The lower boundary of the speed range for Taylor Vortices can be calculated as shown in Eq.(2.24) [31].

$$Re_* = \frac{w_r R_r (R_s - R_r)}{\nu} = 185 \Longrightarrow w_r > 31.05 rad/sec \tag{2.24}$$

Based on the comparison provided in [31], $Re_* = 185$ is a critical Reynolds number. Below this critical number, 2D and 3D models have almost identical temperature and

velocity profiles with acceptable errors; above this critical number, 2D and 3D results deviate.

It is shown that the homogeneity property is still satisfied when Taylor Vortices are present. A similar homogeneity property test shown in Section 2.3.1 has been carried out for the air gap model under these conditions, as shown in Table 2.10.

Model	Air Gap
# simulations	9
Temperature range	$268 \sim 444K$
Rotor speed range	$700 \sim 840rpm$
Scaling factor range	$0.8 \sim 1.2$
Max relative error	4.2×10^{-5}

Table 2.10: 2D Homogeneity Test with Taylor Vortices in Air Gap

To include the critical Taylor's number into the mapping, an additional term has been added, as shown in Eq.(2.25).

$$\begin{aligned} Ta \sim & \frac{\omega_r}{\nu} \sim \omega\rho \sim \frac{\omega_r}{T} \\ & \Rightarrow \frac{\omega_r}{T} \end{aligned} \tag{2.25}$$

It can be seen that by adding the term, the proposed model in Eq.(2.26), still satisfies the homogeneity property of the general form shown in Eq.(2.21).

$$H_{comp} = \left(\frac{\omega_r}{\bar{T}}\right)^x \sum_{k=1}^{n} \sum_{i=1}^{n-1} \sum_{j=i+1}^{n} \gamma_{ijk} T_k^{e_{1,ijk}} (T_i^{e_{2,ijk}} - T_j^{e_{2,ijk}}) \omega_r^{1-e_{1,ijk}-e_{2,ijk}} \tag{2.26}$$

where $\bar{T}$ is the fluid temperature, approximated by averaged boundary temperatures. The maximum errors of the proposed model have been compared with a third-order model, similar to the quadratic model formulation in laminar flow modeling, which follows all the assumptions, except for the homogeneity property, as shown in Eq.(2.27),

and the comparison is shown in Table 2.11 and Fig. 2.10.

$$H_{comp} = \left(\frac{\omega_r}{\bar{T}}\right)^x \sum_{x=1}^{n} \sum_{i=1}^{n-1} \sum_{j=i+1}^{n} \gamma_{ijk} T_k (T_i - T_j) \omega_r \tag{2.27}$$

Similar to the modeling of laminar flow, all coefficients for both models and exponents for the proposed model have been determined by fmincon routined in MATLAB and the least square method.

It is also shown that using homogeneity property, the MRE has been reduced by more than an order of magnitude.

MRE	2D Air Gap
Proposed Model	2.2%
Third Order Model	23.2%

Table 2.11: Comparison of Proposed Model and Third-Order Model

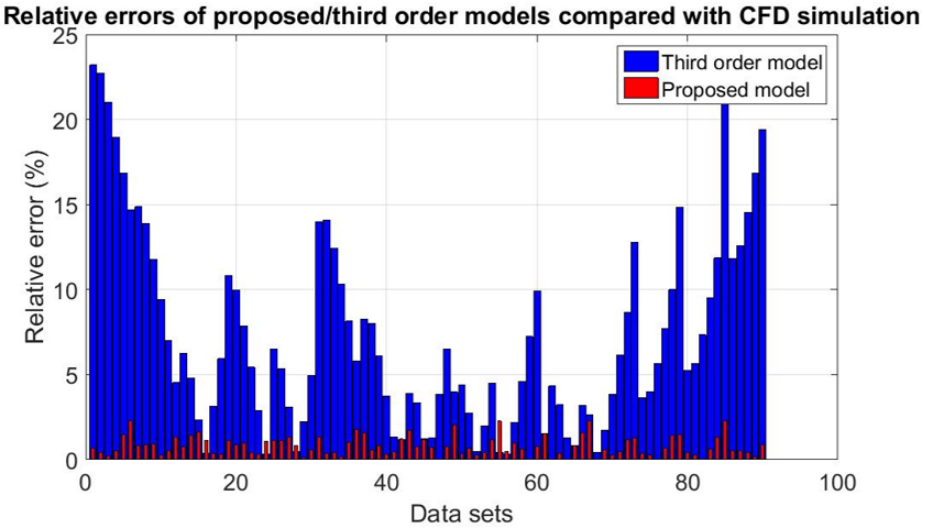

Figure 2.10: 2D Comparison between Proposed Model and Third Order Model for Medium Rotor Speed

2.3.2.2 3D Simulations for medium rotor speed

3D time-averaged simulations were conducted to consider the influence of stator slots, with air gap length (2.5mm). Temperature profile is shown in Fig. 2.11 with the boundary conditions shown in Table 2.12.

$T_r(K)$	$T_s(K)$	$T_{winding}(K)$	$w_r(rpm)$
300	330	335	450

Table 2.12: 3D Simulations Boundary Conditions for 3D Taylor Vortices (2.5mm)

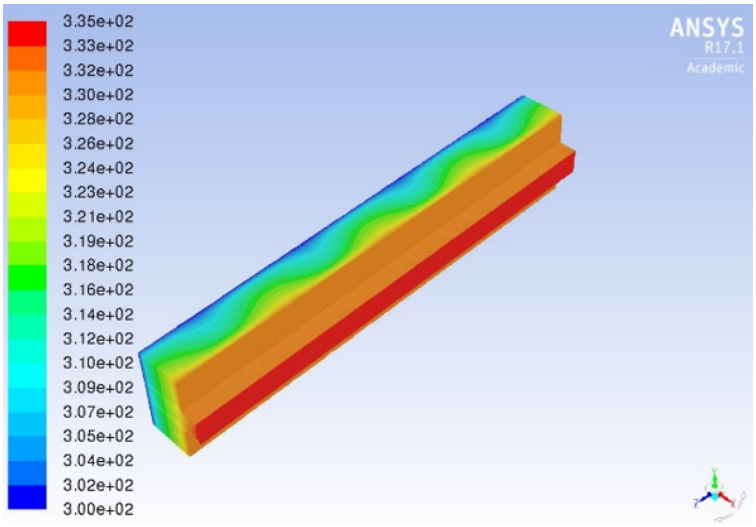

Figure 2.11: Temperature Profile of 3D Simulations for Taylor Vortex Effect

Using a similar fitting method, the maximum error of the proposed model is compared with the third-order model, as shown in Table 2.13 and Fig. 2.12.

MRE	H_{rotor}	H_{stator}	$H_{winding}$
Proposed Model	0.25%	0.28%	0.28%
Third Order Model	43.04%	508.71%	44.43%

Table 2.13: MRE Comparison between the Proposed Model with the Third-Order Model of 3D Medium Speed Simulations

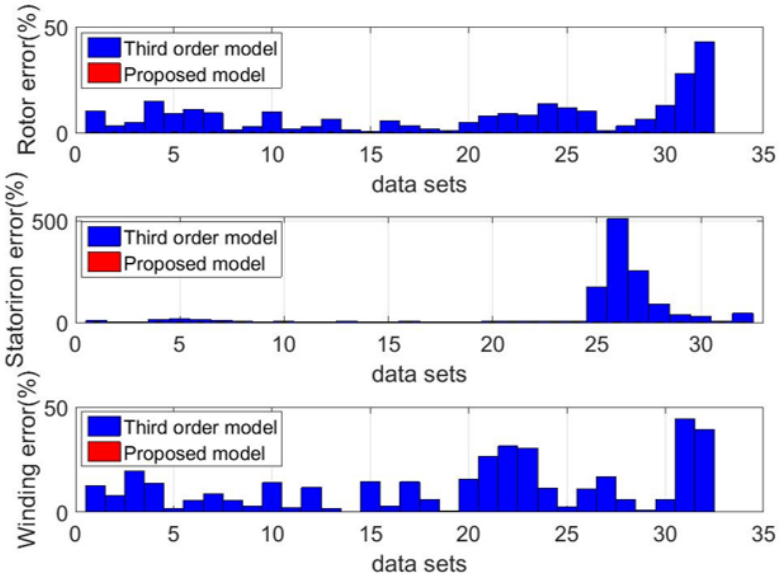

(a) 3D MRE Comparison: the Proposed Model has Relative Small Error Comparing to the Third Order Model. A Zoom in Figure is Shown Below

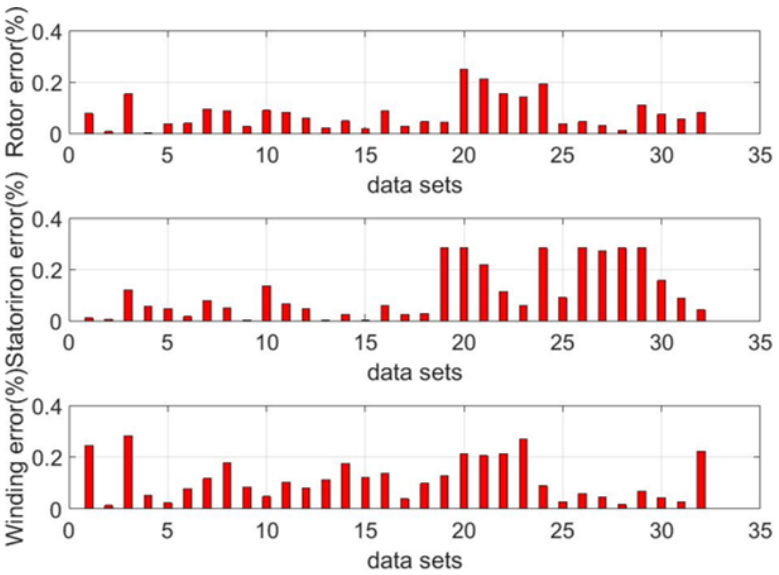

(b) 3D MRE Comparison Zoom in, with Errors from Third Order Model Omitted for Clearer View

Figure 2.12: 3D MRE Comparison of the Proposed Model and the Third-Order Model

It has been shown that initial results with a homogeneous time-averaged heat flux model show significantly better accuracy than a third-order model compared with full-order CFD simulation results, with maximum errors of 2.2% for 2D and 0.34% for 3D.

2.4 Discussion

2.4.1 Computation Time

The proposed model has a computation time less than 10 ms to capture heat convection for one operating point for both the air gap and end region model on a computer with an Intel(R) Xeon(R) @ 3.2GHz CPU of 4 cores. Simultaneously, a full order 2D CFD simulation takes $5 \sim 10$ minutes depending on rotor speed and initial conditions. Full order 3D CFD simulations to capture Taylor Vortices take a much longer time to finish, thus can not be performed on the same CPU. All 3D simulations are conducted on the MPEL8 server (the server provided by Michigan Power and Energy Lab), using parallel computing over 80 cores. The computation time ranges from tens of hours to several days, depending on rotor speed and initial conditions.

2.4.2 Simulation Requirements

Due to the homogeneity property used to generate the mapping, which places constraints on the mapping structure, the number of needed CFD simulations have been reduced. For example, to determine the model parameters, the air gap and end region's thermal convection models for low rotor speed used 55 CFD simulations. The heat fluxes calculated from this proposed model are then compared with 300 CFD simulations with good agreement shown in Table 2.8. For medium rotor speed, due to the considerable computation time required by 3D simulations, all simulation data is used to construct the mapping.

2.5 Conclusion

A computationally-efficient thermal convection model has been built for low and medium speed for the air gap and low speed for the end region. The homogeneity

property proven in fundamental governing equations and validated through simulations is exploited to construct the mapping from component temperatures and rotor speed to component total heat flux. This property is similar to Reynolds Scaling, but Reynolds Scaling assumes incompressible flow while this property uses the ideal gas law, which is more accurate over a larger temperature range. This property is used to construct the model, and only a relatively small number of CFD simulations are needed to avoid hundreds of time-consuming CFD simulations that cover all the operating conditions. The phenomena of Taylor Vortices is investigated when modeling air gap heat convection for both smooth and non-smooth stator surfaces.

CHAPTER III

Modeling of AC Resistance in Stator Winding Slot

3.1 Introduction

One important component of the thermal model for electric machines is power loss estimation (which acts as the heat generation term of the heat conduction equation). Several machine components have significant heat generation, such as conduction loss in the machine winding, hysteresis and eddy current losses in permanent magnets and iron, and friction loss in the bearing. Among these elements, conduction loss is dominant. Conduction loss estimation accuracy is largely affected by the modeling of resistance. Due to phenomena such as the skin and proximity effects, current and resistance will be re-distributed in the winding as a function of frequency, causing the effective resistance to increase.

In this chapter, a model of AC resistance in the slot of an AC stator based on magnetoquasistatic analysis will be presented. We assume the slot is rectangular in nature (in practice, the slot can be either rectangular or scalloped).

3.2 Derivation

The nomenclature used in this chapter is provided in Table 3.1:

Electric machines are typically analyzed using a magnetoquasistatic formulation

Table 3.1: Nomenclature for AC Resistance Model

Variables			
$\vec{A}$	Magnetic Vector Potential	N_{pp}	Number of Parallel Paths
$\vec{B}$	Magnetic Flux Density	N_s	Number of Slots
$\vec{E}$	Electric Field Strength	n	Number of Data Points
f_e	Electrical Frequency	R	Resistance
h_t	Height of Winding Turn	t	Time
$\vec{H}$	Magnetic Field Strength	w_t	Width of Winding Turn
I	Current	ϕ	Electrical Scalar Potential
$\vec{J}$	Current Density	σ	Electrical Conductivity
$l_{endturn}$	Endturn Length	δ	Skin Depth
l_{stack}	Stack Length	μ_0	Free Space Permeability
$\vec{M}$	Material Magnetization	μ_r	Relative Permeability
N	Number of Turns	ω	Electrical Angular Velocity
N_p	Number of Poles		

of Maxwell's equations [89]. The geometry of the cross-section of a stator slot with rectangle conductors is shown in Fig. 3.1, neglecting any space between each turn. The spacing does not affect the AC resistance, as proved at the end of this chapter in Section A. Intuitively this is because the magnetic field boundary conditions for each conductor will not change when gaps are introduced.

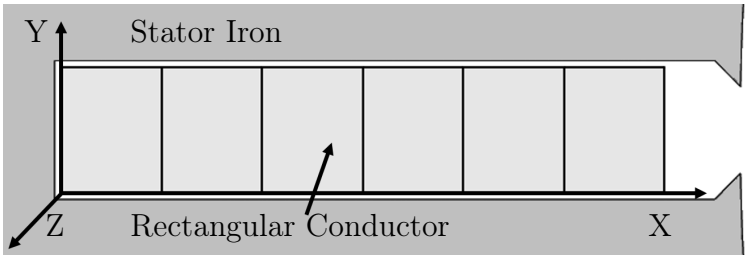

Figure 3.1: Simplified Winding Placement in a Slot (Rectangular Conductor)

3.2.1 Governing Equations

Magnetoquasistatic (MQS) is a good and accurate approximation to Maxwell's equations in the spatial and temporal scales of interest of electric machines [90]. The

fundamental partial differential equations which establish MQS behavior are:

$$\nabla \times \vec{H} = \vec{J}, \qquad \text{Ampere's Law} \tag{3.1a}$$

$$\nabla \times \vec{E} = -\frac{\partial \vec{B}}{\partial t}, \qquad \text{Faraday's Law} \tag{3.1b}$$

$$\nabla \cdot \vec{B} = 0, \qquad \text{Gauss's Law} \tag{3.1c}$$

where $\vec{H}$ is the field intensity, $\vec{E}$ is the electric field, $\vec{J}$ is the current density, $\vec{B}$ is the magnetic flux density. The magnetic flux density in the conductors, which are assumed to be nonmagnetic, is related to the magnetic field density, as shown in Eq.(3.2):

$$\vec{B} = \mu_0 \vec{H}, \tag{3.2}$$

where μ_0 is the permeability of free space. The relationship between the current density and electric field intensity is:

$$\vec{J} = \sigma \vec{E}, \tag{3.3}$$

where σ is the electrical conductivity. Equation Eq.(3.1c) implies that the magnetic flux density can be expressed as the curl of Magnetic Vector Potential (MVP), $\vec{A}$:

$$\nabla \times \vec{A} = \vec{B}. \tag{3.4}$$

Using this identity, Eq.(3.1b) can be rewritten as:

$$\nabla \times \left(\vec{E} + \frac{\partial \vec{A}}{\partial t} \right) = 0. \tag{3.5}$$

Since the curl of the variable in Eq.(3.5) is zero, it can be expressed as the gradient

of the electric scalar potential, Φ:

$$\vec{E} + \frac{\partial \vec{A}}{\partial t} = -\nabla\Phi. \tag{3.6}$$

Using the equations above, a Partial Differential Equation (PDE) representing the electromagnetic dynamics can be written as:

$$\nabla \times \frac{\vec{B}}{\mu_0} = \frac{1}{\mu_0}\nabla \times \nabla \times \vec{A} = \frac{1}{\mu_0}\Big(\nabla(\nabla \cdot \vec{A}) - \nabla^2\vec{A}\Big) = -\sigma\Big(\nabla\Phi + \frac{\partial \vec{A}}{\partial t}\Big). \tag{3.7}$$

Assuming the Coulomb gauge ($\nabla \cdot \vec{A} = 0$), Eq.(3.7) is simplified:

$$\nabla^2\vec{A} = \mu_0\sigma(\nabla\Phi + \frac{\partial \vec{A}}{\partial t}). \tag{3.8}$$

Due to the 1D structure of the problem, the MVP $\vec{A}$ only varies in the $\mathbf{x}$ direction and only has a component in the direction aligned with the current (i.e., $\vec{A} = A(x,t)\mathbf{z}$). Furthermore, only the z-component of the electric scalar potential gradient contributes, denoted as $\nabla\tilde{\Phi}_z$. If a sinusoidal excitation is applied to the winding, $A(x,t)$ can be expressed as follows:

$$A(x,t) = Re[\tilde{A}(x)e^{j\omega t}], \tag{3.9}$$

where ω is the electrical frequency and " ˜ " is used to represent a complex variable. The governing PDE Eq.(3.8) then becomes a complex Ordinary Differential Equation (ODE):

$$\frac{d^2\tilde{A}}{dx^2} = \mu_0\sigma(\nabla\tilde{\Phi}_z + j\omega\tilde{A}), \tag{3.10}$$

The solution of this ODE, expressed in Eq.(3.11), is the summation of the homogeneous solution $\tilde{A}_h$ and particular solution $\tilde{A}_p$:

$$\tilde{A}(x) = \tilde{A}_h + \tilde{A}_p = \tilde{A}_+ e^{\tilde{\gamma}x} + \tilde{A}_- e^{-\tilde{\gamma}x} - \frac{\tilde{\nabla\Phi}_z}{j\omega}, \tag{3.11}$$

where $\tilde{\gamma} = \sqrt{j\omega\mu_0\sigma}$ is the roots of the characteristic equation and $\tilde{A}_+$ and $\tilde{A}_-$ are the coefficients for the homogeneous solution to be determined by boundary conditions.

3.2.2 Boundary Conditions

The slot winding region is divided into N segments, corresponding to the number of conductors in the slot, and w_t and h_t represent the width and height of each conductor, respectively. The k^{th} segment has its own potential gradient $\tilde{\nabla\Phi}_z^{(k)}$, which is assumed to be uniform across the conductor. A net current $I^{(k)}$ flows through each segment in the z direction, as shown in Fig. 3.2 with the boundary conditions.

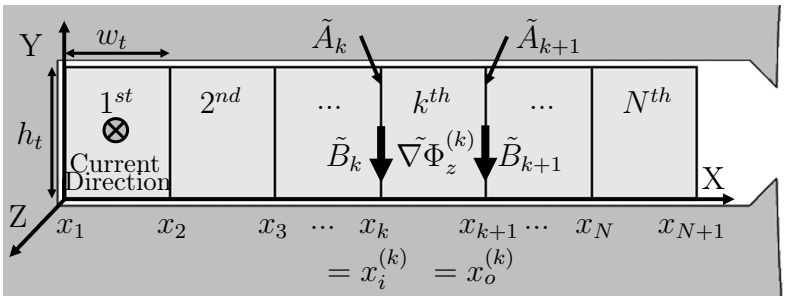

Figure 3.2: Boundary Conditions and Field Variables in Slot

The values of the continuum variables (including position, MVP, flux density and current density.) at the inner boundary $x_i^{(k)}$ and outer boundary $x_o^{(k)}$ of the k^{th} segment are denoted with subscripts k and $k+1$, e.g:

$$x_k = x_i^{(k)}, \tag{3.12}$$

$$x_{k+1} = x_o^{(k)}. \tag{3.13}$$

The superscript (k) denotes the variable as a function of slot depth in the k^{th}

segment, i and o denote the inner and outer boundaries, and subscripts represent the k^{th} and $(k+1)^{th}$ boundary conditions.

For convenience, the MVP boundary condition at the end of the conductor closest to the slot opening is set to be zero, which limits the magnetic analysis to the conductors in the slot interior:

$$\tilde{A}_{N+1} = 0 \tag{3.14}$$

Applying boundary conditions Eq.(3.12) and Eq.(3.13) within the k^{th} segment to Eq.(3.11), the MVP within the k^{th} segment can be calculated.

$$\begin{aligned}\tilde{A}^{(k)}(x) = \frac{1}{sinh(\tilde{\gamma}w_t)} \times \Bigg[& sinh\big(\tilde{\gamma}(x_{k+1}-x)\big)\left(\tilde{A}_k + \frac{\tilde{\nabla\Phi}_z^{(k)}}{j\omega}\right) + \\ & sinh\big(\tilde{\gamma}(x-x_k)\big)\left(\tilde{A}_{k+1} + \frac{\tilde{\nabla\Phi}_z^{(k)}}{j\omega}\right)\Bigg] - \frac{\tilde{\nabla\Phi}_z^{(k)}}{j\omega}\end{aligned} \tag{3.15}$$

The current density within the k^{th} segment can therefore be expressed as:

$$\begin{aligned}\tilde{J}^{(k)}(x) &= -\sigma\left[j\omega\tilde{A}^{(k)} + \tilde{\nabla\Phi}_z^{(k)}\right] \\ &= -\frac{\sigma}{sinh(\tilde{\gamma}w_t)} \times \Bigg[sinh\big(\tilde{\gamma}(x_{k+1}-x)\big)\left(j\omega\tilde{A}_k + \tilde{\nabla\Phi}_z^{(k)}\right) + \\ &\qquad sinh\big(\tilde{\gamma}(x-x_k)\big)\left(j\omega\tilde{A}_{k+1} + \tilde{\nabla\Phi}_z^{(k)}\right)\Bigg]\end{aligned} \tag{3.16}$$

The magnetic flux density in the y direction within the k^{th} segment is therefore given by:

$$\begin{aligned}\tilde{B}_y^{(k)}(x) &= -\frac{d\tilde{A}}{dx} \\ &= \frac{\tilde{\gamma}}{sinh(\tilde{\gamma}w_t)} \times \Bigg[cosh\big(\tilde{\gamma}(x_{k+1}-x)\big)\left(\tilde{A}_k + \frac{\tilde{\nabla\Phi}_z^{(k)}}{j\omega}\right) - \\ &\qquad cosh\big(\tilde{\gamma}(x-x_k)\big)\left(\tilde{A}_{k+1} + \frac{\tilde{\nabla\Phi}_z^{(k)}}{j\omega}\right)\Bigg]\end{aligned} \tag{3.17}$$

The segment boundary conditions for magnetic flux density comes from Ampere's Law Eq.(3.1a):

$$\tilde{B}_k = \mu_0\tilde{H}_k = \frac{\mu_0}{h_t}\sum_{j=1}^{k-1}\tilde{I}^{(j)}, k = 2, ..., \tag{3.18}$$

where $\tilde{I}^{(j)}$ is the current flowing in the j^{th} segment. Since the left-most boundary of the segment of the conductor region is next to the stator iron, which is assumed to be a magnetic short-circuit, we have:

$$\tilde{B}_1 = 0. \tag{3.19}$$

The combination of Eq.(3.17) and Eq.(3.18) contribute to two boundary equations for the k^{th} segment, shown in Eq.(3.20) and Eq.(3.21); the first one corresponding to the inner boundary of segment k^{th}, and the second corresponding to the outer boundary of the same segment k^{th}, as shown in Fig. 3.2:

$$\frac{\tilde{\gamma}h_t}{\mu_0}\left[coth(\tilde{\gamma}w_t)\left(\tilde{A}_k + \frac{\tilde{\nabla\Phi}_z^{(k)}}{j\omega}\right) - csch(\tilde{\gamma}w_t)\left(\tilde{A}_{k+1} + \frac{\tilde{\nabla\Phi}_z^{(k)}}{j\omega}\right)\right] = \sum_{j=1}^{k-1}\tilde{I}^{(j)}, \tag{3.20}$$

$$\frac{\tilde{\gamma}h_t}{\mu_0}\left[csch(\tilde{\gamma}w_t)\left(\tilde{A}_k + \frac{\tilde{\nabla\Phi}_z^{(k)}}{j\omega}\right) - coth(\tilde{\gamma}w_t)\left(\tilde{A}_{k+1} + \frac{\tilde{\nabla\Phi}_z^{(k)}}{j\omega}\right)\right] = \sum_{j=1}^{k}\tilde{I}^{(j)}. \tag{3.21}$$

These equations can be arranged into a matrix form:

$$\frac{\tilde{\gamma}h_t}{j\omega\mu_0}\begin{bmatrix}\mathbf{D} & -\mathbf{U} & \mathbf{0} & ... & \mathbf{0} & \mathbf{0}\\ \mathbf{0} & \mathbf{D} & -\mathbf{U} & ... & \mathbf{0} & \mathbf{0}\\ ... & ... & ... & ... & ... & ...\\ \mathbf{0} & \mathbf{0} & \mathbf{0} & ... & -\mathbf{U} & \mathbf{0}\\ \mathbf{0} & \mathbf{0} & \mathbf{0} & ... & \mathbf{D} & -\mathbf{U}\\ \mathbf{0} & \mathbf{0} & \mathbf{0} & ... & \mathbf{0} & \mathbf{D}\end{bmatrix}\begin{bmatrix}\tilde{\vec{v}}_1\\ \tilde{\vec{v}}_2\\ ...\\ \tilde{\vec{v}}_N\end{bmatrix} = \begin{bmatrix}\tilde{\vec{b}}_1\\ \tilde{\vec{b}}_2\\ ...\\ \tilde{\vec{b}}_N\end{bmatrix}, \tag{3.22}$$

where

$$\mathbf{D} = \begin{bmatrix} coth(\tilde{\gamma}w_t) & coth(\tilde{\gamma}w_t) - csch(\tilde{\gamma}w_t)\\ csch(\tilde{\gamma}w_t) & csch(\tilde{\gamma}w_t) - coth(\tilde{\gamma}w_t)\end{bmatrix}, \tag{3.23}$$

$$\mathbf{U} = \begin{bmatrix} csch(\tilde{\gamma}w_t) & 0\\ coth(\tilde{\gamma}w_t) & 0\end{bmatrix}, \tag{3.24}$$

$$\tilde{\vec{v}}_k = \begin{bmatrix} j\omega(\tilde{A}_k)\\ \tilde{\nabla}\Phi_z^{(k)}\end{bmatrix}, \tag{3.25}$$

$$\tilde{\vec{b}}_k = \begin{bmatrix} \sum_{j=1}^{k-1}\tilde{I}^{(j)}\\ \sum_{j=1}^{k}\tilde{I}^{(j)}\end{bmatrix}. \tag{3.26}$$

3.2.3 Impedance Matrix

In order to calculate effective slot resistance, Eq.(3.22) is used to derive the impedance matrix **Z**. The matrix in Eq.(3.22) is block upper-diagonal, and so the derivation of its inverse is straight-forward. We therefore have:

$$\tilde{\vec{v}}_k = \frac{jw\mu_0}{\tilde{\gamma}h_t}\mathbf{D}^{-1}\sum_{i=k}^{N}(\mathbf{U}\mathbf{D}^{-\mathbf{1}})^{(i-k)}\tilde{\vec{b}}_i, \tag{3.27}$$

where:

$$\mathbf{D}^{-1} = \begin{bmatrix} coth(\tilde{\gamma}w_t) - csch(\tilde{\gamma}w_t) & coth(\tilde{\gamma}w_t) - csch(\tilde{\gamma}w_t) \\ csch(\tilde{\gamma}w_t) & -coth(\tilde{\gamma}w_t) \end{bmatrix} \tag{3.28}$$

It can be shown that $\mathbf{UD}^{-1}$ can be represented in its Jordan form as follows:

$$\begin{aligned} \mathbf{UD}^{-1} &= \frac{1}{1 + cosh(\tilde{\gamma}w_t)} \begin{bmatrix} 1 & 1 \\ cosh(\tilde{\gamma}w_t) & coth(\tilde{\gamma}w_t) \end{bmatrix} \\ &= \mathbf{V\Lambda V^{-1}} \\ &= \begin{bmatrix} 1 & 1 \\ cosh(\tilde{\gamma}w_t) & -1 \end{bmatrix} \begin{bmatrix} 1 & 0 \\ 0 & 0 \end{bmatrix} \begin{bmatrix} 1 & 1 \\ cosh(\tilde{\gamma}w_t) & -1 \end{bmatrix}^{-1} \end{aligned} \tag{3.29}$$

Hence, we have:

$$\begin{aligned} (\mathbf{UD}^{-1})^{(i-k)} &= \mathbf{V\Lambda^{(i-k)}V^{-1}} \\ &= \mathbf{V\Lambda V^{-1}} \\ &= \mathbf{UD}^{-1}, i - k \neq 0 \end{aligned} \tag{3.30}$$

The solution for $\tilde{\vec{v}}_k$ is therefore:

$$\tilde{\vec{v}}_k = \frac{jw\mu_0}{\tilde{\gamma}h_t} \left(\mathbf{D}^{-1} \tilde{\vec{b}}_k + \mathbf{K} \sum_{j=k+1}^{N} \tilde{\vec{b}}_j \right), \tag{3.31}$$

where:

$$\begin{aligned} \mathbf{K} &= \mathbf{D^{-1}UD^{-1}} \\ &= \big(coth(\tilde{\gamma}w_t) - csch(\tilde{\gamma}w_t) \big) \begin{bmatrix} 1 & 1 \\ -1 & -1 \end{bmatrix} \end{aligned} \tag{3.32}$$

Thus Eq.(3.22) can be re-written as:

$$\begin{bmatrix} \tilde{\vec{v}}_1 \\ \tilde{\vec{v}}_2 \\ ... \\ \tilde{\vec{v}}_N \end{bmatrix} = \frac{j\omega\mu_0}{\tilde{\gamma}h_t} \begin{bmatrix} \mathbf{D}^{-1} & \mathbf{K} & \mathbf{K} & ... & \mathbf{K} & \mathbf{K} \\ \mathbf{0} & \mathbf{D}^{-1} & \mathbf{K} & ... & \mathbf{K} & \mathbf{K} \\ ... & ... & ... & ... & ... & ... \\ \mathbf{0} & \mathbf{0} & \mathbf{0} & ... & \mathbf{K} & \mathbf{K} \\ \mathbf{0} & \mathbf{0} & \mathbf{0} & ... & \mathbf{D}^{-1} & \mathbf{K} \\ \mathbf{0} & \mathbf{0} & \mathbf{0} & ... & \mathbf{0} & \mathbf{D}^{-1} \end{bmatrix} \begin{bmatrix} \tilde{\vec{b}}_1 \\ \tilde{\vec{b}}_2 \\ ... \\ \tilde{\vec{b}}_N \end{bmatrix}, \tag{3.33}$$

With Eq.(3.33), $\tilde{A}_k$ and $\tilde{\nabla\Phi}_z^{(k)}$ can then be determined as follows:

$$\tilde{A}_k = \frac{\mu_0}{\tilde{\gamma}h_t}\big(coth(\tilde{\gamma}w_t) - csch(\tilde{\gamma}w_t)\big) \times \sum_{i=k}^{N}\left(2\sum_{j=1}^{i-1}\tilde{I}^{(j)} + \tilde{I}^{(i)}\right), \tag{3.34}$$

$$\begin{aligned} \tilde{\nabla\Phi}_z^{(k)} = \frac{j\omega\mu_0}{\tilde{\gamma}h_t} \times \Bigg[&(csch(\tilde{\gamma}w_t) - coth(\tilde{\gamma}w_t)) \sum_{i=k}^{N}\left(2\sum_{j=1}^{i-1}\tilde{I}^{(j)} + \tilde{I}^{(i)}\right) + \\ &coth(\tilde{\gamma}w_t)\sum_{j=1}^{k-1}\tilde{I}^{(j)} - csch(\tilde{\gamma}w_t)\sum_{j=1}^{k}\tilde{I}^{(j)}\Bigg] \end{aligned} \tag{3.35}$$

The potential gradients of each segment can be re-arranged into a vector and expressed in a corresponding matrix form as follows:

$$\tilde{\vec{\nabla}}\vec{\Phi}_z = \frac{j\omega\mu_0}{\tilde{\gamma}h_t} \times \Big[csch(\tilde{\gamma}w_t)(\mathbf{M_1} - \mathbf{M_3}) - coth(\tilde{\gamma}w_t)(\mathbf{M_1} - \mathbf{M_2})\Big]\tilde{\vec{I}} = \mathbf{Z}\tilde{\vec{I}}, \tag{3.36}$$

where:

$$\vec{\tilde{\nabla}\Phi}_z = \begin{bmatrix} \tilde{\nabla}\Phi_z^{(1)} \\ \tilde{\nabla}\Phi_z^{(2)} \\ ... \\ \tilde{\nabla}\Phi_z^{(N-1)} \\ \tilde{\nabla}\Phi_z^{(N)} \end{bmatrix}; \quad \vec{\tilde{I}} = \begin{bmatrix} \tilde{I}^{(1)} \\ \tilde{I}^{(2)} \\ ... \\ \tilde{I}^{(N-1)} \\ \tilde{I}^{(N)} \end{bmatrix}, \tag{3.37}$$

$$\mathbf{M_1}(i,j) = \begin{cases} 2(N-j)+1, & \text{if } i < j \\ 2(N-i)+2, & \text{if } i \geqslant j \end{cases} \tag{3.38}$$

$$\mathbf{M_2}(i,j) = \begin{cases} 0, & \text{if } i \leqslant j \\ 1, & \text{if } i > j \end{cases} \tag{3.39}$$

$$\mathbf{M_3}(i,j) = \begin{cases} 0, & \text{if } i < j \\ 1, & \text{if } i \geqslant j \end{cases} \tag{3.40}$$

$\mathbf{Z} = \frac{j\omega\mu_0}{\tilde{\gamma}h_t}\big(csch(\tilde{\gamma}w_t)(\mathbf{M_1}-\mathbf{M_3}) - coth(\tilde{\gamma}w_t)(\mathbf{M_1}-\mathbf{M_2})\big)$ is the impedance matrix per unit length.

3.3 Winding Configurations

With the impedance matrix, the proposed model is capable of calculating slot impedance for all possible winding configurations. The effective resistance of the k^{th} conductor in the slot R_k can be calculated as shown in Eq.(3.41):

$$R_k = -Real\left[\frac{\tilde{\nabla}\Phi_z^{(k)} \times l_{stack}}{\tilde{I}^{(k)}}\right], \tag{3.41}$$

where l_{stack} is the stack length.

3.3.1 Full-Pitch Winding

Assuming a full-pitch winding; i.e., all the turns in one slot are from one phase and are connected in series, $\tilde{I}^{(k)} = \tilde{I}$ for all k. Therefore, the AC resistance of the winding in the slot is shown in Eq.(3.42).

$$\begin{aligned} R_{slot} &= \sum_{k=1}^{N} R_k \\ &= -Real\left[\frac{j\omega\mu_0}{\tilde{\gamma}h_t}\left(\frac{2N^3-2N}{3}csch(\tilde{\gamma}w_t) - \frac{2N^3+N}{3}coth(\tilde{\gamma}w_t)\right) \times l_{stack}\right] \end{aligned} \tag{3.42}$$

3.3.2 Fractional Pitch Winding

In a fractional pitch winding, some slots contain coils from multiple phases. Examples are shown in Fig. 3.3 and Fig. 3.4.

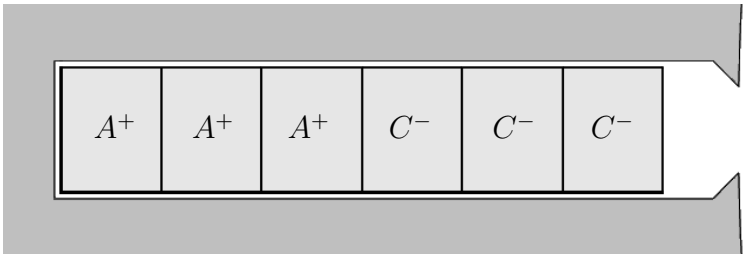

Figure 3.3: Fractional-Pitch Three Phase Winding with Rectangle Conductors in Slots, Case 1

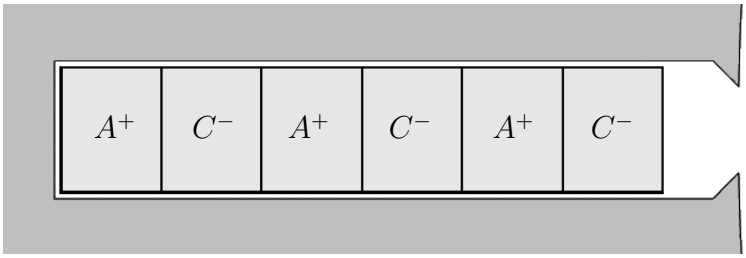

Figure 3.4: Fractional-Pitch Three Phase Winding with Rectangle Conductors in Slots, Case 2

In these cases, $\tilde{I}_{A^+}$ and $\tilde{I}_{C^-}$ are the corresponding phase currents that will be fed into the current vector shown in Eq.(3.37), with the relationship $\tilde{I}_{C^-} = \tilde{I}_{A^+}\underline{/60°}$.

The magnetic field generated in the slot can be determined as the summation of the magnetic field generated by both $\tilde{I}^{(k)} = \tilde{I}_{A^+}$ for $k = 1 \sim 3$ and $\tilde{I}^{(k)} = \tilde{I}_{C^-}$ for $k = 4 \sim 6$. Then, according to Eq.(3.36), the resistance of each phase inside this slot can be calculated.

Similar to Eq.(3.42), the slot resistance associated with a fractional pitch winding for Case 1 and Case 2 can be explicitly expressed in Eq.(3.43) and Eq.(3.44):

$$R_1 = -Real\left[\frac{j\omega\mu_0}{\tilde{\gamma}h_t}\left(\frac{13N^3-16N}{24}csch(\tilde{\gamma}w_t) - \frac{13N^3+8N}{24}coth(\tilde{\gamma}w_t)\right) \times l_{stack}\right] \tag{3.43}$$

$$R_2 = -Real\left[\frac{j\omega\mu_0}{\tilde{\gamma}h_t}\left(\frac{N^3-N}{2}csch(\tilde{\gamma}w_t) - \frac{N^3+N}{2}coth(\tilde{\gamma}w_t)\right) \times l_{stack}\right] \tag{3.44}$$

The resistance of other configurations can be easily generated from the impedance matrix. Moreover, this proposed model can also easily capture the influence of temperature on the AC resistance by simply setting the resistivity as a function of temperature.

3.4 Validation by Finite Element Analysis Simulations

The current density calculated by Eq.(3.16) is compared with the current density distribution determined with FEA of the stator winding with rectangular conductors inside a slot. The structure of this winding is shown in Fig. 3.5 [91].

Figure 3.5: Stator Winding Structure with Rectangle Conductors [91]

The commercial FEA software COMSOL is used to model one pole of the stator, and the simulations are done with the frequency domain solver and run by Intel(R) Xeon(R) CPU E5-2695 V3 @2.3 GHz. The linear model for soft iron material without loss is used for stator iron, with the relative permeability set to be 5000 for iron purity of 99.8%. The input parameters, dimensions of the example stator design, and material properties are provided in Table 3.2.

Table 3.2: Example Dimensions and Setup Parameters.

Geometry parameters	
number of poles N_p	18
N	6
w_t (mm)	2.8
h_t (mm)	2.2
Operation parameters	
RPM	4000
electrical frequency f_e (Hz)	600
$\tilde{I}^{(i)}$ (A)	1
Constants	
σ (m/Ω)	5.24×10^7
μ_0 $(\mathrm{kgm}/(sA)^2)$	$4\pi \times 10^{-7}$
iron permeability μ_r	5000

A vector plot of the slots' magnetic field intensity calculated by 2D FEA is shown in Fig. 3.6. It can be seen that the assumption of only y component field is justified.

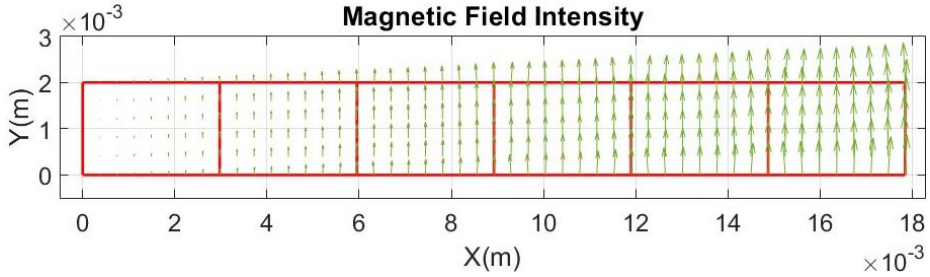

Figure 3.6: Vector Plot of Magnetic Field Intensity in Slot as Calculated by 2D FEA

The 1D plot showing the comparison of the current density distribution at electrical frequency $f_e = 600\ Hz$ by using FEA and the proposed model is shown in Fig. 3.7:

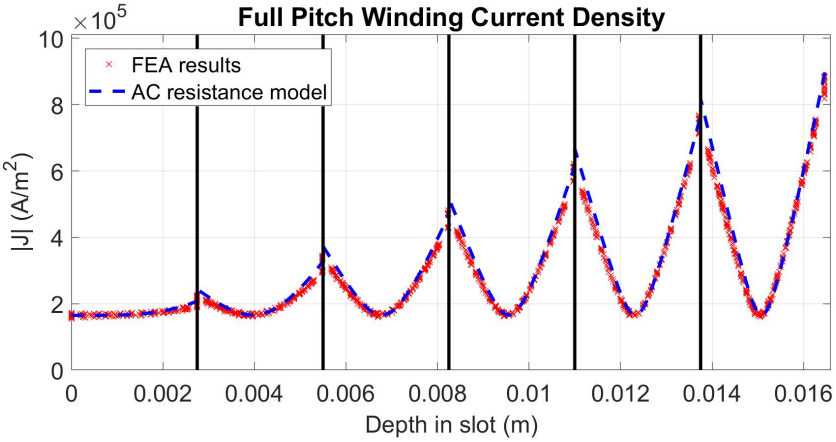

Figure 3.7: Current Density Distribution Comparison at $f_e = 600$-Hz between FEA and the proposed model vs. Depth of Stator Winding Slot in 1D

Similarly, the contour plot showing the comparison is shown in Fig. 3.8:

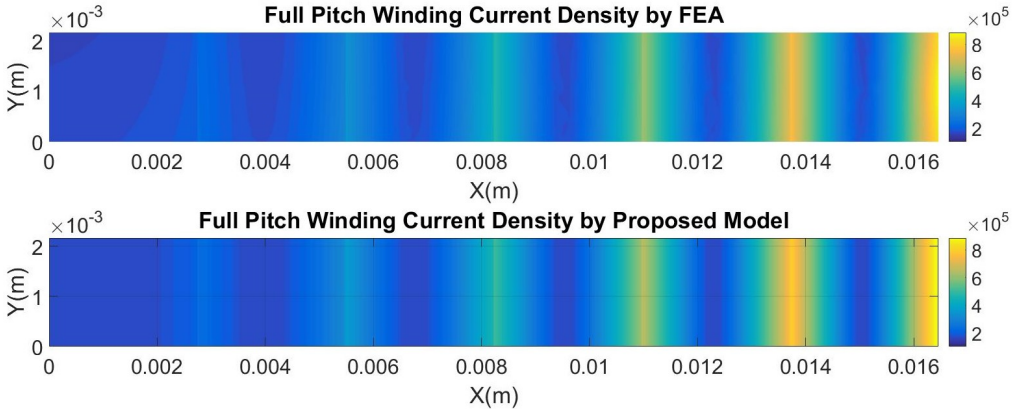

Figure 3.8: Current Distribution Comparison at $f_e = 600\ Hz$ between FEA and the proposed model.

In order to compare the results, we define the average relative difference (ARD) as follows:

$$ARD = \frac{1}{n}\sum_{i=1}^{n}\left|\frac{J_{Proposed,i} - J_{FEA,i}}{J_{FEA,i}}\right| \times 100\%, \tag{3.45}$$

The ARD vs. electric frequencies is shown in Table 3.3.

Table 3.3: ARD Comparison between FEA and the Proposed Model

f_e (Hz)	10	150	300	600
ARD (%)	0.27	1.07	2.40	4.36

It can be seen that the ARD increases with frequency, which may be the result of FEA mesh quality, since the higher the electric frequency is, the thinner the skin depth is; thus, more elements are required to capture the skin and proximity effect accurately.

For the fractional-pitch winding configuration, the current density in one slot containing two phases is also validated by FEA. All setups are the same as the full pitch winding except for $w_t = 4\ mm$ and $h_t = 5\ mm$. Two possible configurations are studied with $N = 6$: Case 1 with the turns of each phase placed adjacently in a group of three, as shown in Fig. 3.3; and Case 2 where the turns of the two phases alternate,

as shown in Fig. 3.4. The current density distributions are shown in Fig. 3.9 and Fig. 3.10, respectively.

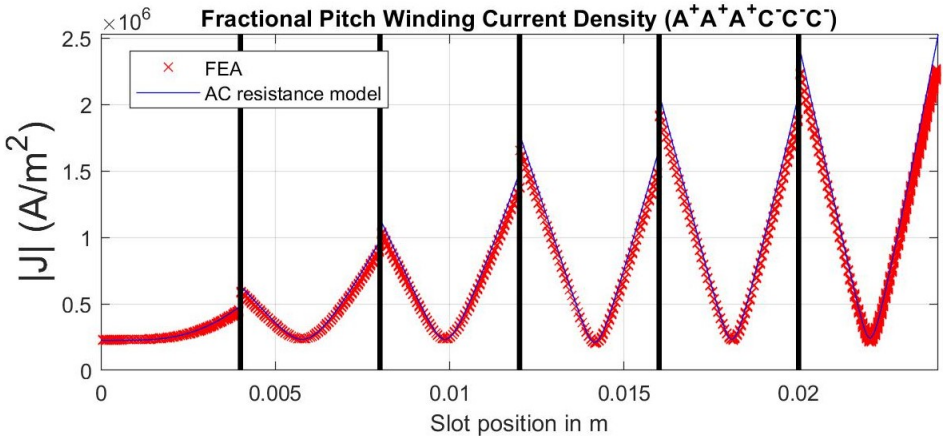

Figure 3.9: Current Distribution Comparison at $f_e = 600\ Hz$ between FEA and the proposed model of fractional pitch winding, Case 1.

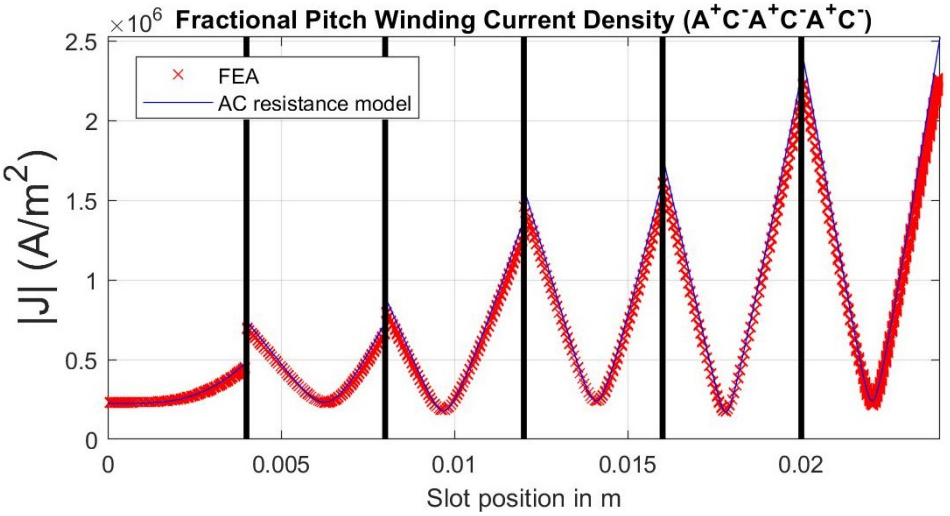

Figure 3.10: Current Distribution Comparison at $f_e = 600\ Hz$ between FEA and the proposed model of fractional pitch winding, Case 2.

The comparison of AC resistance of different configurations is shown in Fig. 3.11. It can be seen that fractional-pitch winding resistance is smaller than the full-pitch winding since the presence of two phases in one slot reduces the magnetic fields compared to the full-pitch winding. The phase resistance for Case 2 of fractional-pitch winding is smaller than Case 1 due to a similar reason: the turns of two phases

alternate such that the magnetic field generated is weaker at each boundary comparing with case 1, according to Ampere's law.

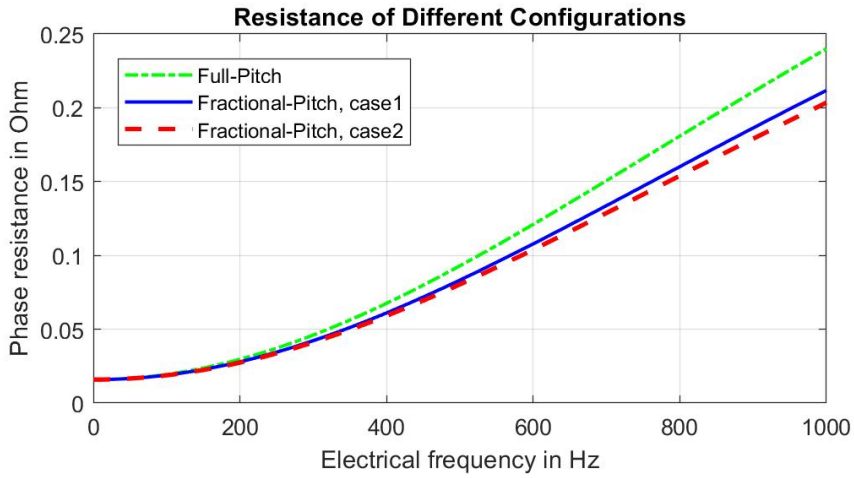

Figure 3.11: Resistance Comparison of Different Winding Configurations

The computation time of the proposed model is dramatically faster than the FEA. For example, the computation time of the Case 1 fractional-pitch winding at $f_e = 600$ Hz for the FEA and the proposed model are as follows:

$$\begin{aligned} T_{FEA} &= 19.9 \quad s \\ T_{ProposedModel} &= 51.1 \quad \mu s \end{aligned} \tag{3.46}$$

3.5 Experimental Validation

A stator with square conductor windings from General Motors, as shown in Fig. 3.12, is used for experimental validation. The line-to-line resistance is measured by an LCR meter for different frequencies, and the phase resistance can be calculated based on its "$\mathbf{Y}$ or Δ" configuration. The stator studied has a $\mathbf{Y}$ configuration, so the phase resistance is the line-to-line resistance.

To estimate the total resistance using the proposed model, the resistance is divided into two parts: the slot resistance and the end-turn resistance. The slot resistance is calculated using Eq.(3.42), while the end-turn resistance is calculated only considering

skin effect, as shown in Eq.(3.47). Then the phase resistance can be calculated based on the number of total slots and parallel connections.

$$R_{endturn} = \frac{L_{endturn}}{\sigma Area}, \tag{3.47}$$

where:

$$Area = \begin{cases} \Delta x \Delta y, & 2\delta \geqslant min(\Delta x, \Delta y) \\ \Delta x \Delta y - (\Delta x - 2\delta)(\Delta y - 2\delta), & \text{otherwise,} \end{cases} \tag{3.48}$$

δ is the skin depth, and $L_{endturn}$ is the winding end turn length.

Figure 3.12: Stator with Rectangle Conductor Winding Provided by General Motors

The geometry information is shown in Table 3.4.

Table 3.4: GM Stator Parameters

N_p	12
Number of parallel paths N_{pp}	1
Number of slots N_{slot}	48
l_{stack} (mm)	51.5
w_t (mm)	3.05
h_t (mm)	3.72

The comparison between the measured phase resistance and estimated resistance calculated using the proposed model is shown in Fig. 3.13.

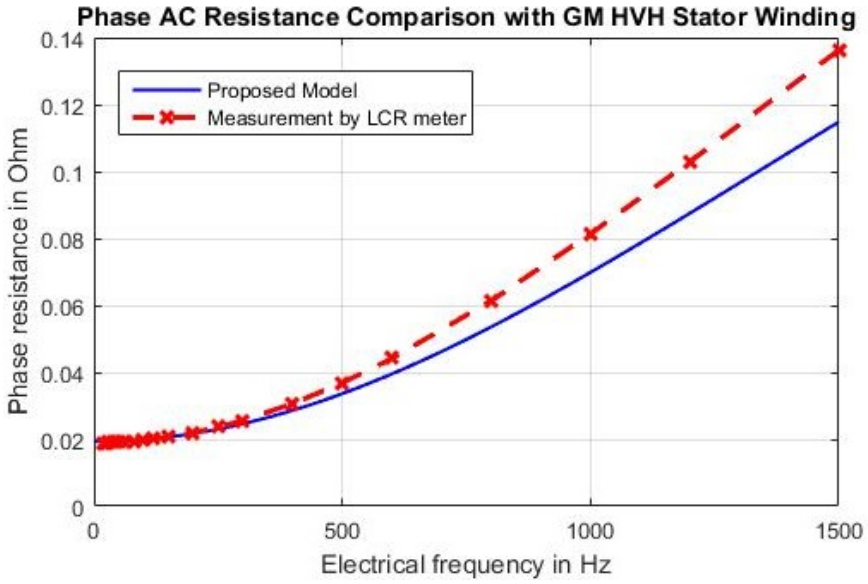

Figure 3.13: Phase AC Resistance Comparison between Experiment and the Proposed Model

Fig. 3.13 shows that, as the electrical frequency increases, the discrepancy increases. One possible explanation is the stator iron loss, which is not considered in the proposed model. Iron loss increases with frequency, which matches with the trend of the discrepancy between the proposed model and measurement. Furthermore, the current density calculated by the proposed model has good agreement with FEA simulations if lossless iron model is applied, while it does not match well if iron loss

model is applied for stator iron material for FEA simulations.

3.6 Conclusion

A computationally efficient method to estimate the AC resistance of rectangular conductor windings in electric machines is presented in this chapter. This method uses a one-dimensional magneto-quasistatic model of the stator slot region to develop boundary transfer relations between each conductor in a slot. These relations are used to create a set of equations that can then be re-arranged to form an impedance matrix, allowing for calculating the resistance of arbitrary winding configurations. FEA simulations were used to validate the current density distribution inside each slot. Experimental measurements of AC resistance at different frequencies were used to validate the resistance calculated by the proposed method.

CHAPTER IV

Comparative Study of Online Loss Estimators Based on Electrical and Thermal Models for AC Permanent Magnet Machines

4.1 Introduction

Power loss estimation in electric machines is important for performance evaluation, condition monitoring, and optimal control. The parameters determining losses can vary with operating conditions; therefore, accurate identification of these parameters is challenging. Online loss estimation can be one solution, where the parameters are identified and updated as they vary under different operating conditions over time. For applications requiring high accuracy, robust estimators considering model uncertainty are needed. A comparative robustness analysis for online loss estimators of AC PM machines using both electrical and thermal models is presented. It is found that estimators based on thermal models are more robust than those based on electrical models over a wide range of operating conditions. The conditions under which the thermal model can achieve better robustness are obtained in analytical expressions and validated through simulation.

The nomenclature used in this chapter is provided in Table 4.1.

Table 4.1: Nomenclature for Loss Estimation

Electrical Model			
G_c	Core Loss Conductance	L_q	Quadrature Inductance
N_p	Number of Poles	L_d	Direct Inductance
I_{pk}	Peak Current	R_w	Winding Resistor
i_d^r	Direct Current	V_{pk}	Peak Voltage
i_{dc}^r	Direct Core Loss Current	v_d^r	Direct Voltage
i_{dm}^r	Direct Magnetization Current	v_q^r	Quadrature Voltage
i_q^r	Quadrature Current	ω_e	Electrical Angular Velocity
i_{qc}^r	Quadrature Core Loss Current	λ_{PM}	Permanent Magnet Flux Linkage
i_{qm}^r	Quadrature Magnetization Current		
Thermal Model			
C_p	Specific Heat	L_{stack}	Stack Length
H_b	Boundary Heat Flux	P_{loss}	Power Loss
h_b	Boundary Heat Convective Coefficient	T	Temperature
k	Material Conductivity		

The superscript "r" represents for variables in the rotor reference frame.

4.2 The Parametric Models for PMSM Loss Estimation

Electrical and thermal models, which are foundations of online loss estimators, are derived in this section.

4.2.1 Assumptions

The models analyzed in this paper are based on the following assumptions:

1. Since the rotor is spinning in synchronization with the rotating magnetic field, rotor loss is small and therefore is ignored;

2. Magnetic saturation is neglected in the electrical model;

3. Conduction loss is modeled by a winding resistance R_w and core loss by a shunt

conductance G_c, as shown in Fig. 4.1. In order to simplify the analysis, the voltage drop due to R_w is neglected when estimating core loss [92]. Thus, the conduction and core losses are expressed as:

$$P_{conds} = \frac{3}{2} R_w I_{pk}^2, \tag{4.1}$$

$$P_{cores} = \frac{3}{2} G_c V_{pk}^2, \tag{4.2}$$

where:

$$I_{pk}^2 = (i_d^r)^2 + (i_q^r)^2, \tag{4.3}$$

$$V_{pk}^2 = (v_d^r)^2 + (v_q^r)^2. \tag{4.4}$$

The estimated parameter vector consists of winding resistance R_w and core conductance G_c are the two parameters used to estimate loss:

$$\vec{\theta} = \begin{bmatrix} R_w & G_c \end{bmatrix}^T. \tag{4.5}$$

4.2.2 Electrical Model

The equivalent circuit for PMSM is shown in Fig. 4.1.

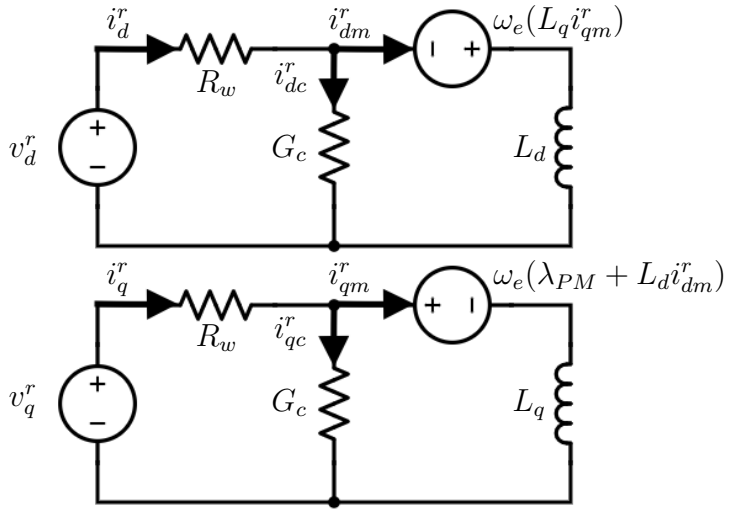

Figure 4.1: Equivalent Circuit for PMSM

The direct and quadrature voltages are expressed as:

$$v_d^r = R_w i_d^r - \omega_e L_q i_{qm}^r + L_d \frac{di_{dm}^r}{dt}, \tag{4.6}$$

$$v_q^r = R_w i_q^r + \omega_e(\lambda_{PM} + L_d i_{dm}^r) + L_q \frac{di_{qm}^r}{dt}. \tag{4.7}$$

And the direct and quadrature core currents are calculated as:

$$i_{dc}^r = G_c(v_d^r - R_w i_d^r) = i_d^r - i_{dm}^r, \tag{4.8}$$

$$i_{qc}^r = G_c(v_q^r - R_w i_q^r) = i_q^r - i_{qm}^r. \tag{4.9}$$

The electrical parametric model can then therefore be expressed as shown in Eqs.(4.10) and (4.11):

$$\begin{aligned} v_d^r = {} & i_d^r R_w + \left(\omega_e L_q v_q^r - L_d \frac{dv_d^r}{dt}\right) G_c \\ & + \left(L_d \frac{di_d^r}{dt} - \omega_e L_q i_q^r\right) + \left(- \omega_e L_q i_q^r + L_d \frac{di_d^r}{dt}\right) R_w G_c, \end{aligned} \tag{4.10}$$

and

$$\begin{aligned} v_q^r = {} & i_q^r R_w - \left(\omega_e L_d v_d^r + L_q \frac{dv_q^r}{dt}\right) G_c \\ & + \left(L_q \frac{di_q^r}{dt} + \omega_e L_d i_d^r + \omega_e \lambda_{PM}\right) + \left(\omega_e L_d i_d^r + L_q \frac{di_q^r}{dt}\right) R_w G_c, \end{aligned} \tag{4.11}$$

where the product $R_w G_c$ is relatively small and can be assumed equal to zero with acceptable accuracy. The parametric electrical model for loss estimation is therefore:

$$\begin{aligned} \begin{bmatrix} v_d^r \\ v_q^r \end{bmatrix} - \begin{bmatrix} L_d \frac{di_d^r}{dt} - \omega_e L_q i_q^r \\ L_q \frac{di_q^r}{dt} + \omega_e L_d i_d^r + \omega_e \lambda_{PM} \end{bmatrix} &= \begin{bmatrix} i_d^r & \omega_e L_q v_q^r - L_d \frac{dv_d^r}{dt} \\ i_q^r & -\omega_e L_d v_d^r - L_q \frac{dv_q^r}{dt} \end{bmatrix} \begin{bmatrix} R_w \\ G_c \end{bmatrix} \\ &= \vec{m}_e - \Delta \vec{z}_e = \vec{z}_e = \phi_e^T \vec{\theta}, \end{aligned} \tag{4.12}$$

where $\vec{m}_e$ is the measured (estimated) voltage. This is what we can observe for loss

estimation based on the electrical model. The difference between $\vec{m}_e$ and $\Delta\vec{z}_e$ (the voltage change due to back Electromotive Force (EMF)) is what we refer to as the output signal $\vec{z}_e$ of the linear parametric model for estimation, and ϕ_e^T is the regressor. Subscript "e" stands for the electrical model.

Therefore, the steady-state voltages are:

$$\begin{aligned}\begin{bmatrix} v_d^r \\ v_q^r \end{bmatrix} - \begin{bmatrix} -\omega_e L_q i_q^r \\ \omega_e L_d i_d^r + \omega_e \lambda_{PM} \end{bmatrix} &= \begin{bmatrix} i_d^r & \omega_e L_q v_q^r \\ i_q^r & -\omega_e L_d v_d^r \end{bmatrix} \begin{bmatrix} R_w \\ G_c \end{bmatrix} \\ &= \vec{m}_{e,s} - \Delta\vec{z}_{e,s} = \vec{z}_{e,s} = \phi_{e,s}^T \vec{\theta},\end{aligned} \tag{4.13}$$

where the subscript "s" stands for steady-state operation.

The voltages provided by power electronics inverters are used to drive the machines. However, the voltages are not usually measured directly; instead, they are often estimated from the inverter duty cycles and voltage drops in transistors. It is worth noting that transistor voltage drop can significantly affect winding resistance estimation. Since voltage estimation is out of this dissertation's scope, we assume good knowledge of the voltage information.

To avoid numerous issues with the derivative terms in Eq.(4.12) for the electrical model, a first-order low-pass filter is applied. This filter is stable, minimum phase, and strictly proper. The filtered signal and its derivative are:

$$\tilde{x} = \{M(s)\}x, \qquad \frac{d}{dt}\tilde{x} = \{sM(s)\}x, \tag{4.14}$$

where x denotes i_d^r, i_q^r, v_d^r or v_q^r, $M(s) = \frac{f_0}{s+f_0}$, f_0 is the cut-off frequency, and $\{\cdot\}x$ refers to the fact that the filter with the transfer function of "$\cdot$" is applied to the signal x.

4.2.3 Thermal Model

The thermal model is introduced in this section. The governing PDE of thermal conduction is shown in Eq.(2.1) in Chapter 2:

$$C_p \frac{\partial T}{\partial t} - k\nabla^2 T = q_{loss}. \tag{4.15}$$

The thermal model is generated by applying this equation to the PMSM stator with appropriate convective boundary conditions. However, due to the complexity of the geometry and variety of materials, as shown in Fig. 1.3, this equation can not be solved analytically for an electric machine.

Thermal systems are typically modeled using two main methods. A common approach is the LPTM presented in [17], which makes use of an equivalent circuit network. Another method with higher accuracy uses FEA introduced in Chapter 1. The latter approach discretizes Eq.(2.1) spatially and temporarily and solves it numerically.

Both methods can be generalized by applying different levels of discretization and model order reduction. LPTM only has a relatively small number of temperatures for each component, while the numerical model has a large number of temperatures within each component. By spatially discretizing Eq.(2.1), we have a generalized thermal model which can represent both LPTM and FEA models, as shown in Eq.(4.16).

$$\mathbf{C}\dot{\vec{T}} + \mathbf{K}\vec{T} = \sum_i \vec{f}_{loss,i} P_{loss,i} - \sum_j \vec{f}_{b,j} H_{b,j}, \tag{4.16}$$

where $\mathbf{C} \in R^{n\times n}$ and $\mathbf{K} \in R^{n\times n}$ (n is the length of temperature vector) are matrices generated due to spatial discretization, which are determined by material properties, machine geometry, and discretization method. Matrix $\mathbf{C}$ captures specific heat and matrix $\mathbf{K}$ captures thermal conductivity. Their non-zero entries indicate how the discretized elements/components are connected. Parameter $P_{loss,i}$ stands for the total

power loss for the i^{th} loss mechanism, $H_{b,j}$ stands for the heat flux density for the j^{th}. The vector $\vec{f}_{loss,i}$ is the normalized loss distribution vector for the i^{th} loss mechanism and $\vec{f}_{b,j}$ is the normalized flux distribution for the j^{th} convective boundary.

The power loss of the stator P_{loss} consists of conduction loss and core loss. Referring to Eq.(4.1) and Eq.(4.2), the parametric thermal model for loss estimation is:

$$\mathbf{C}\dot{\vec{T}} + \mathbf{K}\vec{T} + \sum_j \vec{f}_{b,j} H_{b,j} = \begin{bmatrix} \frac{3}{2} I_{pk}^2 \vec{f}_{conds} & \frac{3}{2} V_{pk}^2 \vec{f}_{cores} \end{bmatrix} \begin{bmatrix} R_w \\ G_c \end{bmatrix}. \tag{4.17}$$

Assuming constant loss and boundary conditions, the linear model with the selected two temperature measurements for loss estimation is:

$$\begin{aligned} &\vec{T}_m(s) + \mathbf{M_T}(\mathbf{C}s + \mathbf{K})^{-1} \frac{\sum_j \vec{f}_{b,j} H_{b,j}}{s} \\ &\qquad = \mathbf{M_T}(\mathbf{C}s + \mathbf{K})^{-1} \begin{bmatrix} \frac{3}{2s} I_{pk}^2 \vec{f}_{conds} & \frac{3}{2s} V_{pk}^2 \vec{f}_{cores} \end{bmatrix} \begin{bmatrix} R_w \\ G_c \end{bmatrix} \\ &\quad = \vec{m}_t - \Delta\vec{z}_t = \vec{z}_t = \phi_t^T \vec{\theta}, \end{aligned} \tag{4.18}$$

where $\vec{m}_t$ is the measured temperature vector, $\Delta\vec{z}_t$ is the temperature change due to boundary convection, $\vec{z}_t$ is the output signal and ϕ_t^T is the regressor. Subscript "t" stands for the thermal model. The matrix $\mathbf{M_T} \in R^{2\times n}$ is the selection matrix, with "1" entries on each row with index corresponding to nodal positions for the temperatures measurements (i.e., winding and back iron) shown in Fig.1.3, and zero entries otherwise.

The steady-state temperatures are therefore:

$$\begin{aligned} &\vec{T}_m + \mathbf{M_T}\mathbf{K}^{-1} \sum_j \vec{f}_{b,j} H_{b,j} = \mathbf{M_T}\mathbf{K}^{-1} \Big(\begin{bmatrix} \frac{3}{2} I_{pk}^2 \vec{f}_{conds} & \frac{3}{2} V_{pk}^2 \vec{f}_{cores} \end{bmatrix} \begin{bmatrix} R_w \\ G_c \end{bmatrix} \Big) \\ &\qquad = \vec{m}_{t,s} - \Delta\vec{z}_{t,s} = \vec{z}_{t,s} = \phi_{t,s}^T \vec{\theta}, \end{aligned} \tag{4.19}$$

We will use $\mathbf{F}$ to denote $\begin{bmatrix} \vec{f}_{conds} & \vec{f}_{cores} \end{bmatrix}$.

4.3 Loss Estimation Algorithm

The adaptive parameter estimation method used in this section is now introduced.

The normalized gradient descent approach is used to build the estimators for the following linear model [93]:

$$\vec{z} = \phi^T \vec{\theta}^*, \tag{4.20}$$

where $\vec{\theta}^*$ is the true values of the estimated parameter vector, ϕ is the regressor and $\vec{z}$ is the observation signal.

Let $\vec{\theta}$ be the estimate of the unknown parameter vector $\vec{\theta}^*$. To compute $\vec{\theta}$, we construct the following normalized quadratic cost function:

$$J(\vec{\theta}) = \frac{(\epsilon)^2}{2m^2} = \frac{(\vec{\theta} - \vec{\theta}^*)^T \phi \phi^T (\vec{\theta} - \vec{\theta}^*)}{2m^2}, \tag{4.21}$$

where $\epsilon = \phi^T \vec{\theta} - \vec{z} = \phi^T (\vec{\theta} - \vec{\theta}^*)$, is the observation error, and $m = \sqrt{1 + \phi^T \phi}$ is the normalizing signal.

Using the steepest descent method and noting that $\frac{\partial J}{\partial \vec{\theta}} = \frac{\phi \epsilon}{m^2}$, the following adaptive law can be used for estimation of $\vec{\theta}$ [93]:

$$\dot{\vec{\theta}}(t) = -\frac{\Gamma \phi(t) \epsilon(t)}{m^2(t)}, \tag{4.22}$$

where Γ is the gain matrix.

As long as the persistency of excitation condition is satisfied, this adaptive law will adjust the estimated parameters until the observation error ϵ converges to zero, and the estimated parameters converge.

The persistent excitation condition is satisfied if and only if the 2×2 Grammian matrix $W(t, t + \Delta T)$ is Positive Definite (PD) for all $t \geqslant 0$ and some ΔT, as shown in [74]:

$$W(t, t+\Delta T) = \frac{1}{\Delta T} \int_{t}^{t+\Delta T} \phi(\tau)\phi^T(\tau)d\tau. \tag{4.23}$$

The worst-case scenario for persistency of excitation is steady-state operation, thus two independent outputs are needed ($\vec{z} \in R^{2\times 1}$, $\phi^T \in R^{2\times 2}$) to satisfy PD requirement of $W(t, t+\Delta T)$.

Considering the facts:

1. If the square matrix ϕ is full rank, then $\phi\phi^T$ is PD;
2. If ϕ is not full rank, then $\phi\phi^T$ is Positive Simi-Definite (PSD);
3. The summation of PD matrices is PD;
4. The summation of PD matrices and PSD matrices is PD.

So for constant excitation, it is sufficient to guarantee that the system is persistently excited if the square regressor matrix ϕ is full rank.

4.4 Robustness of the Estimators

The estimators' robustness is defined as its performance when uncertainty is introduced into other parameters that are not the estimation targets. The uncertain parameters for these two models are listed in Table 4.2, with level of uncertainty:

Table 4.2: Uncertain Parameters for Electrical/Thermal Models

	Parameter p	Uncertainty Level
Electrical Model	L_d	$\sim 0.5\%$ [94]
	L_q	$\sim 1.5\%$ [94]
	λ_{PM}	$\sim 4\%$ [95]
Thermal Model	$C_{p,j}$	$\sim 0.2\%$ [96]
	k_j	$\sim 3\%$ [97]
	$H_{b,j}$	$\sim 5\%$ [98]

The robustness is quantified by the estimated parameters' sensitivity w.r.t the

uncertain parameters. To compare the effects of different parameters, the relative variation in the estimated parameter w.r.t the relative variation in the uncertain parameter [99] is determined:

$$S_{\theta_i,p} = \frac{\partial \theta_i}{\partial p}\frac{p}{\theta_i}, \tag{4.24}$$

where p represents the uncertain parameter.

In general, sensitivity depends on the type of excitation and it is time-dependent. For simplicity, we focus on steady-state errors caused by the uncertain parameter (which is also the worst-case scenario) and calculate the steady-state sensitivity.

Uncertainty in the parameters will introduce errors in $\boldsymbol{\phi}_s^T$ and $\Delta\vec{\boldsymbol{z}}_s$. Note that:

$$\phi_s{}^T\vec{\theta} + \Delta\vec{z}_s = \vec{m}_s, \tag{4.25}$$

and $\vec{m}_s$ is independent of p, so we have:

$$\frac{\partial \phi_s^T}{\partial p}\vec{\theta} + \phi_s^T\frac{\partial \vec{\theta}}{\partial p} + \frac{\partial \Delta\vec{z}_s}{\partial p} = 0. \tag{4.26}$$

Thus, $\frac{\partial\vec{\theta}}{\partial p}$ can be calculated as:

$$\frac{\partial \vec{\theta}}{\partial p} = -\left(\phi_s^T\right)^{-1}\left(\frac{\partial \phi_s^T}{\partial p}\vec{\theta} + \frac{\partial \Delta\vec{z}_s}{\partial p}\right). \tag{4.27}$$

The sensitivity is therefore:

$$\begin{bmatrix} S_{R_w,p} \\ S_{G_c,p} \end{bmatrix} = -\begin{bmatrix} \frac{p}{R_w} & 0 \\ 0 & \frac{p}{G_c} \end{bmatrix}\left(\phi_s^T\right)^{-1}\left(\frac{\partial \phi_s^T}{\partial p}\vec{\theta} + \frac{\partial \Delta\vec{z}_s}{\partial p}\right). \tag{4.28}$$

4.4.1 Sensitivity Analysis of the Electrical Model

Commanding constant i_q^r and i_d^r, and referring to Eq.(4.13) and Eq.(4.28), we have:

$$\phi_s^T = \begin{bmatrix} i_d^r & \omega_e L_q v_q^r \\ i_q^r & -\omega_e L_d v_d^r \end{bmatrix}, \tag{4.29}$$

and

$$\Delta \vec{z}_s = \begin{bmatrix} -\omega_e L_q i_q^r \\ \omega_e L_d i_d^r + \omega_e \lambda_{PM} \end{bmatrix}. \tag{4.30}$$

Sensitivities for the estimated parameters w.r.t L_d, L_q, and λ_{PM} can then be expressed as:

$$\begin{bmatrix} S_{R_w,L_d} \\ S_{G_c,L_d} \end{bmatrix} = \frac{\omega_e}{i_d^r \omega_e L_d v_d^r + i_q^r \omega_e L_q v_q^r} \begin{bmatrix} \frac{L_d}{R_w} & 0 \\ 0 & \frac{L_d}{G_c} \end{bmatrix} \begin{bmatrix} \omega_e L_d v_d^r & \omega_e L_q v_q^r \\ i_q^r & -i_d^r \end{bmatrix} \begin{bmatrix} 0 \\ v_d^r G_c - i_d^r \end{bmatrix}, \tag{4.31}$$

$$\begin{bmatrix} S_{R_w,L_q} \\ S_{G_c,L_q} \end{bmatrix} = -\frac{\omega_e}{i_d^r \omega_e L_d v_d^r + i_q^r \omega_e L_q v_q^r} \begin{bmatrix} \frac{L_q}{R_w} & 0 \\ 0 & \frac{L_q}{G_c} \end{bmatrix} \begin{bmatrix} \omega_e L_d v_d^r & \omega_e L_q v_q^r \\ i_q^r & -i_d^r \end{bmatrix} \begin{bmatrix} v_q^r G_c - i_q^r \\ 0 \end{bmatrix}, \tag{4.32}$$

and

$$\begin{bmatrix} S_{R_w,\lambda_{PM}} \\ S_{G_c,\lambda_{PM}} \end{bmatrix} = -\frac{\omega_e}{i_d^r \omega_e L_d v_d^r + i_q^r \omega_e L_q v_q^r} \begin{bmatrix} \frac{\lambda_{PM}}{R_w} & 0 \\ 0 & \frac{\lambda_{PM}}{G_c} \end{bmatrix} \begin{bmatrix} \omega_e L_d v_d^r & \omega_e L_q v_q^r \\ i_q^r & -i_d^r \end{bmatrix} \begin{bmatrix} 0 \\ 1 \end{bmatrix}. \tag{4.33}$$

Eqs.(4.31), (4.32) and (4.33) show that sensitivities of electrical models depend greatly on the operating conditions of currents and rotor speed. Based on the machine

specifications and operating range, the estimator sensitivity based on the electrical model can be calculated accordingly.

4.4.2 Sensitivity Analysis of Thermal Model

Referring to Eq.(4.19) and Eq.(4.28), we have:

$$\boldsymbol{\phi}_s^T = \mathbf{M_T}\mathbf{K}^{-1}\mathbf{F}\begin{bmatrix} \frac{3}{2}I_{pk}^2 & 0 \\ 0 & \frac{3}{2}V_{pk}^2 \end{bmatrix}, \tag{4.34}$$

and

$$\Delta\vec{z}_s = -\mathbf{M_T}\mathbf{K}^{-1}\sum_j \vec{f}_{b,j}H_{b,j}. \tag{4.35}$$

If uncertainty is in C_p, $\mathbf{C}$ will change while $\mathbf{K}$ will remain the same, thus, referring to Eq.(4.19), the estimated parameters in steady state will not be influenced. However, if uncertainty is in material conductivity k, $\mathbf{K}$ will change accordingly. $\mathbf{K}$ can be expressed as the linear combination of $\mathbf{K_i}$, which also satisfies $\mathbf{K_i} \propto k_i$, where k_i is the thermal conductivity of i^{th} material:

$$\mathbf{K} = \sum_i \mathbf{K}_i = \sum_i \mathbf{M}_i k_i. \tag{4.36}$$

The sensitivity of estimated parameters with respect to conductivity k_i is:

$$\begin{aligned}\begin{bmatrix} S_{R_w,k_i} \\ S_{G_c,k_i} \end{bmatrix} &= \begin{bmatrix} R_w & 0 \\ 0 & G_c \end{bmatrix}^{-1} \frac{\partial\vec{\theta}}{\partial k_i}k_i \\ &= -\begin{bmatrix} P_{conds} & 0 \\ 0 & P_{cores} \end{bmatrix}^{-1} \left(\mathbf{M_T}\mathbf{K}^{-1}\mathbf{F}\right)^{-1}\left(\mathbf{M_T}\mathbf{K}^{-1}\left(\mathbf{K}_i\mathbf{K}^{-1}\right)\mathbf{F}\right)\begin{bmatrix} P_{conds} \\ P_{cores} \end{bmatrix} \\ &\quad + \sum_j \begin{bmatrix} \frac{H_{b,j}}{P_{conds}} & 0 \\ 0 & \frac{H_{b,j}}{P_{cores}} \end{bmatrix}\left(\mathbf{M_T}\mathbf{K}^{-1}\mathbf{F}\right)^{-1}\mathbf{M_T}\mathbf{K}^{-1}\left(\mathbf{K}_i\mathbf{K}^{-1}\right)\vec{f}_{b,j}.\end{aligned} \tag{4.37}$$

On the other hand, if uncertainty is introduced in the j^{th} convective boundary

condition, the sensitivity with respect to $H_{b,j}$ is:

$$\begin{bmatrix} S_{R_w,H_{b,j}} \\ S_{G_c,H_{b,j}} \end{bmatrix} = \begin{bmatrix} P_{conds} & 0 \\ 0 & P_{cores} \end{bmatrix}^{-1} \frac{\partial \vec{p}}{\partial H_{b,j}} H_{b,j} = \begin{bmatrix} \frac{H_{b,j}}{P_{conds}} & 0 \\ 0 & \frac{H_{b,j}}{P_{cores}} \end{bmatrix} \left(\mathbf{M_T K^{-1} F}\right)^{-1} \mathbf{M_T K^{-1}} \vec{f}_{b,j}. \tag{4.38}$$

4.5 Simulation Validation

4.5.1 Estimators Based on Electrical and Thermal Models

The estimators' schematic diagrams based on electrical and thermal models for online loss estimation are shown in Figs. 4.2 and 4.3, respectively.

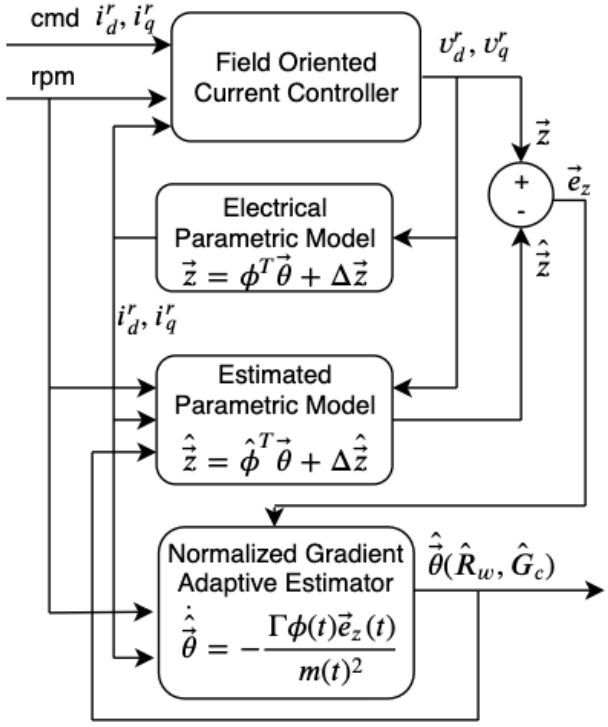

Figure 4.2: Schematic Diagram for Online Loss Estimator Based on Electrical Model Using Normalized Gradient Algorithm

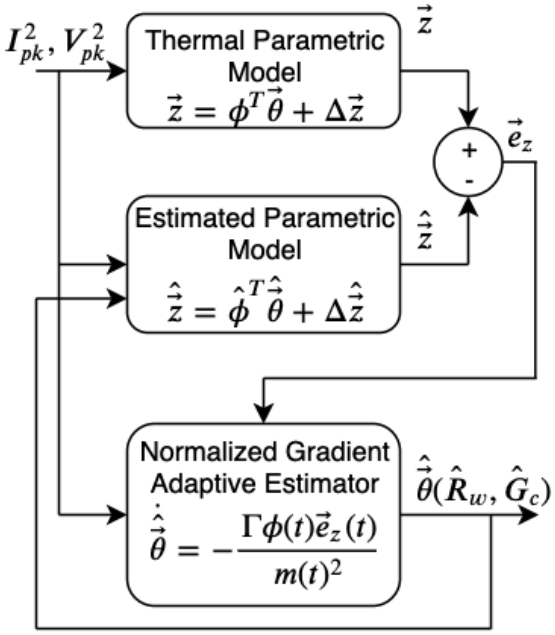

Figure 4.3: Schematic Diagram for Online Loss Estimator Based on Thermal Model Using Normalized Gradient Algorithm

The simulation model is conducted based on the UQM145 PowerPhase SMPMs [14]. The direct current i_d^r is set to be $0A$ to minimize winding loss as i_d^r does not produce torque for SMPMs. The specifications, operating conditions (machine speed and current), and boundary conditions are shown in Table 4.3.

Table 4.3: Machine Specifications and Operating Conditions.

Machine Specification	
N_p	18
Number of Teeth	108
Endturn-Effect Coeff	0.2759
L_{stack} (m)	0.142
L_d (H)	1.05×10^{-4}
L_q (H)	1.8×10^{-4}
λ_{PM} $(V \cdot sec)$	6×10^{-2}
Operation parameters	
RPM	4000
i_d^r (A)	0
i_q^r (A)	214.8
V_{pk}^2 (V^2)	7.4×10^4
P_{conds} (kW)	1.102
P_{cores} (kW)	1.14
Thermal parameters	
H_{end} (w)	2.6073
H_{liq} (w)	558.0788
H_{ags} (w)	32.8664
Uncertainty	
Uncertainty Level	1%/10%

4.5.2 Persistence of Excitation

Before the simulation, the requirement of the persistence of excitation is verified for both models. Since for both models, $\phi^T \in R^{2\times 2}$, as long as ϕ^T is full rank, the requirement of the persistence of excitation can be met.

For the electrical model, without considering the reference filter since it will not affect the results[1], the regressor is:

$$\phi_e^T = \begin{bmatrix} 0 & \omega_e L_q v_q^r - L_d \frac{dv_d^r}{dt} \\ i_q^r & -\omega_e L_d v_d^r - L_q \frac{dv_q^r}{dt} \end{bmatrix}. \tag{4.39}$$

[1]Given a persistently exciting u with u' bounded, and a stable, minimum phase, proper transfer function $M(s)$, it follows that $y = \{M(s)\}u$ is also persistently exciting [100].

For the thermal model, the regressor is:

$$\phi_t^T = \mathbf{M_T}(\mathbf{C}s + \mathbf{K})^{-1} \begin{bmatrix} \frac{3}{2} I_{pk}^2 \vec{f}_{conds} & \frac{3}{2} V_{pk}^2 \vec{f}_{cores} \end{bmatrix}. \tag{4.40}$$

Both regressors have non-zero determinant except for $t = 0s$ and $2.5s$, shown in Fig. 4.4 with operating conditions provided in Table 4.3, so the requirement of the persistence of excitation in Section 4.3 is met.

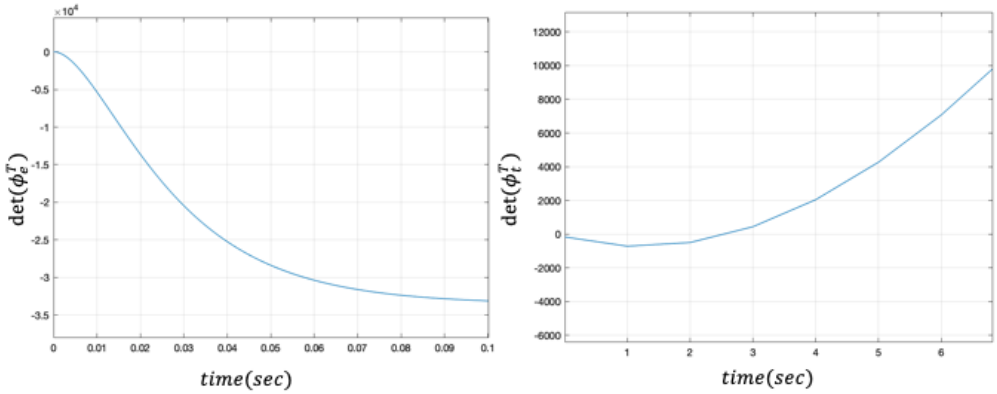

Figure 4.4: The determinant of regressor for the electrical and thermal model

4.5.3 Simulation Results

The thermal model used for validation is expressed in [15]. The thermal conductivity in materials of winding, iron and liner (with subscripts *winding*, *iron* and *liner*, respectively) is considered. The convective boundaries include the air gap, the end region, and the liquid cooling (with subscripts *ags*, *end* and *liq*, respectively) as shown in Figs.1.3 and 1.4.

Estimator performance for nominal conditions (assuming no uncertainty in the parametric model) is evaluated first. Then uncertainty in one unestimated parameter will be simulated. The sensitivity of the estimated parameters w.r.t this uncertain parameter will be numerically calculated after each simulation. This numerical sensitivity will then be compared with the theoretical sensitivity analysis provided in Section 4.4.

4.5.3.1 Performance of Estimator Based on Electrical Model

Fig. 4.5 shows the estimator performance at nominal condition for the electrical model, assuming no uncertainty in the parameters of L_d, L_q and λ_{PM}. The estimated parameters have steady-state errors due to the neglect of the term $R_w G_c$ (Relative Errors of 0.25% for R_w and 1.46% for G_c).

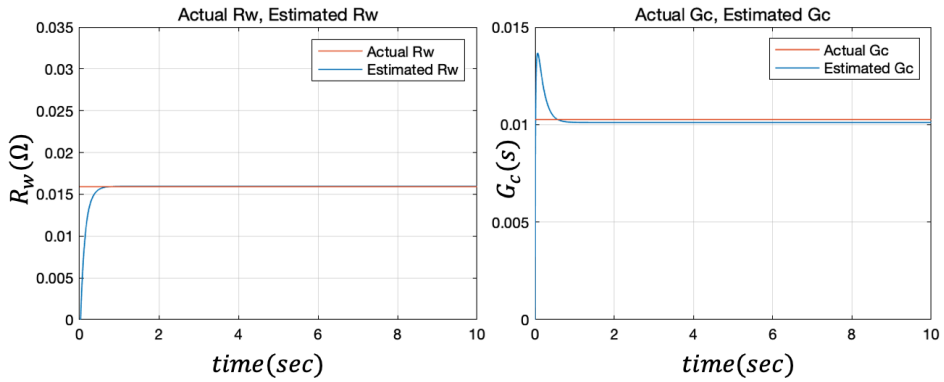

Figure 4.5: Estimator performance at Nominal Condition for the Electrical Model (No Uncertainty in Unestimated Parameters)

Fig. 4.6 shows how the estimated parameters R_w and G_c converge given 1% uncertainty in the electrical parameters.

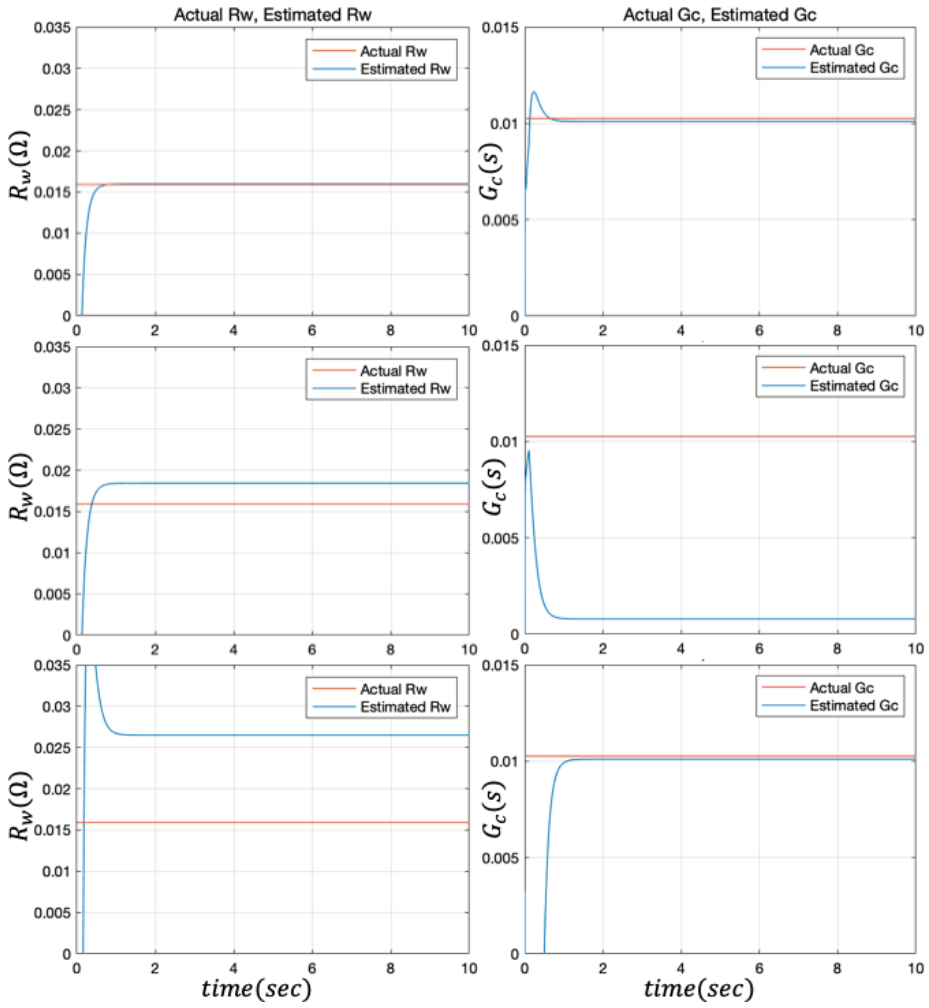

Figure 4.6: Convergence of Estimated Parameters Using Electrical Parameters. Top: 1% decrease in L_d. Middle: 1% decrease in L_q. Bottom: 1% decrease in λ_{PM}.

It can be seen that, when 1% uncertainty is introduced in L_d, the converged values of estimated parameters are still close to true values. However, situations change when L_q is not well-known. Both estimated parameters differ significantly from their truth, especially for G_c. Besides, uncertainty in λ_{PM} influences the estimated R_w dramatically, while G_c does not deviate significantly from its ground truth. The numerical and theoretical sensitivities for the electrical model for uncertainty in 1% are summarized in Table 4.4.

Note that the electrical model used to design the loss estimator does not include

the non-linear term $R_w G_c$ (and hence the sensitivity analysis), while the simulation model does. Therefore, the numerical sensitivity will be different from those calculated from the theoretical analysis, which is especially obvious for small sensitivity shown in the 6^{th} row of Table. 4.4.

Table 4.4: Estimated Parameter Sensitivity (Electrical Model)

Uncertainty Estimation	Sensitivity	
	Analysis	Simulation
$R_w, 99\%L_d$	0.48	0.44
$G_c, 99\%L_d$	0	0
$R_w, 99\%L_q$	15.56	15.83
$G_c, 99\%L_q$	96.24	92.34
$R_w, 99\%\lambda_{PM}$	66.45	65.77
$G_c, 99\%\lambda_{PM}$	0	1.46

4.5.3.2 Performance of Estimator Based on Thermal Model

Fig. 4.7 shows the estimator performance at nominal condition for the thermal model, assuming no uncertainty in the parameters of k_i and $H_{b,j}$. Both estimated parameter converge to their ground truth.

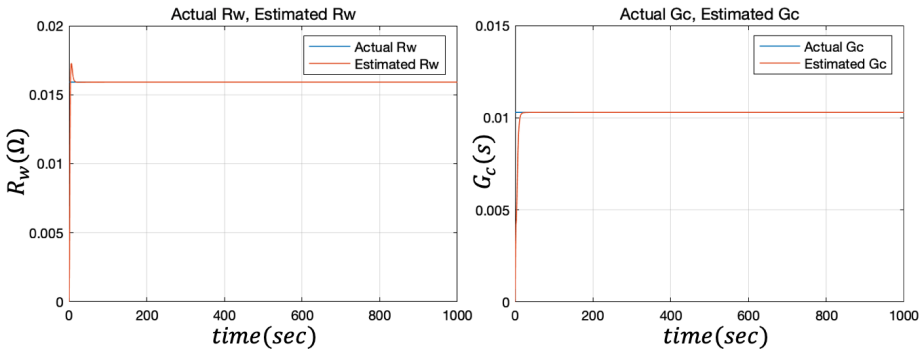

Figure 4.7: Estimator performance at Nominal Condition for the Thermal Model (No Uncertainty in Unestimated Parameters)

Figs. 4.8 and 4.9 show how the estimated parameters R_w and G_c converge given 1% uncertainty in the thermal parameters. It can be seen that the estimated parameters converge to the values close to their ground truth values given 1% uncertainty in k_i,

including $k_{winding}, k_{iron}$ and k_{liner} in Fig. 4.8, and in $H_{b,j}$, including H_{end}, H_{liq}, and H_{ags} in Fig. 4.9. The estimator robustness is significantly improved when the loss parameters are estimated based on the thermal model instead of the electrical model.

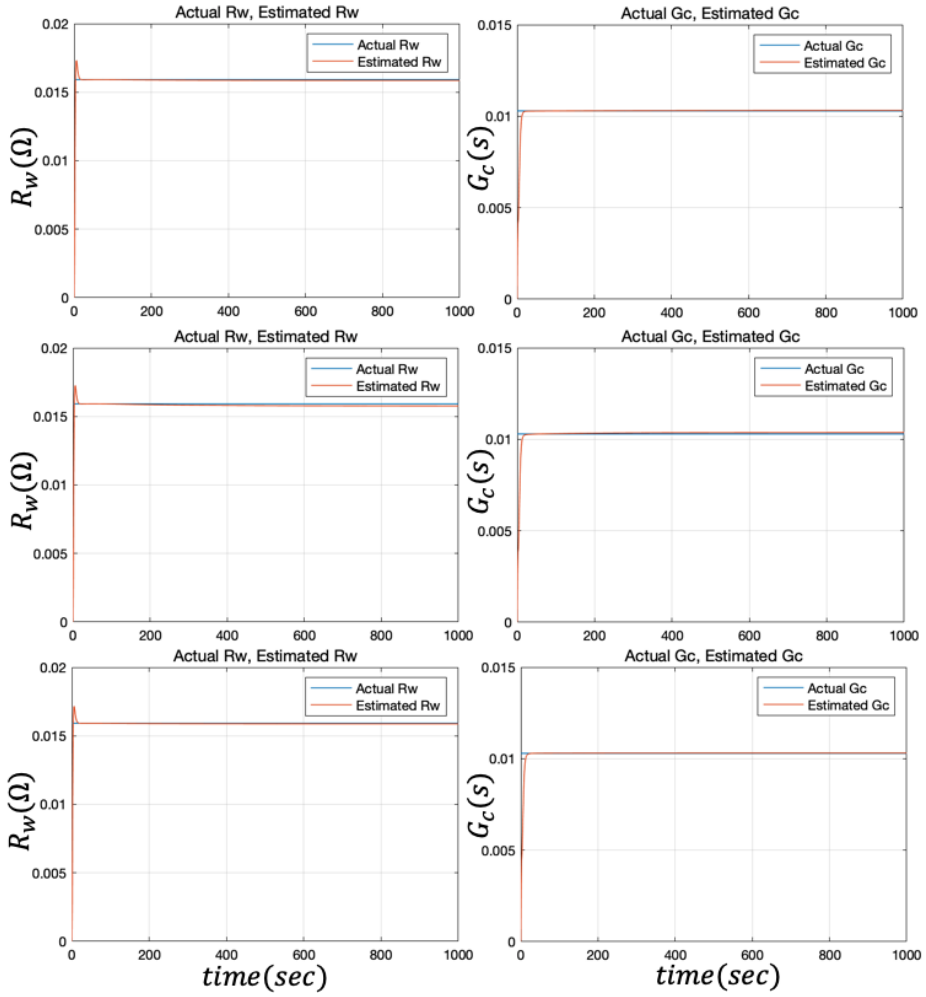

Figure 4.8: Convergence of Parameters with 1% decrease in Thermal Parameters in $k_{winding}$ (1^{st} Row), k_{iron} (2^{nd} Row) and k_{liner} (3^{rd} Row)

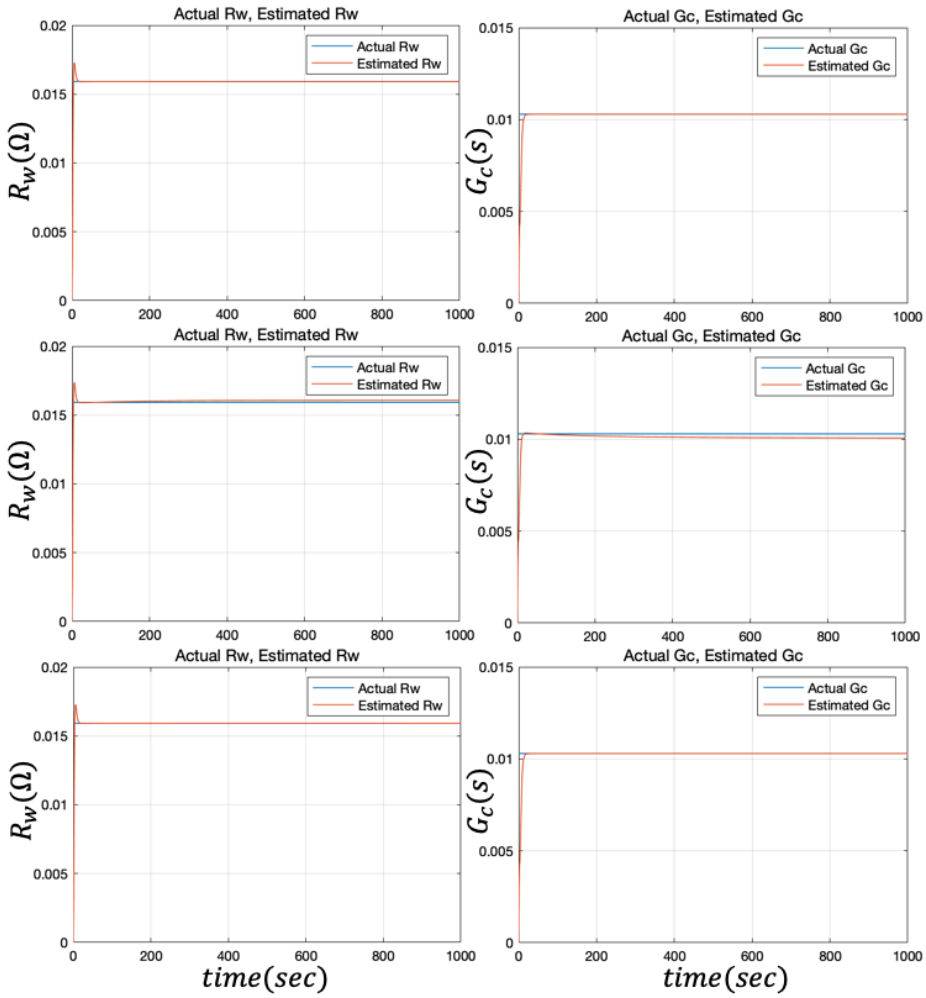

Figure 4.9: Convergence of Parameters with 1% decrease in H_{end} (1^{st} Row), H_{liq} (2^{nd} Row) and H_{ags} (3^{rd} Row)

To see how the estimator works with even larger uncertainty, simulations are also conducted with 10% uncertainty in the conductivity and convection coefficient, as shown in Figs. 4.11 and 4.10.

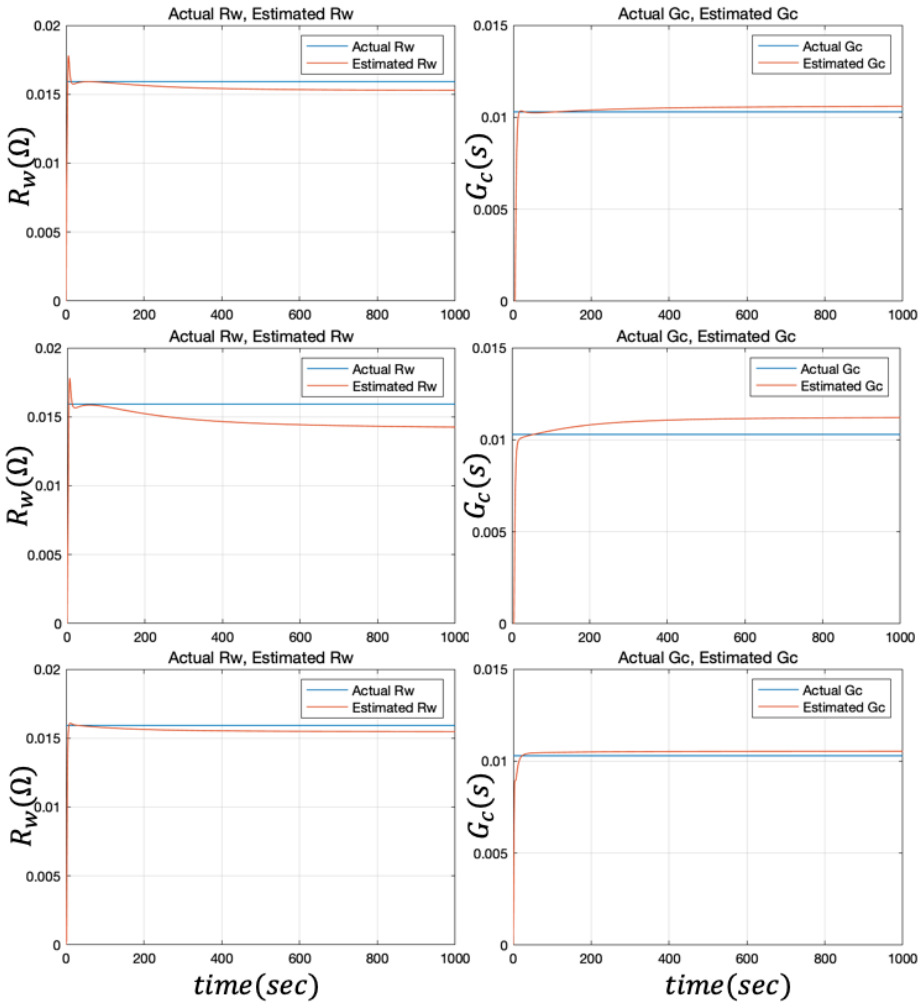

Figure 4.10: Convergence of Parameters with 10% decrease in Thermal Parameters in $k_{winding}$ (1^{st} Row), k_{iron} (2^{nd} Row) and k_{liner} (3^{rd} Row)

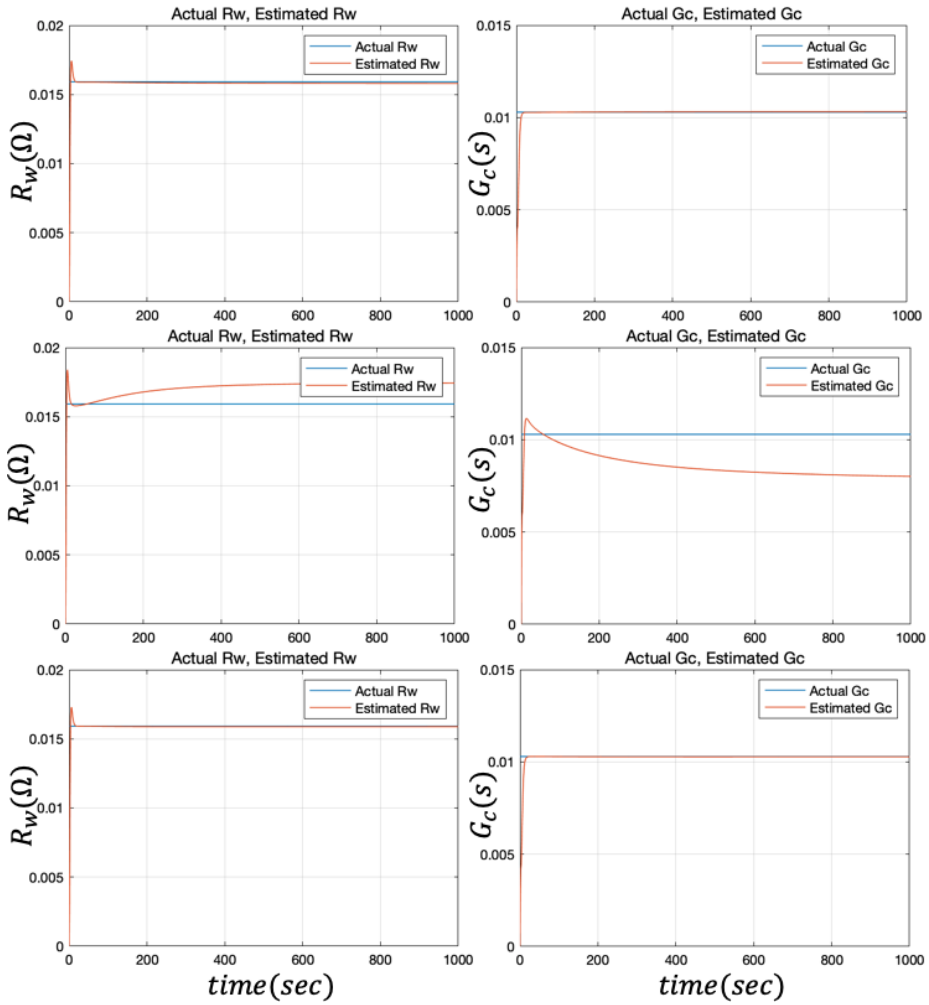

Figure 4.11: Convergence of Parameters with 10% decrease in Thermal Parameters in H_{end} (1^{st} Row), H_{liq} (2^{nd} Row) and H_{ags} (3^{rd} Row)

It can be seen that larger errors occur for both R_w and G_c due to large uncertainty (10%) in k_i in Fig. 4.10, and $h_{b,j}$ in Fig. 4.11. The errors, however, are still less than the estimation errors of the electrical model with 1% uncertainty in L_q for R_w and G_c, and λ_{PM} for R_w. It is worth noting that the estimated parameters are more sensitive to H_{liq}, because the cooling jacket removes most of the heat, thus considerable $\frac{H_{b,j}}{P_{loss,i}}$.

The numerical sensitivity for the estimator based on the thermal model is compared with theoretical expressions for both uncertainties of 1% and 10%, shown in Table 4.5.

Table 4.5: Estimated Parameter Sensitivity (Thermal Model)

Uncertainty Estimation	Sensitivity	
	Analysis	Simulation
$99\%k_{winding}, R_w$	0.43	0.39
$99\%k_{winding}, G_c$	0.34	0.31
$99\%k_{iron}, R_w$	1.20	1.04
$99\%k_{iron}, G_c$	0.95	0.85
$99\%k_{liner}, R_w$	0.29	0.27
$99\%k_{liner}, G_c$	0.23	0.22
$99\%H_{end}, R_w$	0.09	0.08
$99\%H_{end}, G_c$	0.03	0.03
$99\%H_{liq}, R_w$	0.97	0.96
$99\%H_{liq}, G_c$	2.48	2.40
$99\%H_{ags}, R_w$	0	0
$99\%H_{ags}, G_c$	0	0
$90\%k_{winding}, R_w$	0.43	0.42
$90\%k_{winding}, G_c$	0.34	0.32
$90\%k_{iron}, R_w$	1.20	1.13
$90\%k_{iron}, G_c$	0.95	0.92
$90\%k_{liner}, R_w$	0.29	0.29
$90\%k_{liner}, G_c$	0.23	0.24
$90\%H_{end}, R_w$	0.09	0.08
$90\%H_{end}, G_c$	0.03	0.03
$90\%H_{liq}, R_w$	0.97	0.96
$90\%H_{liq}, G_c$	2.48	2.40
$90\%H_{ags}, R_w$	0	0.02
$90\%H_{ags}, G_c$	0	0.01

Overall, the simulation results agree well with the theoretical analysis.

4.5.4 Discussion

To understand the simulation results, the component contribution in Eq.(4.13) and Eq.(4.19) is investigated for the operating conditions shown in Table.4.3. Specifically, for the electrical model, the voltage drop due to R_w, G_c and $\Delta\vec{z}_{e,s}$ (EMF) in Eq.(4.13) are compared. For the thermal model, the temperature rise due to R_w, G_c and $\Delta\vec{z}_{t,s}$ (convective boundary) in Eq.(4.19) are compared.

Fig. 4.12 shows the how large each component is in Eq.(4.13) for the electrical

model and Eq.(4.19) for the thermal model for the operating conditions in Table. 4.3. For the electrical model, the voltage drops due to EMF are much larger than those due to the estimated parameters of R_w and G_c. In contrast, for the thermal model, the temperature changes due to convection are much smaller than or with the same order as those due to R_w and G_c. Consequently, small errors in the electrical model's uncertain parameters will cause large errors in the estimated parameters, but uncertainty will not greatly influence the parameter convergence if using the thermal model. We can extend this analysis to the dynamic sensitivity. Dynamic voltages will add another component for back EMF ($L\frac{di^r}{dt}$), while the transient temperature change due to convection and R_w, G_c is still in proportion as the steady state, but with some amount of power to firstly increase the system thermal capacitance. Thus the estimator based on thermal model should have more robust dynamic performance.

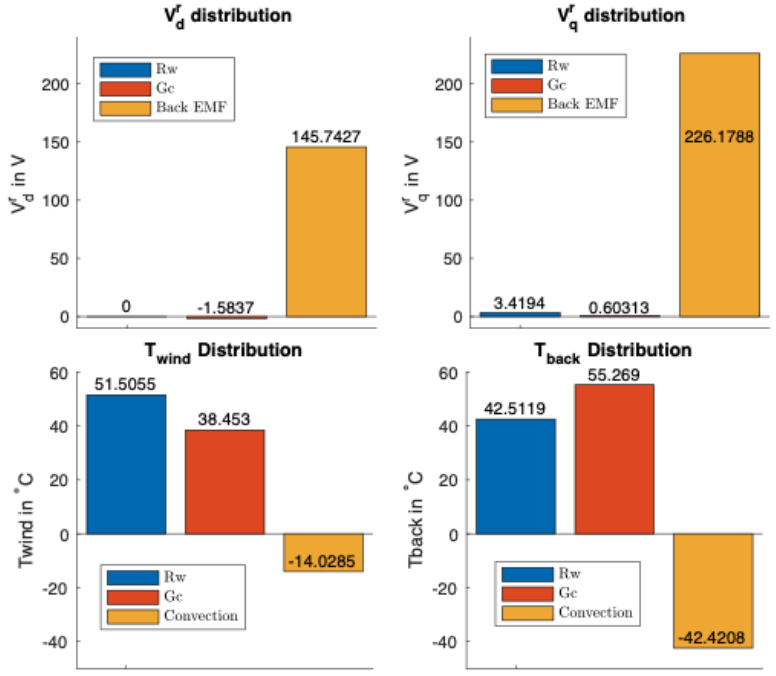

Figure 4.12: Each Component in the Output Signals. Top: Electrical Model. Bottom: Thermal Model

The operating conditions will largely influence the estimator sensitivity. Thus,

sensitivity variation over the entire operating conditions (varying i_q^r and RPM with $i_d^r = 0A$) for the electrical and thermal models are shown in Figs 4.13, 4.14 and 4.15. For clear demonstration, the sensitivities are saturated at 20.

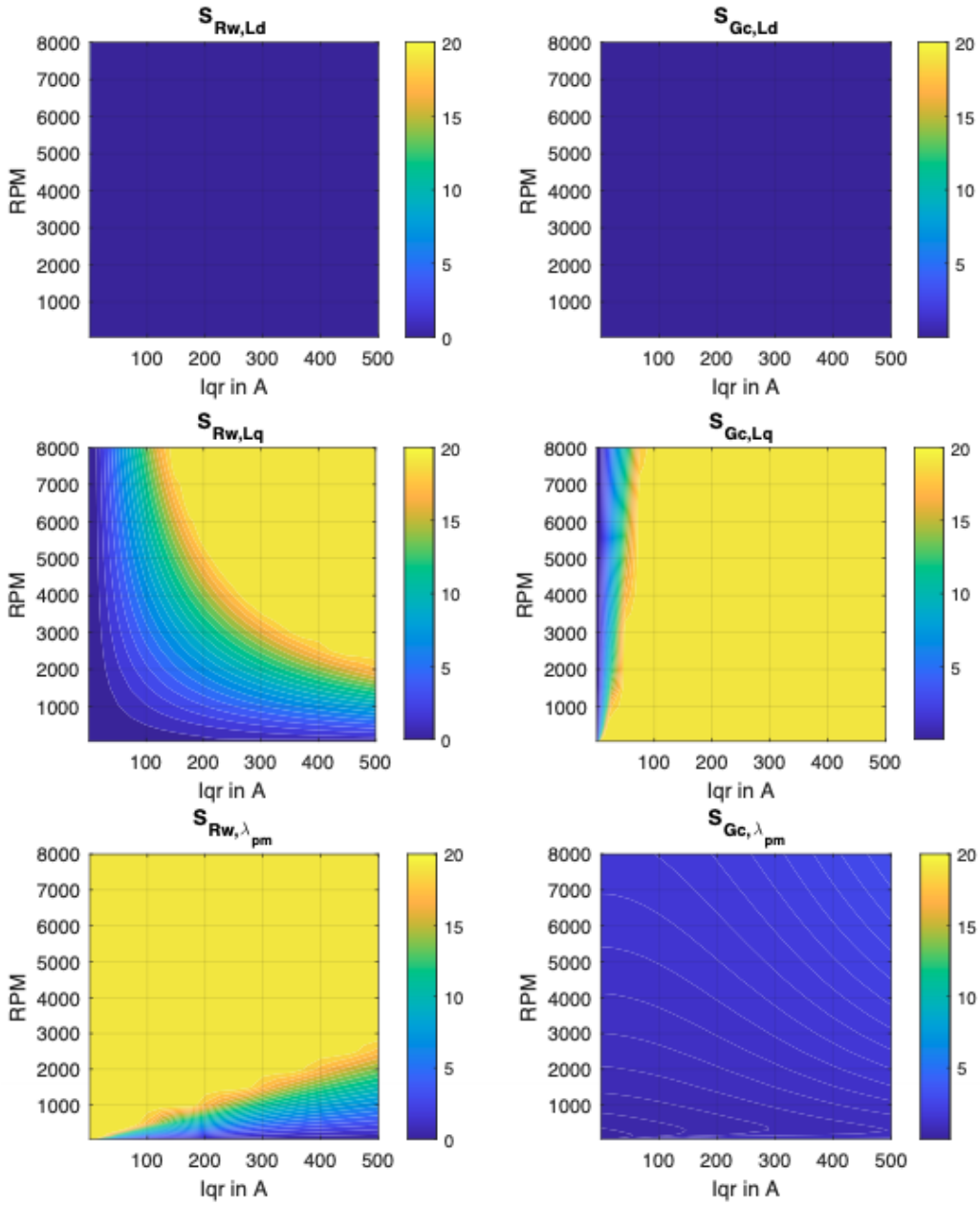

Figure 4.13: Sensitivities based on Electrical Model for Operating Conditions Saturated at 20. Top: L_d. Middle: L_q. Bottom: λ_{PM}

Note that when $i_q^r = 0A$, R_w can not be estimated, thus a singularity occurs in

the sensitivity. This can not be easily seen due to the small singularity region. Also, S_{G_c,L_d} and $S_{G_c,\lambda_{PM}}$ are non zero, due to the consideration of $R_w G_c$ terms which are ignored in the sensitivity analysis.

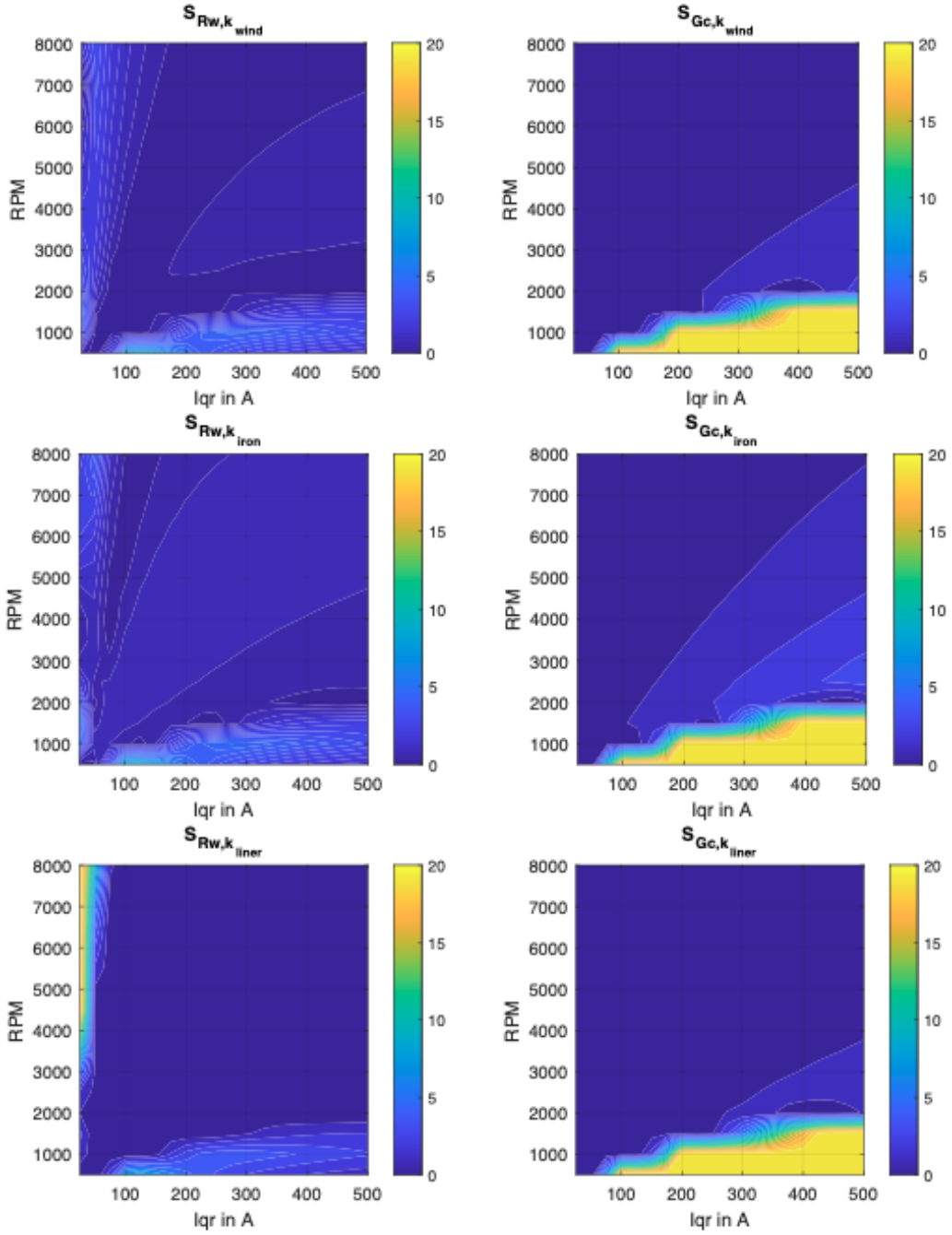

Figure 4.14: Sensitivities based on Thermal Model with Thermal Conductivity Uncertainty for Operating Conditions Saturated at 20. Top: $k_{winding}$. Middle: k_{iron}. Bottom: k_{liner}

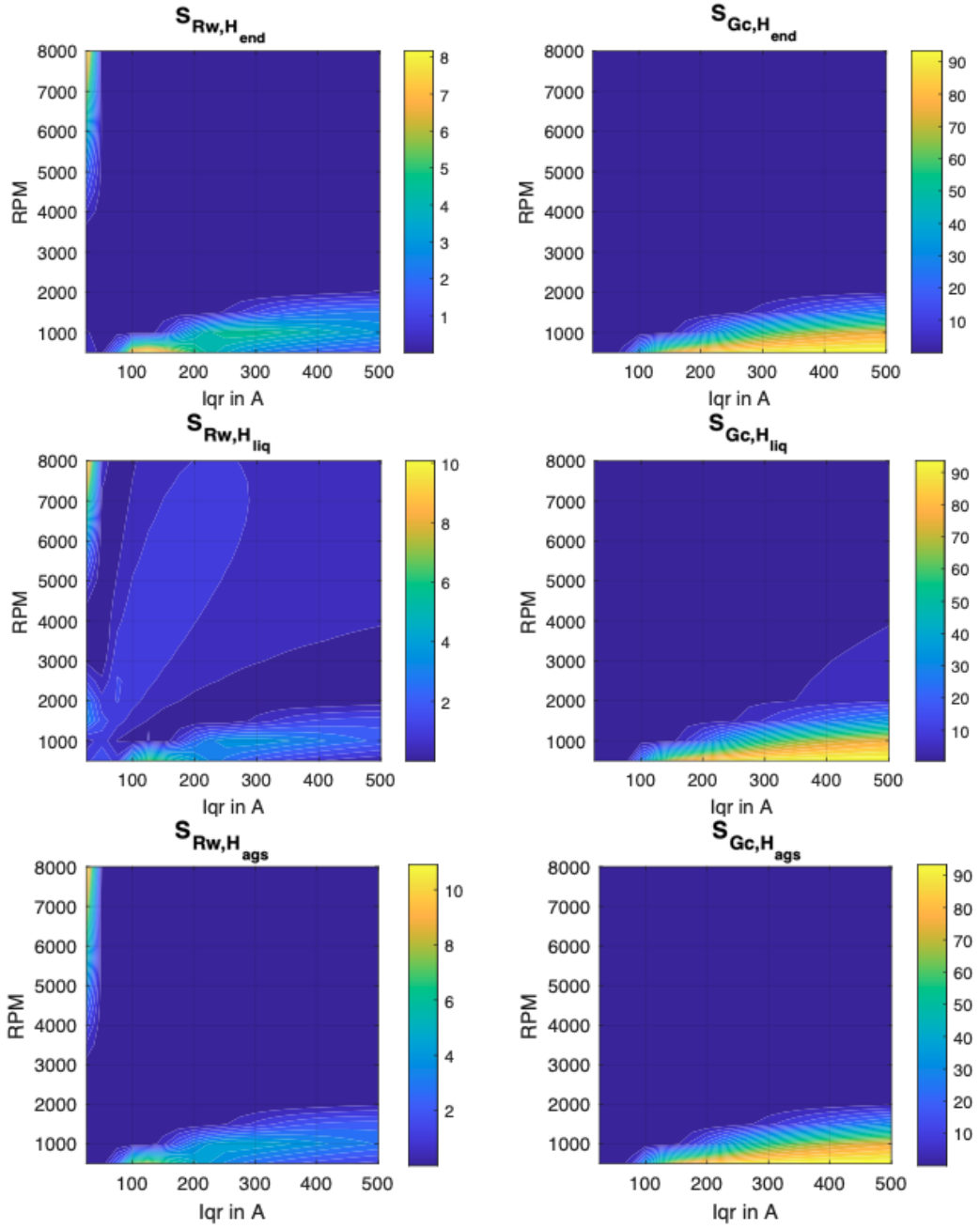

Figure 4.15: Sensitivities based on Thermal Model with Convective Coefficient Uncertainty for Operating Conditions Saturated at 20. Top: H_{end}. Middle: H_{liq}. Bottom: H_{ags}

It can be seen that the thermal model's sensitivity is small over wide operating conditions except for low current or low-speed regions. Note that S_{G_c} becomes significant for low speed region since core loss becomes small. As a result, since core loss is

negligible at low speed, large sensitivity in this region is acceptable. For the estimator based on the electrical model, sensitivities are relatively large for uncertainties in L_q and λ_{PM}. One thing to notice is that, $S_{R_w,L_d} = S_{G_c,L_d} = 0$ and $S_{G_c,\lambda_{pm}}$ is small, due to the command of $i_d^r = 0A$ to achieve minimum winding loss for SMPMs. Significant estimation errors can occur if non-zero i_d^r is applied to achieve field weakening referring to Eqs. (4.31), (4.32) and (4.33). The operating range of small sensitivity using the electrical model is limited to the low-current or low-speed region. This is not a region that electrical machines usually operate in due to the low efficiency in this region. For the normal operating range (considerable current and speed), the estimator based on the thermal model is more robust than the electrical model. Referring to Table.4.2, the thermal model is more robust over a wide operating range and suitable for online loss estimation.

4.6 Conclusion

A comparative study of the robustness of online loss estimators for PMSMs based on electrical and thermal models is conducted in this chapter. Robustness for the electrical model and the thermal model to uncertain parameters is theoretically determined using sensitivity analysis. Simulation results validate the analytical expressions. The operating conditions under which the thermal model can achieve better robustness are demonstrated. It is concluded that the estimator based on the thermal model is more robust than the electrical model in most operating conditions. This conclusion is useful for applications requiring accurate loss estimation.

CHAPTER V

Conclusion and Future Work

5.1 Conclusion

Computationally-efficient thermal and electromagnetic models of electric machines, with one potential application for the thermal model, are presented in this dissertation.

A computationally efficient steady-state thermal convection model is proposed in Chapter 2, which focuses on heat convection considering laminar flow for low rotor speeds and Taylor vortices for medium rotor speeds. It is shown that the fluid dynamic/heat transfer expressions satisfy a homogeneity property under reasonable assumptions when modeling airflow in electric machines. This property dramatically reduces the space of possible heat convection models and the number of simulations need to parameterize the model. The time-averaged heat flux model shows significantly better accuracy than second-(low speed) or third-(medium speed) order models when compared with CFD simulation results.

An AC resistance model for winding solid conductors is proposed in Chapter 3. An innovative and computationally efficient method is presented. The method uses a 1D magnetoquasistatic model of the stator slot region to develop boundary transfer relations between the individual turns of the winding. These relations are used to create an impedance matrix associated with the winding turns, easily calculating

the AC resistance for different configurations. FEA-based simulation data of current distribution and experiment measurements are used to validate the proposed method.

An application of the thermal model for electric machines is presented in Chapter 4: online loss estimation of AC synchronous permanent magnet machines. A comparative study between the online loss estimators based on electrical/thermal models is conducted by analyzing estimator robustness via a sensitivity analysis. A comprehensive performance evaluation is performed when other parameters in the parametric model are uncertain. Results show that the online loss estimator based on the thermal model is more robust than that based on the electrical model. The sensitivity as a function of operating conditions for each model are provided.

5.2 Future Work

In this section, possible future work is discussed. The future work consists of three main categories: computationally efficient thermal model, computational efficient loss calculation, and analysis of possible applications of the thermal model.

5.2.1 Computational Efficient Thermal Model

Heat Convection Model for high rotor speed needs to be determined, where turbulence is expected to occur. Although turbulence is itself unstable and theoretically requires transient simulation, heat transfer is actually a macro phenomenon. Most common simplifications include making use of steadiness of flow and heat transfer with rotation: transient flow solutions are in most cases unnecessary, as time-averaging models give close results at a fraction of time [16]. As a result, only time averaging governing equations: Reynolds-Averaged Navier-Stokes Equations (RANS) are needed. The RANS for incompressible flow are shown in Eq.(5.1a) and Eq.(5.1b).

$$\frac{\partial \overline{v}_i}{\partial t} = 0 \qquad \text{(Conservation of Mass)} \tag{5.1a}$$

$$\frac{\partial \overline{v}_i}{\partial t} + \overline{v}_j \frac{\partial \overline{v}_i}{\partial x_j} + \frac{1}{\rho}\frac{\partial \overline{p}}{\partial x_i} - \nu \frac{\partial^2 \overline{v}_i}{\partial x_i \partial x_j} + \frac{\partial \overline{v_i' v_j'}}{\partial x_j} = 0 \qquad \text{(Conservation of Momentum)} \tag{5.1b}$$

The Reynolds Stress Tensor $\overline{v_i' v_j'}$ needs to be modeled. And for most turbulent models, the eddy viscosity hypothesis is applied, as shown in Eq.(5.2).

$$-\overline{v_i' v_j'} = 2\nu_T S_{ij} - \frac{2}{3} k_T \delta_{ij}, \tag{5.2}$$

where

$$k_T = \frac{1}{2}\overline{v_i' v_i'} \qquad \text{(Turbulent Kinetic Energy)} \tag{5.3a}$$

$$S_{ij} = \frac{1}{2}\left(\frac{\partial v_i}{\partial x_j} + \frac{\partial v_j}{\partial x_i}\right) \qquad \text{(Mean Strain-Rate Tensor)} \tag{5.3b}$$

And ν_T is the kinetic eddy viscosity, and δ_{ij} is the Kronecker delta.

If $k - \epsilon$ model for turbulence is applied, ν_T can be expressed as:

$$\nu_T = \rho C_\mu \frac{k_T^2}{\epsilon}, \tag{5.4}$$

where $C_\mu = 0.09$ and ϵ is the turbulent dissipation. And two more equations are added to the governing equations:

$$\frac{\partial k_T}{\partial t} + \overline{v}_j \frac{\partial k_T}{\partial x_j} = \tau_{ij}\frac{\partial \overline{v}_i}{\partial x_j} - \epsilon + \frac{\partial}{\partial x_j}\left[(\nu + \nu_T/\sigma_k)\frac{\partial k_T}{\partial x_j}\right], \tag{5.5a}$$

$$\frac{\partial \epsilon}{\partial t} + \overline{v}_j \frac{\partial \epsilon}{\partial x_j} = C_{\epsilon 1}\frac{\epsilon}{k_T}\tau_{ij}\frac{\partial \overline{v}_i}{\partial x_j} - C_{\epsilon 2}\frac{\epsilon^2}{k_T} + \frac{\partial}{\partial x_j}\left[(\nu + \nu_T/\sigma_\epsilon)\frac{\partial \epsilon}{\partial x_j}\right], \tag{5.5b}$$

where $C_{\epsilon 1} = 1.44$, $C_{\epsilon 2} = 1.92$, $\sigma_k = 1$ and $\sigma_\epsilon = 1.3$.

Many turbulent models can be used. The models are classified based on how to model the Reynolds Stress Tensor $\overline{v_i' v_j'}$ to close RANS. Besides $k-\epsilon$ model, turbulent models include the Spalart–Allmaras Model (SA), $k-\omega$ model, Menter's Shear Stress Transport Model (SST), and Reynolds Stress Equation Model (RSM). All listed models describe how the eddy viscosity ν_T is modeled, except for the RSM which avoids the eddy viscosity hypothesis but directly computes each component of the Reynolds stress tensor. These models are compared in [101]. In most turbulent models, the eddy viscosity hypothesis is applied, which contradicts our constant viscosity assumption. When substituting the scaled profiles into RANS, this viscosity is also scaled accordingly. It can be shown that for compressible flow, the governing equations can also be satisfied with the scaled profiles. However, for turbulence, wall functions are applied to reduce cell numbers and calculate temperature gradient and heat fluxes in the turbulent boundary layer. Thus the homogeneity property used to model heat convection for low and medium rotor speed for electric machines may not be applicable.

To model turbulence, 3D steady-state CFD simulations are needed. The homogeneity property will then be tested. If the property still holds, the proposed model should be able to capture the heat convection for higher rotor speed, similarly to the modeling process used for low and medium rotor speeds.

If the property does not hold anymore, an alternative approach will need to be proposed. Possible approaches include:

1. Take the full-order CFD simulation profiles and apply non-linear order reduction techniques with a compressible density air model;

2. Choose air density piece-wise constant as a function of temperature;

3. Use a constant air density model and apply linear model order reduction techniques.

5.2.2 Computationally Efficient Loss Model

A computationally-efficient AC resistance model is presented in this dissertation to model the winding conduction loss accurately. However, core loss is also considerable, especially for high rotor speed. The approaches to model iron loss involves empirical models such as SE, MSE, GSE, iGSE and NSE. One thing to notice is that all these models suffer from frequency-dependent Steinmetz coefficients. Due to hysteresis loss, flux density history will also impact iron loss, which is not considered for this category [42]. Moreover, PWM waveforms generated by inverters can also influence machine loss, as analyzed in [102] and a rotor eddy current loss model considering PWM effect is provided in [103].

Many parameters are temperature dependent. If the loss can be determined efficiently and accurately, the loss calculation can be coupled with the thermal model to provide a more accurate thermal model. Xue *et al.* [104] coupled the thermal and loss analyses by improving the temperature-dependent iron loss model.

5.2.3 Relevant Applications

Besides loss estimation, the computationally efficient models can be used to construct model-based control techniques, such as Model Predictive Control (MPC). For example, an active liquid cooling system to regulate slot winding temperature based on gradient descent algorithms was proposed in [105]. Electric machines under three different cooling systems (housing cooling jacket, direct slot cooling, and liquid-cooled rotor) are analyzed in [106]. The thermal management system can limit temperature to guarantee normal operation and improve the efficiency of cooling systems.

Another potential application is thermal aging analysis. As mentioned in Chapter I, thermal aging follows the Arrhenius equation. Thermal lifetime evaluation can be helpful in design process and is feasible with the temperature profile. With the computationally efficient thermal model, temperature information can be used

to estimate Arrhenius curve thus predicting thermal aging. For example, a thermal lifetime determination method for machine insulation based on Arrhenius curves has been proposed in [107]. Analysis showing that how thermal aging influence winding conductivity is provided in [108].

APPENDIX

APPENDIX A

AC Resistance Considering Spacing

The derivation of AC resistance considering the spacing between the conductors is shown as follows. The gap between each conductor is assumed to be the same, denoted as W_g. The subscript ws stands for "with spacing."

Due to the spacing between conductors, two boundary conditions are needed for each turn, denoted as $\tilde{A}_{i,ws}^{(k)}$ and $\tilde{A}_{o,ws}^{(k)}$. Then the matrix form considering the spacing effects can be expressed in Eq.(3.22), with different expressions for $\mathbf{D}_{ws}$, $\mathbf{U}_{ws}$, $\tilde{\vec{v}}_{k,ws}$ and $\tilde{\vec{b}}_{k,ws}$, which are updated as:

$$\mathbf{D}_{ws} = \begin{bmatrix} coth(\tilde{\gamma}w_t) & coth(\tilde{\gamma}w_t) - csch(\tilde{\gamma}w_t) & -csch(\tilde{\gamma}w_t) \\ csch(\tilde{\gamma}w_t) & csch(\tilde{\gamma}w_t) - coth(\tilde{\gamma}w_t) & -coth(\tilde{\gamma}w_t) \\ 0 & 0 & -1 \end{bmatrix}, \tag{A.1}$$

$$\mathbf{U}_{ws} = \begin{bmatrix} 0 & 0 & 0 \\ 0 & 0 & 0 \\ -1 & 0 & 0 \end{bmatrix}, \tag{A.2}$$

$$\tilde{\vec{v}}_{k,ws} = \begin{bmatrix} j\omega(\tilde{A}^{(k)}_{i,ws}) \\ \tilde{\nabla\Phi}^{(k)}_{z,ws} \\ j\omega(\tilde{A}^{(k)}_{o,ws}) \end{bmatrix}, \tag{A.3}$$

$$\tilde{\vec{b}}_{k,ws} = \begin{bmatrix} \sum_{j=1}^{k-1} \tilde{I}^{(j)} \\ \sum_{j=1}^{k} \tilde{I}^{(j)} \\ -W_g\tilde{\gamma}\sum_{j=1}^{k} \tilde{I}^{(j)} \end{bmatrix}. \tag{A.4}$$

Similar to the process of non-spacing analysis, the solution is the same as Eq.(3.27). Extracting the potential gradient of k^{th} segment from the solution, we have:

$$\vec{\nabla\Phi}^{(k)}_{z,ws} = \vec{\nabla\Phi}^{(k)}_{z} - \frac{j\omega\mu_0 W_g}{h_t}\left[\sum_{j=1}^{k}\tilde{I}^{(j)} + \sum_{j=1}^{k+1}\tilde{I}^{(j)} ... \sum_{j=1}^{N}\tilde{I}^{(j)}\right], \tag{A.5}$$

where $\vec{\nabla\Phi}^{(k)}_{z}$ is the potential gradient without spacing. It can be seen that the additional term is reactive and hence contributes to the leakage inductance, but not the resistance. Therefore the AC resistance expression is unaffected by the gap.

BIBLIOGRAPHY

BIBLIOGRAPHY

[1] J. P. Rodrigue, *The Geography of Transport Systems*. United States of America: Routledge, 5th ed., 2020.

[2] D. Lowell and A. Huntington, "Electric vehicle market status." `https://www.mjbradley.com/sites/default/files/ElectricVehicleMarketStatus05072019.pdf`, 2019.

[3] Z. Runsen and F. Shinichiro, "The role of transport electrification in global climate change mitigation scenarios," *Environmental Research Letters*, vol. 15, pp. 1–12, 2020.

[4] E. Kontou, M. Melaina, and A. Brooker, "Light-duty vehicle attribute projections." `https://www.nrel.gov/docs/fy18osti/70455.pdf`, 2018.

[5] V. Buyukdegirmenci, P. Krein, and D. Abc, "Machine Characterization for Short-Term or Instantaneous Torque Capabilities: An Approach Based on Transient Thermal Response," *Proc. 2013 IEEE Int. Electric Machines and Drives Conf. (IEMDC)*, pp. 801–808, May 2013.

[6] C. Kral, A. Haumer, and S. B. Lee, "A Practical Thermal Model for the Estimation of Permanent Magnet and Stator Winding Temperatures," *IEEE Transactions on Power Electronics*, vol. 29, pp. 455–464, Jan. 2014.

[7] M. Valenzuela, P. Reyes, and D. Abc, "Simple and Reliable Model for the Thermal Protection of Variable-Speed Self-Ventilated Induction Motor Drives," *IEEE Transactions on Industrial Applications*, vol. 46, pp. 770–778, Mar. 2010.

[8] M. Legranger, G. Friedrich, S. Vivier, and J. Mipo, "Combination of Finite-Element and Analytical Models in the Optimal Multidomain Design of Machines: Application to an Interior Permanent-Magnet Starter Generator," *IEEE Transactions on Industrial Applications*, vol. 46, pp. 232–239, Jan. 2010.

[9] X. Tao, K. Zhou, A. Ivanco, and J. Wagner, "A hybrid electric vehicle thermal management system - nonlinear controller design," in *SAE Technical Paper*, 2015.

[10] S. Li, D. Han, and B. Sarlioglu, "Analysis of temperature effects on performance of spoke-type interior permanent magnet machines," in *2017 IEEE Transportation Electrification Conference and Expo (ITEC)*, pp. 442–447, 2017.

[11] J. D. McFarland and T. M. Jahns, "Investigation of the rotor demagnetization characteristics of interior pm synchronous machines during fault conditions," *IEEE Transactions on Industry Applications*, vol. 50, no. 4, pp. 2768–2775, 2014.

[12] G. Champenois, D. Roye, and D. Zhu, "Electrical and Thermal Performance Predictions in Inverter-Fed Squirrel-Cage Inudction Motor Drives," *Electric Machines and Power Systems*, vol. 22, pp. 355–369, 1994.

[13] S. P. Carfagno and R. J. Gibson, "Review of equipment aging theory and technology. final report," 9 1980.

[14] UQM Technologies Inc., Longmont, Colorado, U.S, *UQM PowerPhase 145 datasheet*.

[15] K. Zhou, J. Pries, and H. Hofmann, "Computationally-Efficient 3D Finite-Element-Based Dynamic Thermal Models of Electric Machines," *IEEE Transactions on Transportation Electrification*, vol. 1, pp. 138–149, Aug. 2015.

[16] A. Boglietti, A. Cavagnino, S. Martin, M. Markus, and M. Carlos, "Evelution and Modern Approaches for Thermal Analysis of Electrical Machines," *IEEE Transactions on Industrial Electronics*, vol. 56, pp. 871–882, 2009.

[17] P. Mellor, D. Roberts, and T. D.R, "Lumped Paramter Thermal Model for Electrical Machines of TEFC Design," *IEE Proceedings B - Electric Power Applications*, vol. 138, pp. 205–218, 1991.

[18] G. Taylor, "Stability of a Viscous Liquid Contained between Two Rotating Cylinders," *Philosophical Transactions of the Royal Society of London, Series A, Containing Papers of a Mathematical or Physical Character*, vol. 223, pp. 289–343, 1923.

[19] G. Taylor, "Distribution of Velocity and Temperature between Concentric Cylinders," *Proc. Roy Soc*, vol. 159, pp. 546–579, 1935.

[20] M. Hosain and R. Fdhila, "Air-gap heat transfer in rotating electrical machines: A parametric study," in 9^{th} *International Conference on Applied Energy, ICAE2017*, vol. 142, pp. 4147–4171, 2017.

[21] M. Fenot, E. Dorignac, A. Giret, and G. Lalizel, "Convective Heat Transfer in the Entry Region of an Annular Channel with Slotted Rotating Inner Cylinder," *Applied Thermal Engineering*, vol. 54, pp. 345–358, 2013.

[22] S. Nategh, Z. Huang, A. Krings, O. Wallmark, and M. Leksell, "Thermal modeling of directly cooled electric machines using lumped parameter and limited cfd analysis," *IEEE Transactions on Energy Conversion*, vol. 28, no. 4, pp. 979–990, 2013.

[23] F. Ahmed, E. Ghosh, and N. C. Kar, "Transient thermal analysis of a copper rotor induction motor using a lumped parameter temperature network model," in *2016 IEEE Transportation Electrification Conference and Expo (ITEC)*, pp. 1–6, 2016.

[24] L. Veg and J. Laksar, "Thermal model of high-speed synchronous motor created in matlab for fast temperature check," in *2018 18th International Conference on Mechatronics - Mechatronika (ME)*, pp. 1–5, 2018.

[25] A. Boglietti, A. Cavagnino, D. A. Staton, M. Popescu, C. Cossar, and M. I. McGilp, "End space heat transfer coefficient determination for different induction motor enclosure types," *IEEE Transactions on Industry Applications*, vol. 45, no. 3, pp. 929–937, 2009.

[26] B. Zhang, R. Qu, J. Wang, W. Xu, X. Fan, and Y. Chen, "Thermal Model of Totally EnclosedWater-Cooled Permanent-Magnet Synchronous Machines for Electric Vehicle Application," *IEEE Transactions on Industrial Applications*, vol. 51, pp. 3020–3029, 2015.

[27] S. Pickering, D. Lampard, and S. M., "Modeling Ventilation and Cooling of the Rotors of Salient Pole Machines," *Proc. IEEE-IEMDC, Cambridge, MA*, vol. 1, pp. 806–808, 2001.

[28] S. Viazzo and S. Poncet, "Numerical Simulation of the Flow Stability in a High Aspect Ratio Taylor-Couette System Submitted to a Radial Temperature Gradient," *Computers and Fluids*, vol. 101, pp. 15–26, 2014.

[29] M. Hosain, R. Fdhila, and K. Ronnberg, "Taylor-couette flow and transient heat transfer inside the annulus air-gap of rotating electrical machines," *Applied Energy*, pp. 624–633, 2017.

[30] V. Lepiller, A. Goharzadeh, A. Prigent, and I. Mutabazi, "Weak Temperature Gradient Effect on the Stability of the Circular Couette Flow," *Eur Phys J B*, vol. 61, pp. 445–455, 2008.

[31] T. Hayase, J. Hunphrey, and R. Greif, "Numerical Calculation of Convective Heat Transfer between Rotating Coaxial Cylinders with Periodically Embedded Cavities," *AMSE*, vol. 144, pp. 589–597, Aug. 1992.

[32] N. Lancial, F. Torriano, F. Beaubert, and S. Harmand, "Taylor-couette-poiseuille flow and heat transfer in an annulus channel with a slotted rotor," *Applied Energy*, pp. 92–103, 2016.

[33] R. Kedia, M. Hunt, and T. Colonius, "Numerical simulations of heat transfer in tyalor-couette flow," *Journal of Heat Transfer*, vol. 120, pp. 65–71, 1998.

[34] C. Micallef, S. Pickering, K. Simmons, and K. Bradley, "Improved Cooling in the End Region of a Strip-Wound Totally Enclosed Fan-Cooled Induction Electric Mcahine," *IEEE Transactions on Industry Electronics*, vol. 10, pp. 3517–3524, 2008.

[35] D. Lampard, S. J. Pickering, and J. Mugglestone, "The use of computational fluid dynamics to model the air flow in the end region of a tefc induction motor," in *IEE Colloquium on Modeling the Performance of Electrical Machines (Digest No: 1997/166)*, pp. 2/1–2/5, 1997.

[36] "Air density, specific weight and thermal expansion coefficient at varying temperature and constant pressures." `https://www.engineeringtoolbox.com/air-density-specific-weight-d_600.html`.

[37] X. Hu, S. Lin, S. Asgari, S. Stanton, and W. Lian, "A State Space Thermal Model for HEV/EV Nonlinear and Timevaring Battery Thermal System," *Proceedings of the ASME 2011 International Mechanical Engineering Congress and Exposition IMECE 2011*, vol. 1, pp. 1–8, 2011.

[38] X. Hu, H. Lei, S. Lin, S. Asgari, and S. Stanton, "A Computationally Efficient Transient Thermal Model for Electric Machines Based on Singular Value Decomposition," *IEEE Transportation Electrification Conference and Expo, Asia-Pacific*, vol. 1, pp. 1–6, 2014.

[39] Y. Lang, A. Malacina, L. Biegler, S. Munteanu, J. Madsen, and S. Zitney, "Reduced Order Model Based on Principal Component Analysis for Process Simulation and Optimization," *Energy and Fuel*, vol. 23, pp. 1695–1706, 2009.

[40] P. Ding, X. Wu, Y. He, and W. Tao, "A Fast and Efficient Method for Predicting Fluid Flow and Heat Transfer Problem," *Journal of Heat Transfer*, vol. 130, pp. 032502/1– 032502/17, 2008.

[41] W. Choi, S. Li, and B. Sarlioglu, "Core loss estimation of high speed electric machines: An assessment," in *IECON 2013 - 39th Annual Conference of the IEEE Industrial Electronics Society*, pp. 2691–2696, 2013.

[42] A. Krings and J. Soulard, "Overview and comparison of iron loss models for electrical machines," in *2010 Ecological Vehicles Renewable Energies*, 2010.

[43] C. Mi, G. R. Slemon, and R. Bonert, "Modeling of iron losses of permanent-magnet synchronous motors," *IEEE Transactions on Industry Applications*, vol. 39, no. 3, pp. 734–742, 2003.

[44] S. Bobbio, G. Milano, C. Serpico, and C. Visone, "Models of magnetic hysteresis based on play and stop hysterons," *IEEE Transactions on Magnetics*, vol. 33, no. 6, pp. 4417–4426, 1997.

[45] S. Steentjes, S. Boehmer, and K. Hameyer, "Permanent magnet eddy-current losses in 2-d fem simulations of electrical machines," *IEEE Transactions on Magnetics*, vol. 51, no. 3, pp. 1–4, 2015.

[46] P. Ponomarev, J. Keränen, and P. Pasanen, "Electromagnetic transient finite element 3d modelling of electrical machines using open-source tools," in *2016 XXII International Conference on Electrical Machines (ICEM)*, pp. 1657–1661, 2016.

[47] J. Vkzncik, "Prediction of windage power loss in alternators," in *NASA Technical Note NASA TN D-4849*, 1968.

[48] S. Shah, B. Silwal, and A. Lehikoinen, "Efficiency of an Electrical Machine in Electric Vehicle Application," *Journal of the Institute of Engineering*, vol. 1, pp. 20–29, 2015.

[49] S. Rhyu, J. Lee, and J. Seo, "Design of the End-Coil Structure with Square Conductor for the Automobile ISG," *EVS28 International Electric Vehicle Symposium and Exhibition, KINTEX, Korea*, vol. 1, pp. 1–5, May 2015.

[50] A. Eilenberger, R. Hintringer, M. Primorac, and D. Scherrer, "High Efficient Electric Motors with Bar Windings for Serial Production," *39th International Vienna Motor Symposium, Miba AG, Mateo Primorac*, vol. 1, pp. 1–13, Apr. 2018.

[51] P. Dowell, "Effects of Eddy Currents in Transformer Winding," *Proceedings. IEE*, vol. 113, pp. 1387–1394, Aug. 1966.

[52] E. Bennett and S. Larson, "Effective Resistance to Alternating Currents of Multi-layer Windings," *Electrical Engineering*, vol. 59, pp. 1010–1016, Dec. 1940.

[53] M. P. Perry, "Multiple layer series connected winding design for minimum losses," *IEEE Transactions on Power Apparatus and Systems*, vol. PAS-98, no. 1, pp. 116–123, 1979.

[54] J. Ferreira, "Improved Analytical Modeling of Conductive Losses in Magnetic Components," *IEEE Transactions on Power Electronics*, vol. 9, pp. 127–131, 1994.

[55] M. Bartoli, N. Noferi, R. A, and M. Kazimierczuk, "Modeling Litz-Wire Winding Losses in High-Frequency Power Inductors," *PESC Record. 27th Annual IEEE Power Electronics Specialists Conference*, vol. 1, pp. 1690–1696, 1996.

[56] F. A. Holguín, R. Asensi, R. Prieto, and J. A. Cobos, "Simple analytical approach for the calculation of winding resistance in gapped magnetic components," in *2014 IEEE Applied Power Electronics Conference and Exposition - APEC 2014*, pp. 2609–2614, 2014.

[57] L. J. Wu, Z. Q. Zhu, D. Staton, M. Popescu, and D. Hawkins, "Analytical model of eddy current loss in windings of permanent-magnet machines accounting for load," *IEEE Transactions on Magnetics*, vol. 48, no. 7, pp. 2138–2151, 2012.

[58] A. Bellara, Y. Amara, G. Barakat, and B. Dakyo, "Two-dimensional exact analytical solution of armature reaction field in slotted surface mounted pm radial flux synchronous machines," *IEEE Transactions on Magnetics*, vol. 45, no. 10, pp. 4534–4538, 2009.

[59] S. A. Swann and J. W. Salmon, "Effective resistance and reactance of a solid cylindrical conductor placed in a semi-closed slot," *Proceedings of the IEE - Part C: Monographs*, vol. 109, no. 16, pp. 611–615, 1962.

[60] S. A. Swann and J. W. Salmon, "Effective resistance and reactance of a rectangular conductor placed in a semi-closed slot," *Proceedings of the Institution of Electrical Engineers*, vol. 110, no. 9, pp. 1656–1662, 1963.

[61] S. A. Swann and A. R. M. Noton, "Effective resistance and reactance of a conductor of trapezoidal cross-section placed in semiclosed slot," *Proceedings of the Institution of Electrical Engineers*, vol. 117, no. 2, pp. 401–408, 1970.

[62] S. Xu and H. Ren, "Analytical computation for ac resistance and reactance of electric machine windings in ferromagnetic slots," *IEEE Transactions on Energy Conversion*, vol. 33, no. 4, pp. 1855–1864, 2018.

[63] J. Ferreira, "Analytical Computation of AC Resistance of Round and Rectangular Litz Wire Windings," *IEE Proceedings-B*, vol. 139, pp. 21–25, 1992.

[64] A. S. Thomas, Z. Q. Zhu, and G. W. Jewell, "Proximity loss study in high speed flux-switching permanent magnet machine," *IEEE Transactions on Magnetics*, vol. 45, no. 10, pp. 4748–4751, 2009.

[65] H. Hämäläinen, J. Pyrhönen, J. Nerg, and J. Talvitie, "Ac resistance factor of litz-wire windings used in low-voltage high-power generators," *IEEE Transactions on Industrial Electronics*, vol. 61, no. 2, pp. 693–700, 2014.

[66] C. R. Sullivan, "Optimal choice for number of strands in a litz-wire transformer winding," *IEEE Transactions on Power Electronics*, vol. 14, no. 2, pp. 283–291, 1999.

[67] X. Nan and C. Sullivan, "An Improved Calculation of Proximity-Effect Loss in High-Frequency Windings of Round Conductors," *IEEE 34th Annual Conference on Power Electronics Specialist, 2003. PESC '03*, vol. 1, pp. 853–860, 2003.

[68] H. Hämäläinen, J. Pyrhönen, and J. Nerg, "AC Resistance Factor in One-Layer Form-Wound Winding Used in Rotating Electrical Machines," *IEEE Transactions on Magnetics*, vol. 49, pp. 2967–2973, 2013.

[69] D. A. Gonzalez and D. M. Saban, "Study of the copper losses in a high-speed permanent-magnet machine with form-wound windings," *IEEE Transactions on Industrial Electronics*, vol. 61, no. 6, pp. 3038–3045, 2014.

[70] S. Ayat, R. Wrobel, J. Baker, and D. Drury, "A comparative study between aluminium and copper windings for a modular-wound ipm electric machine," in *2017 IEEE International Electric Machines and Drives Conference (IEMDC)*, pp. 1–8, 2017.

[71] M. Paradkar and J. Böcker, "Analysis of eddy current losses in the stator windings of ipm machines in electric and hybrid electric vehicle applications," in *8th IET International Conference on Power Electronics, Machines and Drives (PEMD 2016)*, pp. 1–5, 2016.

[72] V. Venegas, J. L. Guardado, E. Melgoza, and M. Hernandez, "A finite element approach for the calculation of electrical machine parameters at high frequencies," in *2007 IEEE Power Engineering Society General Meeting*, pp. 1–5, 2007.

[73] M. S. Rafaq and J. Jung, "A comprehensive review of state-of-the-art parameter estimation techniques for permanent magnet synchronous motors in wide speed range," *IEEE Transactions on Industrial Informatics*, vol. 16, no. 7, pp. 4747–4758, 2020.

[74] D. M. Reed, J. Sun, and H. F. Hofmann, "Simultaneous identification and adaptive torque control of permanent magnet synchronous machines," *IEEE Transactions on Control Systems Technology*, vol. 25, no. 4, pp. 1372–1383, 2017.

[75] A. Balamurali, C. Lai, G. Feng, V. Loukanov, and N. C. Kar, "Online multi-parameter identification of permanent magnet synchronous motors in ev application considering iron losses," in *2016 XXII International Conference on Electrical Machines (ICEM)*, pp. 2306–2312, 2016.

[76] M. Cao and H. Migita, "A high efficiency control of ipmsm with online parameter estimation," in *2018 21st International Conference on Electrical Machines and Systems (ICEMS)*, pp. 1421–1424, 2018.

[77] D. Q. Dang, M. S. Rafaq, H. H. Choi, and J. Jung, "Online parameter estimation technique for adaptive control applications of interior pm synchronous motor drives," *IEEE Transactions on Industrial Electronics*, vol. 63, no. 3, pp. 1438–1449, 2016.

[78] S. Li, D. Han, and B. Sarlioglu, "Compensation control algorithm for ipm machines considering temperature effects based on online multi-parameter estimation," in *2017 IEEE Applied Power Electronics Conference and Exposition (APEC)*, pp. 1188–1195, 2017.

[79] H. Khreis, A. Deflorio, and B. Schmuelling, "A novel online pmsm parameter identification method for electric and hybrid electric vehicles based on cluster technique," in *2015 IEEE International Electric Machines Drives Conference (IEMDC)*, pp. 41–47, 2015.

[80] Y. Xu, K. Yang, A. Liu, X. Wang, and F. Jiang, "Online parameter identification based on mtpa operation for ipmsm," in *2019 22nd International Conference on Electrical Machines and Systems (ICEMS)*, pp. 1–4, 2019.

[81] D. Liang, J. Li, and R. Qu, "Super-twisting algorithm based sliding mode observer for wide-speed range pmsm sensorless control considering vsi nonlinearity," in *2017 IEEE International Electric Machines and Drives Conference (IEMDC)*, pp. 1–7, 2017.

[82] J. Hey, A. C. Malloy, R. Martinez-Botas, and M. Lampérth, "Online monitoring of electromagnetic losses in an electric motor indirectly through temperature measurement," *IEEE Transactions on Energy Conversion*, vol. 31, no. 4, pp. 1347–1355, 2016.

[83] E. Ghosh, F. Ahmed, A. Mollaeian, J. Tjong, and N. C. Kar, "Online parameter estimation and loss calculation using duplex neural — lumped parameter thermal network for faulty induction motor," in *2016 IEEE Conference on Electromagnetic Field Computation (CEFC)*, pp. 1–1, 2016.

[84] Y. Wang, H. Hofmann, D. Rizzo, and S. Shurin, "Computationally-efficient heat convection model for electric machines," in *SAE Technical Paper*, 2017.

[85] Y. Wang, J. Pries, K. Zhou, H. Hofmann, and D. Rizzo, "Computationally efficient ac resistance model for stator winding with rectangular conductors," *IEEE Transactions on Magnetics*, vol. 56, no. 4, pp. 1–9, 2020.

[86] C. Hsun and F. Weng, "Heat transfer for incompressible and compressible fluid flows over a heated cylinder," *Numerical Heat Transfer, Part A: Applications*, vol. 18, pp. 325–324, 1990.

[87] "Ansys fluent tutorial guide." `http://users.abo.fi/rzevenho/ansys\%20fluent\%2018\%20tutorial\%20guide.pdf`, 2017.

[88] M. Fenot, Y. Bertin, E. Dorignac, and G. Lalizel, "A Review of Heat Transfer between Concentric Rotating Cylinders with or without Axial Flow," *International Journal of Thermal Science*, vol. 50, pp. 1138–1155, July 2011.

[89] J. Melcher, *Continuum Electromechanics*. United States of America: MIT Press, Cambridge, Mass, 3rd ed., 1981.

[90] J. Pries, *Computationally Efficient Steady-State Simulation Algorithms for Finite-Element Models of Electric Machines*. PhD thesis, Univ. of Michigan, Dept. Elect. Eng. Comput. Sci., Ann Arbor, MI, U.S, 2015.

[91] "High voltage hairpin winding structure." https://d2t1xqejof9utc.cloudfront.net/pictures/files/83324/original.jpg?1463425744, 2019.

[92] I. Lar and M. M. Radulescu, "Equivalent core-loss resistance identification for interior permanent-magnet synchronous machines," in *2012 XXth International Conference on Electrical Machines*, pp. 1667–1671, 2012.

[93] G. Tao, *Adaptive Control Design and Analysis*. John Wiley & Sons, Inc., 2003.

[94] S. Moreau, R. Kahoul, and J. . Louis, "Parameters estimation of permanent magnet synchronous machine without adding extra-signal as input excitation," in *2004 IEEE International Symposium on Industrial Electronics*, vol. 1, pp. 371–376 vol. 1, 2004.

[95] G. Xie, K. Lu, S. K. Dwivedi, R. J. Riber, and W. Wu, "Permanent magnet flux online estimation based on zero-voltage vector injection method," *IEEE Transactions on Power Electronics*, vol. 30, no. 12, pp. 6506–6509, 2015.

[96] A. Williams, D. Burns, and M. McEwen, "Measurement of the specific heat capacity of the electron-beam grahite calorimeter," *NPL Report RSA(EXT)*, 1993.

[97] A. C. Whaley, "Experimental measurement of thermal conductivity of an unknown material," Master's thesis, Univ. of Tennessee, Dept. Mechanical. Eng., Knoxville, TN, U.S, 2008.

[98] D. Mueller and J. H. Abu-Mulaweh, "Estimation of the average heat transfer coefficient for a long horizontal cylindrical fin rod," in *Proceedings of the 2004 American Society for Engineering Education Annual Conference and Exposition*, 2004.

[99] E. Smith, F. Szidarovszky, W. Karnavas, and A. Bahill, "Sensitivity Analysis, a Powerful System Validation Technique," *The Open Cybernetics and Systemics Journal*, vol. 2, pp. 39–56, Feb. 2008.

[100] P. Ioannou and J. Sun, *Robust Adaptive Control*. Englewood Cliffs, NJ, USA: Prentice Hall, 1996.

[101] M. Kuosa, P. Sallinen, and J. Larjola, "Numerical and experimental modelling of gas flow and heat transfer in the air gap of an electric machine," *Journal of Thermal Science*, vol. 13, pp. 264–278, 2004.

[102] M. van der Geest, H. Polinder, and J. A. Ferreira, "Influence of pwm switching frequency on the losses in pm machines," in *2014 International Conference on Electrical Machines (ICEM)*, pp. 1243–1247, 2014.

[103] S. Jumayev, M. Merdzan, K. O. Boynov, J. J. H. Paulides, J. Pyrhönen, and E. A. Lomonova, "The effect of pwm on rotor eddy-current losses in high-speed permanent magnet machines," *IEEE Transactions on Magnetics*, vol. 51, no. 11, pp. 1–4, 2015.

[104] S. Xue, Z. Q. Zhu, Y. Wang, J. Feng, S. Guo, Y. Li, Z. Chen, and J. Peng, "Thermal-loss coupling analysis of an electrical machine using the improved temperature-dependent iron loss model," *IEEE Transactions on Magnetics*, vol. 54, no. 11, pp. 1–5, 2018.

[105] T. Dong, C. Zhu, F. Zhou, H. Zhang, F. Lu, and X. Zhang, "Innovated approach of predictive thermal management for high-speed propulsion electric machines in more electric aircraft," *IEEE Transactions on Transportation Electrification*, vol. 6, no. 4, pp. 1551–1561, 2020.

[106] G. Volpe, Y. C. Chong, D. A. Staton, and M. Popescu, "Thermal management of a racing e- machine," in *2018 XIII International Conference on Electrical Machines (ICEM)*, pp. 2689–2694, 2018.

[107] V. Madonna, P. Giangrande, G. Migliazza, G. Buticchi, and M. Galea, "A time-saving approach for the thermal lifetime evaluation of low-voltage electrical machines," *IEEE Transactions on Industrial Electronics*, vol. 67, no. 11, pp. 9195–9205, 2020.

[108] V. Madonna, P. Giangrande, and M. Galea, "Influence of thermal aging on the winding thermal conductivity in low voltage electrical machines," in *2020 23rd International Conference on Electrical Machines and Systems (ICEMS)*, pp. 123–128, 2020.